Measurement of The W Boson Production Cross Section and Search for W' in the Muon Channel from pp Collisions at $\sqrt{s} = 7$ TeV with the ATLAS Detector at the LHC

by

Xuefei Li

A dissertation submitted in partial fulfillment
of the requirements for the degree of
Doctor of Philosophy
(Physics)
in The University of Michigan
2012

Doctoral Committee:

Professor Bing Zhou, Chair
Professor Gordon L. Kane
Professor Gregory Tarle
Associate Professor Ji Zhu
Assistant Professor Jennifer Ogilvie

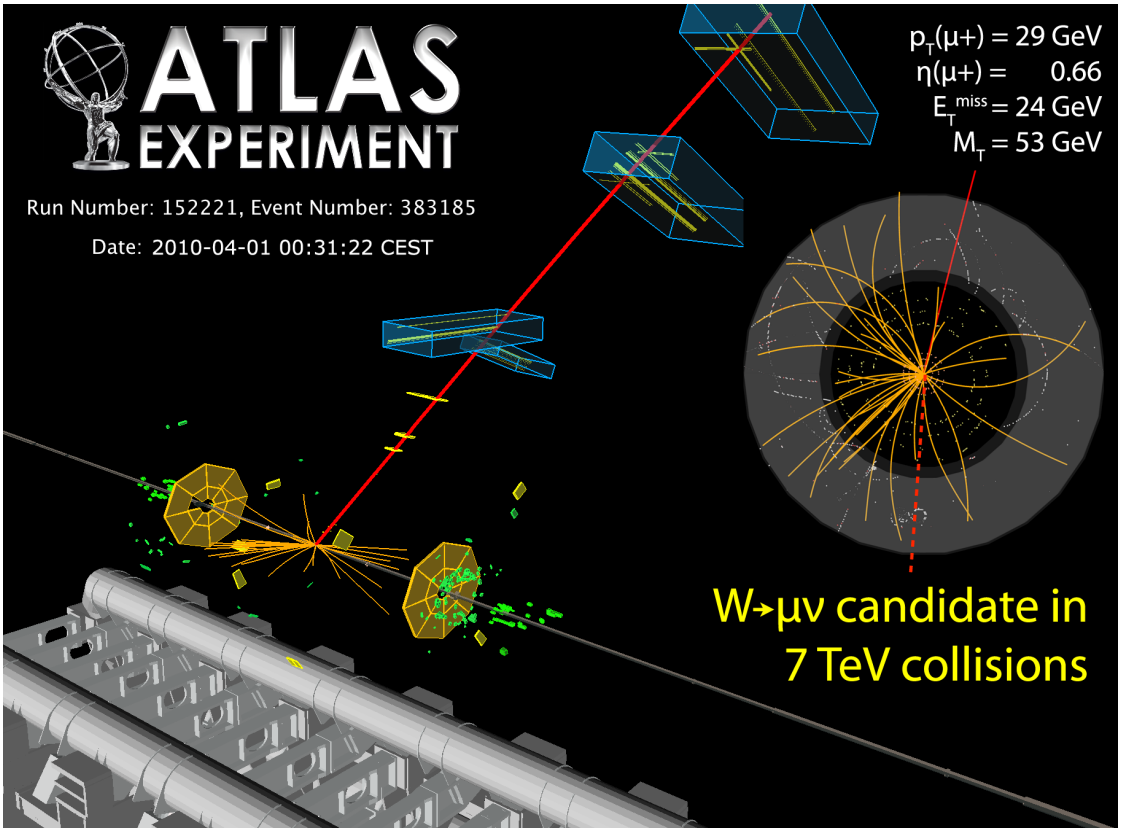

On April 1 2010, only one day after LHC started pp collision at $\sqrt{s} = 7$ TeV, the first candidate for $W \to \mu\nu$ decay collected by ATLAS experiment is shown in this ATLAS event display.

ACKNOWLEDGEMENTS

Along the long and winding path towards completion of this thesis, I received advice and assistance from many people for whom I will always be grateful. This thesis would not have been possible without the help of them.

First, I would like to thank Bing Zhou, my advisor. I want to thank her for taking me as a student, for her devotion and enthusiasm for high energy physics, and for her guidance through my PhD study. She also taught me lessons in life which will be beneficial for years to come.

I would like to thank everyone in the UM ATLAS group for their assistance, helpful suggestions and constructive criticism. In particular, I want to thank Haijun Yang for his tremendous help ever since I joined the group. He was always there to answer my questions. I also thank him for preparing and maintaining data samples for my analysis. I would like to thank Yusheng Wu for his timely assistance with many analysis related questions. I thank Junjie Zhu who had many discussions with me on the work presented in this thesis. I also thank other faculty members in the group: Homer Neal, Jianming Qian, and Rudi Thun for their valuable comments and suggestions on the ATLAS data analysis. Special thanks goes to Bob Ball, Shawn McKee and Ben Meekhof for their help on computing. They are always there to help even it's 10 pm at night or during weekends. I also want to thank Aaron Armbruster, Devin Harper, Hao Liu, Jianbei Liu, Lulu Liu, Alan Wilson and Jiaming Yu for their help and their great friendship. I thank Dan Levin and Josh Gevirtz for proof reading of the thesis. I feel lucky and proud to be part of this wonderful group.

I thank the members of my committee for their time and effort in helping me through this process.

I would like to acknowledge my husband Jun Wang. I would have not been able to complete this work if without his love, support and motivation. I am thankful every day that he is part of my life. I also thank our children, Jeremy and Vera. They are the best gifts I have ever received. They are constant reminders of what is truly important in life.

Lastly, but not the least, I want to thank my parents, especially my mom, and my grandma for their unconditional love and for everything they have done for me. I will not be able to reach where I am without their support.

CONTENTS

LIST OF FIGURES

Figure

LIST OF TABLES

Table

ABSTRACT

Measurement of The W Boson Production Cross Section and Search for W' in The Muon Channel from pp Collisions at $\sqrt{s} = 7$ TeV with the ATLAS Detector at the LHC

by

Xuefei Li

Chair: Bing Zhou

This thesis reports the first measurement of the weak gauge boson $W^{\pm}$ production cross section in proton-proton collisions at center-of-mass energy of 7 TeV at the Large Hadron Collider with the ATLAS experiment. Data used in this measurement were collected by the ATLAS detector from March 30 to October 31, 2010 with an integrated luminosity of 35.2 pb^{-1}. The cross section measurement was carried out using the muon decay channel from the process of $W \rightarrow \mu\nu$. The experimental signature is an isolated muon with large transverse momentum and a large momentum imbalance in the transverse plane w.r.t. the beam direction in the event. The large momentum imbalance is due to the neutrino escaping detection. The key elements of the measurement include studies of the muon trigger efficiency, the event selection optimization, the signal acceptance and associated systematic uncertainties, and the background estimation. With a total of 145226 candidates selected and a background estimation of $8461.6 \pm 6.9\ (stat) \pm 1509.3\ (sys) \pm 188.0\ (lumi)$, the total cross section times branching ratio $\sigma_W \times Br(W \rightarrow \mu\nu)$ is measured to be $10.15 \pm 0.025\ (stat) \pm 0.56\ (sys) \pm 0.35\ (lumi)$ nb, which is consistent with the

Next-to-Leading order Standard Model prediction of 10.46 ± 0.52 nb. The W^+/W^- charge ratio is measured to be $1.56 \pm 0.01\ (stat) \pm 0.09\ (sys)$, which is consistent with the theoretical prediction of $1.433^{+0.032}_{-0.020}$. Using the same datasets, a search for a new gauge boson W' is conducted with the same $\mu\nu$ final state. No experimental signature of W' in $\mu\nu$ decay channel is observed. A 95% confidence level of lower mass limit for W' is set at 1.32 TeV. This limit has exceeded the limit set by Tevatron experiments which have collected data with much higher integrated luminosity ($\sim 5.3\ fb^{-1}$) from $p\bar{p}$ collisions at center-of-mass energy of 1.96 TeV.

CHAPTER I

Introduction

Electroweak bosons were predicted by the unified gauge theory of electromagnetism and weak interactions by Glashow [38], Weinberg [47] and Salam [45] around 1968. In January 1983, the $W^{\pm}$ were discovered by the UA1 experiment [29] at the CERN Super Proton Synchrotron (SPS) proton-antiproton collider at a center-of-mass energy of $\sqrt{s} = 540\ GeV$, with the predicted properties. This discovery was shortly confirmed by the UA2 experiment [30] at CERN. Ever since its discovery the W boson has been investigated intensively in experiments. The W pair productions were studied in detail at LEP e^+e^- collider experiments [34, 21, 23, 24] in the Lep-II program. The CDF [20] [22] and DØ [18] experiments at the Fermilab Tevatron proton-antiproton collider have been accumulating W events over the last twenty years, allowing high-precision measurement of the W boson properties, including mass, width and couplings, as well as other detailed information on the production in proton-antiproton collisions. These measurements have put constraints on the mass range of the Standard Model (SM) Higgs boson, the cornerstone of electroweak symmetry breaking.

The W bosons are expected to be produced abundantly at the Large Hadron Collider (LHC) [35]. The study of W leptonic decays is one of the first milestones in the ATLAS [12] physics program for early LHC data. The unprecedented high

energy at the LHC will allow detailed measurements of W boson production properties and tests of the Standard Model in a previously unexplored kinematic domain. The production cross sections are known theoretically at the few percent level, and such precision makes W production measurement a stringent test of Quantum Chromodynamics (QCD). A measurement of the transverse momentum (denoted as p_T) distribution provides constraints on non-perturbative aspects of QCD related to the resummation of initial parton emissions, while the rapidity distribution is a direct probe of the parton density functions (PDFs) of the proton. Electroweak boson production with high transverse momentum final state leptons also enables important tests of the detector response, underlying processes and calibration of the detector. High p_T leptons play fundamental roles in a broad set of analyses including several new physics searches such as Higgs, extra gauge bosons and supersymmetric models. Finally, besides the cross section measurement of the W boson, the measurement of the asymmetry between the W^+ and W^- cross sections constitutes important tests of the Standard Model. The W^+/W^- ratio can be measured more precisely because some of the experimental and theoretical uncertainties cancel.

This thesis describes the W production cross section measurement in the muon decay channel with data from the proton-proton collisions at a center-of-mass energy ($\sqrt{s}$) of 7 TeV at the LHC. Data samples were collected by the ATLAS experiment during the period of March 30 to October 31, 2010 with a total integrated luminosity of 35.2 pb^{-1}. The experimental signature of W events in the muon decay channel includes prompt muon decays from W and cascade tau decays from the process of $W \to \tau\nu \to \mu + 3\nu$. The W^+ and W^- charge asymmetry is also measured in this analysis.

Many theoretical models beyond the Standard Model predict the existence of new gauge bosons, which have similar properties as the SM gauge bosons, but with much higher masses. A search for a hypothetical, charged new gauge boson particle, W',

in the $\mu\nu$ final state is conducted using the same data-set. A new mass limit is set on the W' gauge boson in this thesis.

This dissertation is organized as follows. Chapter II provides an overview of the theoretical foundations. Chapter III describes the experimental facility and instrument: the LHC and the ATLAS detector. Data and Monte Carlo samples used in this analysis are described in Chapter IV. The physics object reconstruction and identification in ATLAS detector is covered in Chapter V. Chapter VI presents the measurement of the $W \to \mu\nu$ cross section, including the event selection, detection acceptance determination, background estimation, and results. The search for W' and results are presented in Chapter VII. Finally, Chapter VIII summarizes the results of the $W \to \mu\nu$ cross section measurement and new limit on the W' mass.

CHAPTER II

Theoretical Foundations

2.1 The Standard Model

The Standard Model (SM) is a theoretical framework based on gauge theories, which are a special class of quantum field theories with an invariance principle requiring the existence of interactions among the particles. It is by far the most successful theory that has been tested experimentally to very high accuracy. SM is accepted as the current description of particle physics.

2.1.1 The Forces and Particles

The four known interactions in nature are gravity, electromagnetism, weak interaction and strong interaction. Electromagnetism and weak interaction has been unified into the electroweak theory by Glashow [38], Weinberg [47] and Salam [45] in the 1960's. The gauge field theory of the electromagnetism is called Quantum Electrodynamics (QED). Strong interaction is described by Quantum Chromodynamics (QCD). The Standard Model (SM) includes both the theory of electroweak and QCD. Gravity is neglected in this context because it is far too weak comparing to the scale of other forces. The SM is based on the symmetry group $SU(3)_C \otimes SU(2)_L \otimes U(1)_Y$, describing strong, weak and electromagnetic interactions.

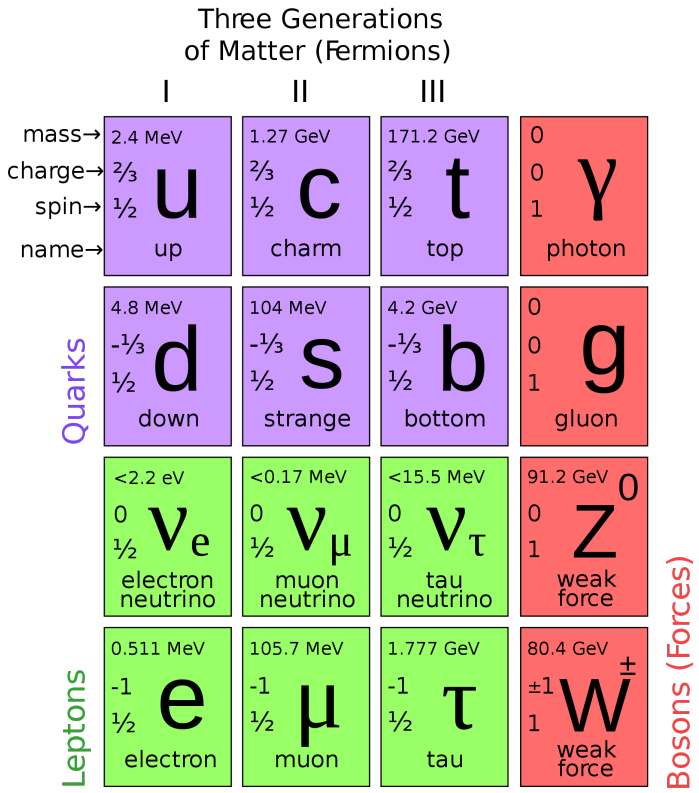

Figure 2.1: The family of Standard Model particles with their mass, spin and charge.

The basic particles in SM can be divided into two categories: matter particles and gauge bosons. The matter particles are leptons and quarks that are the constituents of matter. Gauge bosons are the force mediators in SM theory. The SM particle family is shown in Figure 2.1.

Leptons and quarks are both fermions with spin $\frac{1}{2}$. A quark carries the color charge of QCD, while a lepton does not. There are six lepton flavors and six quark flavors. They naturally fall into three families:

$$\begin{bmatrix} \nu_e & u \\ e^- & d \end{bmatrix}, \begin{bmatrix} \nu_\mu & c \\ \mu^- & s \end{bmatrix}, \begin{bmatrix} \nu_\tau & t \\ \tau^- & b \end{bmatrix},$$

in which the electron (e), muon (μ) and tau (τ) have electric charge -e, while each has its own neutrino of electric charge zero. Leptons participate in electromagnetic

interactions (charged leptons only) and weak interactions but not strong interactions. The neutrinos have non-zero, however tiny, masses and are viewed as massless in detector physics. A lepton number defined for each family is observed experimentally to be conserved. The quarks in the top row have electric charge of $\frac{2}{3}e$ and the ones in the bottom row have $-\frac{1}{3}e$. They participate in electromagnetic, weak and strong interactions. Each quark flavor comes in three colors. No free quarks have been observed as a quark is always bound inside a colorless hadron. There is another quantum number that the quarks carry, called the baryon number B, $B = \frac{1}{3}$ ($B = -\frac{1}{3}$ for antiparticles). Baryon number is also observed to be conserved in experiments.

In addition to leptons and quarks which are the basic particles of matter, there are the particles that transmit the forces: the gauge bosons. The interactions among elementary particles occur via the exchange of gauge bosons. Gauge bosons are spin-1 particles: eight massless gluons for strong interaction, three massive bosons, $W^{\pm}$ and Z^0 for weak interaction and one massless photon for electromagnetic interaction. Table 2.1 summaries the forces and the corresponding gauge bosons.

Force	Gauge Boson	Matter Particle
electromagnetism	photon γ	quarks and charged leptons
Weak interaction	$W^{\pm}$, Z^0	quarks and leptons
Strong interaction	eight gluons g	quarks

Table 2.1: Forces and corresponding mediators, as well as the mass particles that the forces act on.

Weak interactions involving $W^{\pm}$ are referred to as "charged current" interactions, while those involving Z^0 are referred to as "neutral current". Only charged current weak interactions can change the flavor of quarks. The Cabibbo-Kobayashi-Maskawa (CKM) matrix characterizes the strength with which these flavor changing charged current interactions occur. The CKM matrix elements are determined experimentally

as in Equation 2.2 [37].

$$\begin{pmatrix} d' \\ s' \\ b' \end{pmatrix} = V_{CKM} \begin{pmatrix} d \\ s \\ b \end{pmatrix} = \begin{pmatrix} V_{ud} & V_{cd} & V_{td} \\ V_{us} & V_{cs} & V_{ts} \\ V_{ub} & V_{cb} & V_{tb} \end{pmatrix} \begin{pmatrix} d \\ s \\ b \end{pmatrix}. \tag{2.1}$$

$$\begin{pmatrix} V_{ud} & V_{cd} & V_{td} \\ V_{us} & V_{cs} & V_{ts} \\ V_{ub} & V_{cb} & V_{tb} \end{pmatrix} = \begin{pmatrix} 0.9739 - 0.9751 & 0.221 - 0.227 & 0.0029 - 0.0045 \\ 0.221 - 0.227 & 0.9730 - 0.9744 & 0.039 - 0.044 \\ 0.0048 - 0.014 & 0.037 - 0.043 & 0.9990 - 0.9992 \end{pmatrix}. \tag{2.2}$$

2.1.2 The Standard Model Lagrangian

2.1.2.1 The $SU(2)_L \otimes U(1)_Y$ Term

In order to describe weak interactions, we need a structure for several fermionic flavors with left-handed and right-handed fields, considering that the left-handed fermions are in electroweak doublets, while the right-handed fermions are electroweak singlets. $SU(2)$ is the simplest group with doublet representations. The $U(1)$ group is needed for electromagnetic interactions. The subscript L means only left-handed fermions transform under $SU(2)$ and subscript Y is *hypercharge*, which represents the quantum number of the $U(1)$ group [40]. However, the electroweak $SU(2)$ symmetry is broken because there are no right-handed neutrinos observed in experiments.

At this point, fermions are assumed to be massless. The Lagrangian for free fermions is:

$$\mathcal{L}_{free} = i\psi_L^\dagger \gamma^\mu \partial_\mu \psi_L + i\psi_R^\dagger \gamma^\mu \partial_\mu \psi_R. \tag{2.3}$$

Here, ∂_μ is replaced by the covariant derivative $\mathcal{D}_\mu$ in order for the Lagrangian to

be invariant under local gauge transformation:

$$\mathcal{D}_\mu = \partial_\mu + i\frac{g_1}{2} Y B_\mu + i\frac{g_2}{2}\vec{\tau}\cdot\vec{W}_\mu \tag{2.4}$$

Where, g_1 and g_2 are two intrinsic coupling constants, corresponding to $SU(2)$ and $U(1)$ transformations, respectively. $\vec{W}$ are the associated gauge bosons for $SU(2)$, and B_μ is that for $U(1)$.

Then the electroweak Lagrangian becomes:

$$\mathcal{L}_{EW} = i\psi_L^\dagger \gamma^\mu \mathcal{D}_{L\mu}\psi_L + i\psi_R^\dagger \gamma^\mu \mathcal{D}_{R\mu}\psi_R - \frac{1}{4}\vec{W}^{\mu\nu}\cdot\vec{W}_{\mu\nu} - \frac{1}{4}B^{\mu\nu}B_{\mu\nu}. \tag{2.5}$$

Physical electroweak bosons can now be related to the charge eigenstates of these fields as in Equation 2.9. The $W^\pm$ and Z are massive while the photon A is massless, and orthogonal to Z.

$$W^{+\mu} = \frac{W_1^\mu + iW_2^\mu}{\sqrt{2}}, \tag{2.6}$$

$$W^{-\mu} = \frac{W_1^\mu - iW_2^\mu}{\sqrt{2}}, \tag{2.7}$$

$$Z^\mu = \cos\theta_W W_3^\mu - \sin\theta_W B^\mu, \tag{2.8}$$

$$A^\mu = \sin\theta_W W_3^\mu + \cos\theta_W B^\mu, \tag{2.9}$$

where, θ_W is called the Weinberg angle, or the mixing angle, $\theta_W = \tan^{-1}(g_1/g_2)$. It describes the mixing between the weak bosons W_3^μ and B_μ.

2.1.2.2 The Spontaneous Symmetry Breaking and Higgs Mechanism

So far, there are no mass terms in the Lagrangians presented. However, all the fermions and gauge bosons appear to be massive in experiments. Problem arises when adding in mass terms explicitly will destroy the local gauge invariance. One

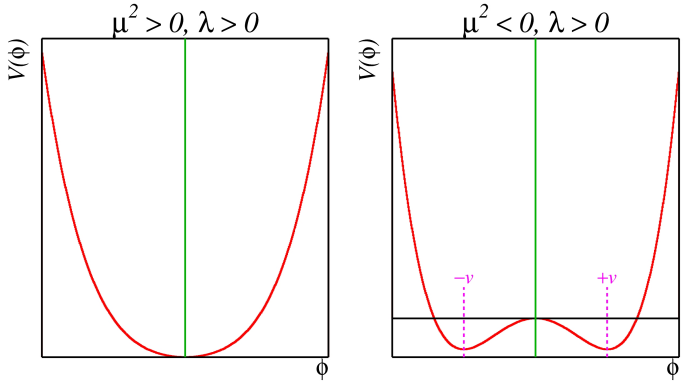

Figure 2.2: The potential $V(\phi)$ for $\mu^2 > 0$ (left) and $\mu^2 < 0$ (right) [1].

way to solve this problem is called the Higgs mechanism. This spontaneously breaks the electroweak $SU(2)_L$ symmetry. The Higgs field is a doublet in the $SU(2)$ space, which can be written as:

$$\phi(x) = \frac{1}{\sqrt{2}} \begin{pmatrix} \phi_1(x) + i\phi_2(x) \\ \phi_3(x) + i\phi_4(x) \end{pmatrix} \tag{2.10}$$

The Higgs Lagrangian is:

$$\mathcal{L}_{Higgs} = \mathcal{D}_\mu \phi^\dagger \mathcal{D}^\mu \phi - V(\phi), \tag{2.11}$$

where, the potential $V(\phi) = \mu^2 \phi^\dagger \phi + \lambda(\phi^\dagger \phi)^2$. If $\mu^2 > 0$, the potential has a trivial minimum at $\phi^\dagger \phi = 0$ and takes the shape of the left plot in Figure 2.2. When $\mu^2 < 0$, $V(\phi)$ has a minimum at $\phi^\dagger \phi = -\mu^2/2\lambda = v^2/2$, as the right plot in Figure 2.2 shows. This ground state is highly degenerate, thus the number of solutions is infinite. This gives rise to three massless Goldstone bosons, which later become the longitudinal $W^\pm$ and Z. The Higgs field can be expanded around the minimum as:

$$\phi(x) = \frac{1}{\sqrt{2}} \begin{pmatrix} 0 \\ v + H(x) \end{pmatrix} \tag{2.12}$$

Substituting Equation 2.12 into the Lagrangian in Equation 2.11, mass terms involving the $\vec{W}_\mu$ and B_μ fields appear. The mass of the W is given by $M_W = \sqrt{-2\mu^2}$, while the Z mass is $M_Z = M_W/\cos\theta_W$. The masses of fermions can also be obtained from the interaction terms between the Higgs boson and the fermions.

2.1.2.3 The $SU(3)_C$ Term

Strong interactions between the quarks and gluons are described by $SU(3)_C$ group. The subscript C stands for color, which identifies the three eigenstates of the symmetry group. The eight generators for $SU(3)$ correspond directly to the eight gluons of QCD theory. These gluons are massless because the $SU(3)$ symmetry remains unbroken in nature.

The quark fields ψ_q are $SU(3)$ triplets. The Lagrangian must be invariant under the transformation:

$$\psi_q \rightarrow e^{-ig_s T\cdot\theta(x)}\psi_q, \tag{2.13}$$

where T includes the eight 3×3 generators of $SU(3)$, which do not commute:

$$[T_a, T_b] = if_{abc}T_c, \tag{2.14}$$

f_{abc} denotes one element of a $3\times 3\times 3$ array of structure constants. The covariant derivative in this case is:

$$\mathcal{D}_\mu = \partial_\mu + ig_s T\cdot G_\mu, \tag{2.15}$$

where, G is an eight-component vector boson field. In the perturbative limit, these fields transform as follows:

$$G_{a\mu} \rightarrow G_{a\mu} + \partial_\mu\theta_a(x) + g_s f_{abc}\theta_b(x)G_{c\mu}. \tag{2.16}$$

With the substitution of the covariant derivative, the QCD Lagrangian can then be

written as:

$$\mathcal{L}_{QCD} = i\psi_q^\dagger \gamma^\mu \mathcal{D}_\mu \psi_q - m_q \psi_q^\dagger \psi_q - \frac{1}{4} G_{\mu\nu} \cdot G^{\mu\nu}. \tag{2.17}$$

The gluon kinetic tensor $G^{\mu\nu}$ is

$$G_{a\mu\nu} = \partial_\mu G_{a\nu} - \partial_\nu G_{a\mu} - g_s f_{abc} G_{b\mu} G_{c\nu}. \tag{2.18}$$

The third term in Equation 2.18 corresponds to a self-coupling term, meaning that gluons will couple to gluons as well as to quarks. This is due to the non-Abelian nature of this interaction. One of the important consequences of this feature is that all physical particles must be colorless so there are no free quarks, known as the *quark confinement*. The gluon-gluon coupling also leads to a running strong coupling constant, resulting the *asymptotic freedom*, meaning that the quarks behave like free particles at high momentum transfer.

2.2 W Boson Production and Decay

The inclusive W boson production mechanism in pp collisions is the quark-antiquark annihilation:

$$q\bar{q}' \rightarrow W^\pm + X, \tag{2.19}$$

Where q is an up-type quark and $\bar{q}'$ is a down-type antiquark. There are two types of quarks within the proton: the valence quarks and the sea quark. The valence quarks determine the quantum numbers of hadrons. In the case of proton uud are the three valence quarks. The sea quark are the indefinite number of virtual quark-antiquark pairs that are part of the color field holding the valence quarks together. The W production happens when a valence quark from the proton and a sea antiquark annihilate in a hard scattering process. The remnants of the protons continue down the beam pipe and are ignored. Additional decay products denoted by 'X', often seen

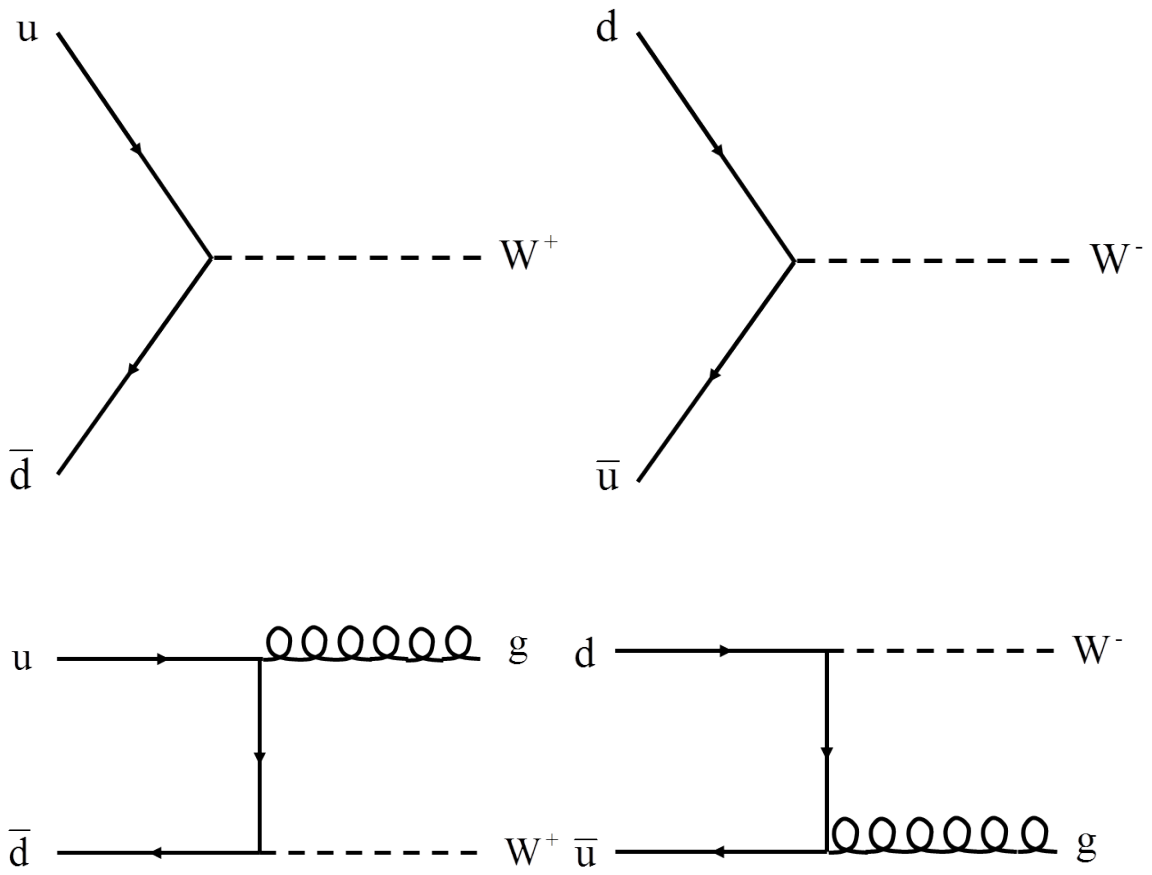

Figure 2.3: The W^+ (left) and W^- (right) boson production processes. In the lowest order diagrams in the top row, the quark and antiquark annihilate. Either quark and antiquark can radiate gluon, which is considered as higher order corrections as shown in the diagrams in the bottom row.

as jets in the detector, are allowed in this inclusive measurement. Around 28% of the W production is associated with jets with jet transverse momentum threshold at 20 GeV. The W^+ and W^- production subprocess are illustrated in Figure 2.3. The lowest order diagram is simply the quark-antiquark annihilation. The next higher order diagrams includes initial state gluon radiation and final state gluon radiation. The W boson can also be produced by c and s quarks, however at a much lower rate.

The W^+ production cross section is given by [31]

$$\hat{\sigma}(q\bar{q}' \to W^+) = 2\pi|V_{qq'}|^2\frac{G_F}{\sqrt{2}}M_W^2\delta(\hat{s} - M_W^2), \tag{2.20}$$

where $V_{qq'}$ is the CKM matrix element connecting the two quark flavors and $\hat{s} = (p_q + p_{\bar{q}'})^2$ is the square of the center-of-mass energy of the $q\bar{q}'$ system. To get the cross section for W^- production, one only need to change q to a down-type quark and $\bar{q}'$ to an up-type antiquark.

To obtain the total W production cross section from the subprocess cross section, one needs to know the distributions of quarks within the colliding protons, the parton distribution functions (PDFs). Theoretical predictions of the W boson production cross section made using MSTW 08 NNLO PDF [42] will be compared to measurement using the first year ATLAS data at the LHC in this thesis. Figure 2.4 shows the MSTW 08 NNLO PDF with different Q^2 values.

The invariant mass of the subprocess is determined by the W boson mass:

$$\sqrt{\hat{s}} = \mid x_1 p_1 + x_2 p_2 \mid = \sqrt{x_1 x_2 s} \equiv M_W \approx 80\ GeV, \tag{2.21}$$

where p_1 and p_2 are the 4-momenta of the colliding protons. x_1 and x_2 are the corresponding momentum fractions. The center-of-mass of the 2010 run at the LHC is $\sqrt{s} = 7\ TeV$ and the typical momentum fraction for W boson production is about $x = 0.01$. From Figure 2.4 one can see that the two u quarks carry more momentum than the d quark at this x value. So the W^+ production is dominant compared to W^- as a result of the reactions between valence quark and sea antiquark. On the other hand, the interaction between sea quarks does not create an asymmetry in W^+ and W^- production. This thesis also measures this $W^\pm$ charge asymmetry.

The total W boson production cross section is:

$$\begin{aligned}\sigma(pp \to W + X) =& \frac{2K_W(\alpha_s)}{3} \int_0^1 dx_1 \int_0^1 dx_2 \sum_{(q,\bar{q}')} [q_1(x_1, M_W^2)\bar{q}_2'(x_2, M_W^2) \\ &+ (q \leftrightarrow \bar{q}')]\hat{\sigma}(q\bar{q}' \to W^+),\end{aligned} \tag{2.22}$$

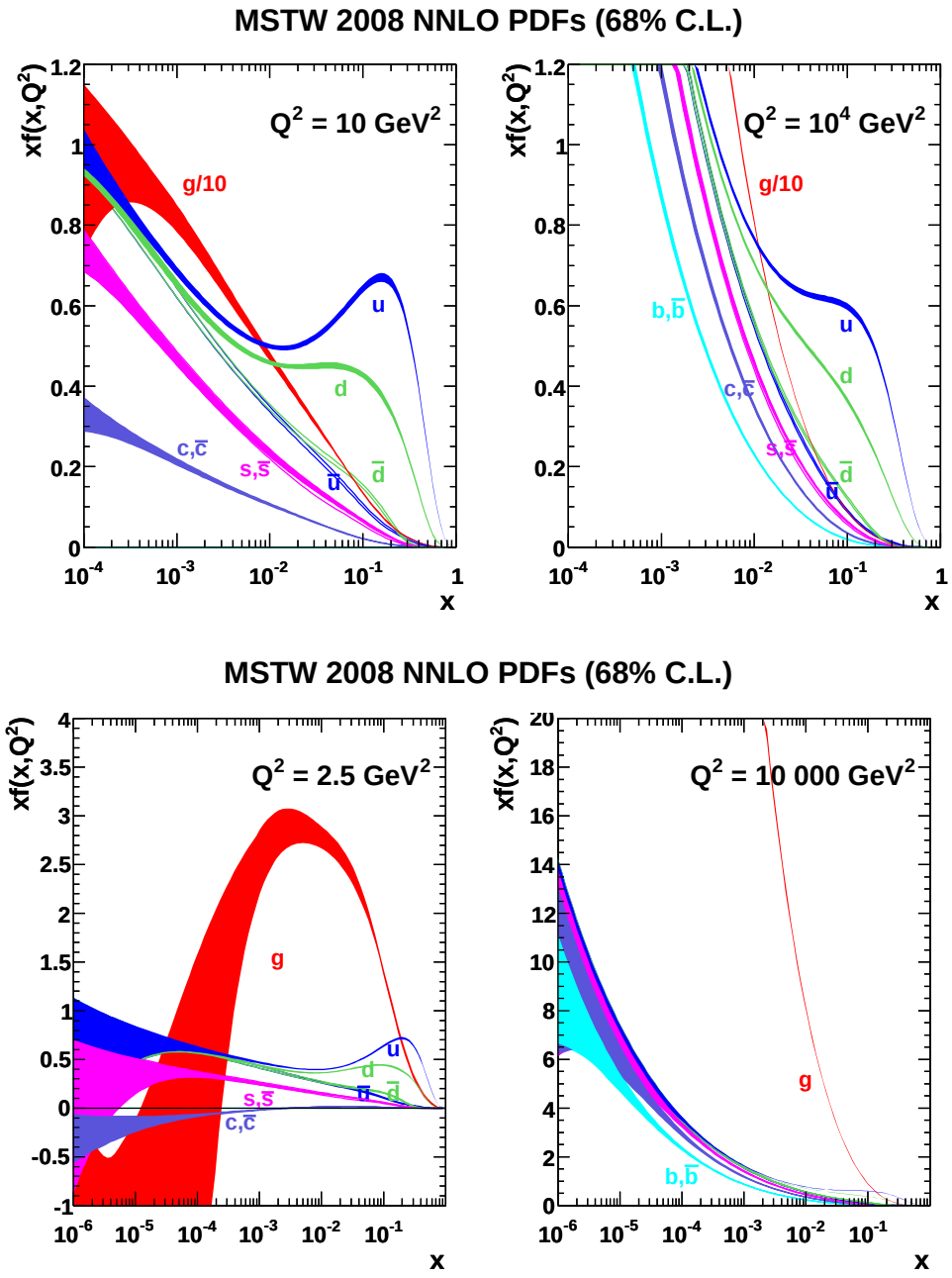

Figure 2.4: The MSTW 2008 NNLO PDFs (68% C.L.), with different Q^2 values. The x value ranges from 10^{-4} to 1 in the top two plots. The bottom two plots are for low x values.

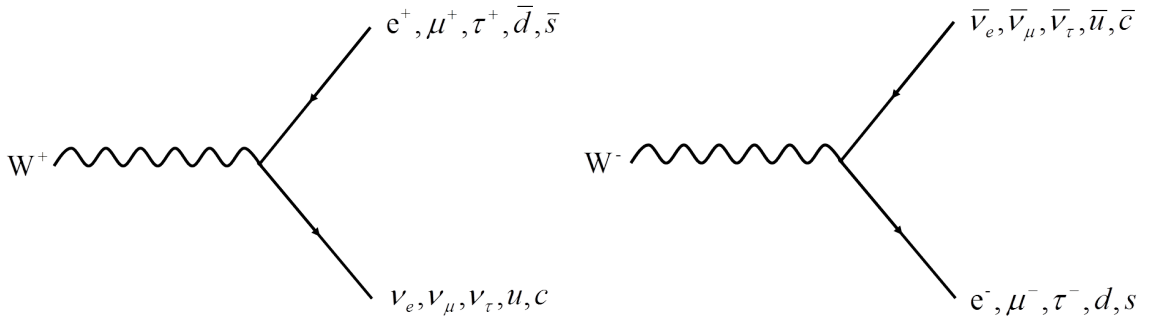

Figure 2.5: The W^+ boson (left) and W^- boson (right) decay modes allowed in Standard Model.

where the factor of 1/3 comes from the requirement that the quark and antiquark colors cancel to form a colorless W, the factor of 2 is for both W^+ and W^- production, q and $\bar{q}'$ are the quark densities at the specified momentum fraction and scale, and the factor $K_W(\alpha_s)$ represents QCD corrections.

W bosons are unstable particles with a lifetime on the order of 10^{-25} s. The principle decay modes allowed in the SM are shown in Figure 2.5. The branching ratio is $B(W \to l\nu) = 10.822\%$, here l =electron, muon or tau. The electron and muon final states are often studied because they are easy to identify with clean experimental signals. This thesis focuses on the $W \to \mu\nu$ decay.

Figure 2.6 shows the rapidity distributions of W^+ and W^- based on the MSTW 08 NNLO pdf set. The rapidity distribution is symmetric about 0. The W^+ and W^- have distinctive shapes.

Using the programs FEWZ [27] with the MSTW 08 NNLO structure function parameterization, the theoretical predictions of the W production cross section are found to be [9]:

$$\sigma_{W^+ \to l^+\nu} = 6.16 \pm 0.31 \; nb, \tag{2.23}$$

$$\sigma_{W^- \to l^-\nu} = 4.30 \pm 0.21 \; nb, \tag{2.24}$$

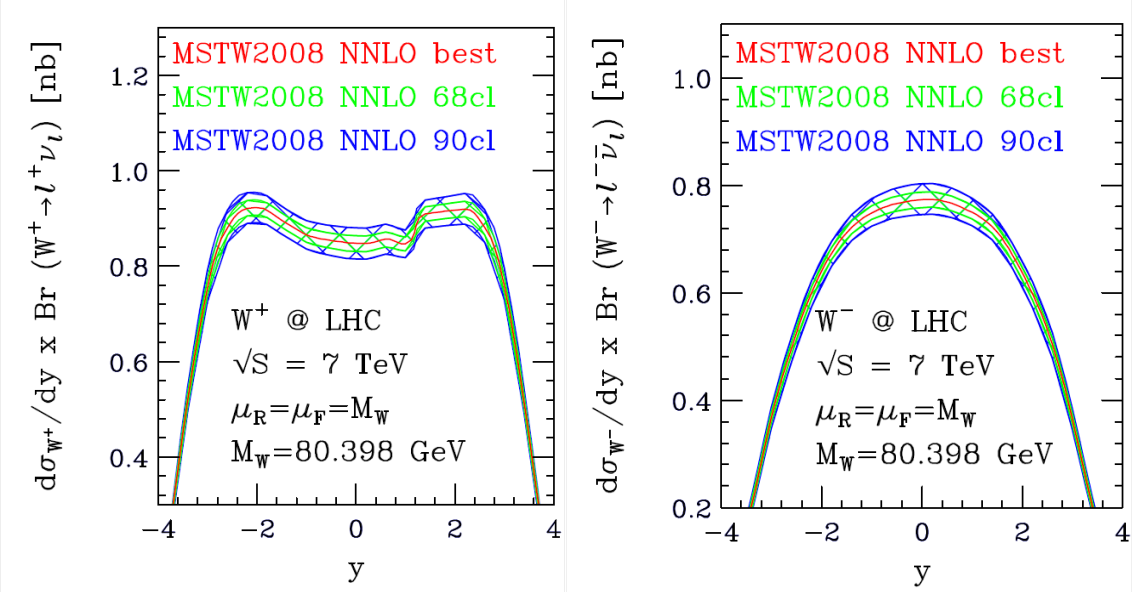

Figure 2.6: The rapidity distribution for W^+ (left) and W^- (right) boson with 68% and 90% confidence level for LHC at $\sqrt{s} = 7\ TeV$ [25].

$$\sigma_{W\to l\nu} = 10.46 \pm 0.52\ nb, \tag{2.25}$$

Equation 2.23 and 2.24 are the cross sections for each lepton flavor of W^+ and W^-, respectively. Equation 2.25 is the total W cross section. The total uncertainty of the cross section is ±5%, which includes 3% from the choice of PDF and 4% from factorization and renormalization scale dependence and size of the correction from NLO to NNLO. The 3% was estimated using the MSTW 08 NNLO PDF error eigenvectors at the 90% C.L. limit, variations of α_s in the range 0.1145-0.1176. The 4% is based on variations of the renormalization and factorization scales by factors of two around the nominal scales $\mu_R = \mu_F = m_W$.

Based on the calculations of the cross section, the ratio of W^+ and W^- cross section is found to be

$$\frac{\sigma_{W^+\to l^+\nu}}{\sigma_{W^-\to l^-\nu}} = 1.433 \times (1.000^{+0.022}_{-0.014}) = 1.433^{+0.032}_{-0.020}. \tag{2.26}$$

The above theoretical predictions will be compared with the W cross section measurements in Chapter VIII.

2.3 Physics Beyond the Standard Model

The Standard Model (SM) has been very successfully predicting and describing almost all measurements performed within its domain. However, as a particle physics theory, it cannot explain the constitutes of dark matter observed in astrophysics experiments. Furthermore, several fundamental theoretical questions remain unresolved. For example, the mechanism for electroweak symmetry breaking described in the SM has not been experimentally confirmed. Many parameters in the SM still lack theoretical explanations. The SM is not an ultimate fundamental theory, but a good approximation of nature at the energy ranges that have been so far accessible to experiment.

New heavy gauge bosons have been predicted by many theories beyond the Standard Model. For example, the Grand Unified Theories (GUT) [41], various Left-Right Symmetric Models (LRSM) [41, 44], extra-dimension theories [28], dynamical symmetry breaking models [32] and even models inspired from superstrings [39]. The unprecedented center-of-mass energy at the LHC will probe regions that are inaccessible at previous experiments. The discovery of a new heavy resonance would open a new era in our understanding of elementary particles and their interactions.

The W' particle is defined as any spin-1 and charged gauge boson that is not included in the SM. Such a new gauge boson with mass below 5-6 TeV can be directly observed at the LHC [11].

This thesis describes a search for a "Standard Model-like" W' boson from the extended gauge models [26]. The W' in these models has Standard Model-like couplings to fermions and its decays to W and Z bosons are suppressed. The search is focused on the high mass signature in the muon-neutrino transverse mass spectrum.

2.4 Units

In this thesis, *natural units* is used. The natural unit is the customary unit system in particle physics, where $\hbar \equiv c \equiv 1$. In this case, energy, momentum and mass can all be expressed using the unit of energy in GeV. The conversion factors for the second and fermi are provided in Equation 2.27 and 2.28, respectively.

$$1\ GeV = 1.517 \times 10^{24}\ s^{-1} \tag{2.27}$$

$$1\ GeV = 5.068\ fm^{-1} \tag{2.28}$$

CHAPTER III

LHC and the ATLAS Detector

3.1 The Large Hadron Collider

The Large Hadron Collider (LHC) [35] at CERN is a two-ring-superconducting-hadron accelerator and collider with a 26.7 km tunnel that were originally built for the CERN LEP machine. The tunnel lies between 45 m and 170 m below the ground on a inclined plane of 1.4%. The four major experiments hosted by LHC are ATLAS, CMS, ALICE and LHCb, as shown in Figure 3.1. ATLAS and CMS are two large general purpose detectors for high luminosity experiments to probe physics at the TeV energy scale. The heavy ion detector ALICE will look at Pb-Pb ion collisions and examine properties of quark-gluon plasma. LHCb is designed for b-physics to study the CP-violation and quark mixing.

The basic layout of the LHC is illustrated in Figure 3.2. The tunnel consists of eight arcs and eight straight sections. Each straight section is approximately 528 m long. Four of them serve as insertions for the four experiments: ATLAS experiment at point 1, CMS experiment at point 5, Point 2 and Point 8 for ALICE and LHC-b as well as the two injection systems for Beam 1 and Beam 2, respectively. The two beams cross at the four interaction points in order to keep the same circumference so that the beams can collide synchronistically. The two sections at Point 3 and 7 each contain two collimation systems to remove off-momentum and beam halo particles.

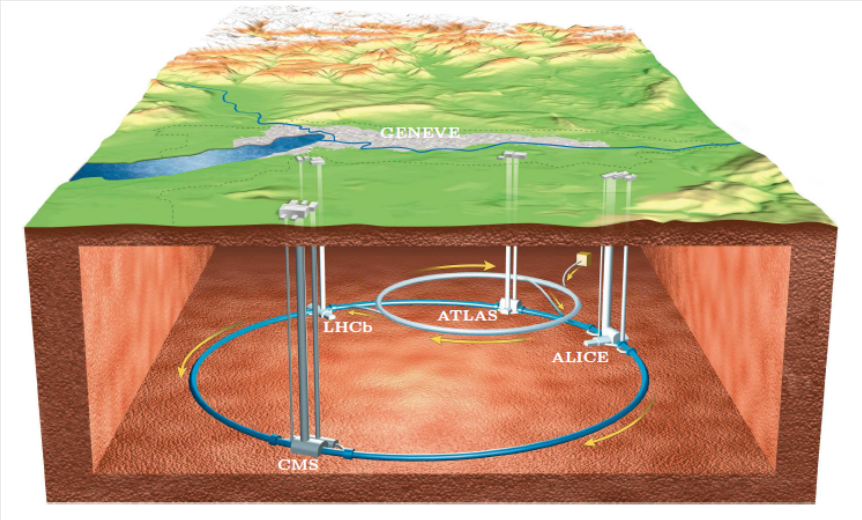

Figure 3.1: Schematic overview of the LHC experiments [35]

The insertion at Point 4 houses two Radio Frequency (RF) systems operating independently for each beam. The straight section at Point 6 includes the beam dumping system. Each of the eight LHC lattice arcs is made of 23 regular arc cells, which are 106.9 m long and consist of a cryostat, short straight section (SSS) assembly and dipole magnets. This design is optimized for a maximum integrated dipole field along the arc with a minimum number of magnet interconnections and with the smallest possible beam envelopes.

In order to achieve a designed center-of-mass of 14 TeV, the beams have to pass a full chain of accelerators. Figure 3.3 is a layout of the LHC injection and acceleration scheme. The protons are first injected by an ion source to a Radio-Frequency cavity and achieve an energy of 750 KeV. Then they enter a Linear Accelerator (LINACS2) with circumference of 30m to be accelerated to 120 MeV before being injected to the 1.4 GeV Proton Synchrotron Booster (PSB). The Proton Synchrotron accelerates the beam to 25 GeV and also generates the LHC bunch structure with 25 ns spacings and 2808 bunches for each proton beam. The beam is later injected to the Super Proton Synchrotron (SPS) and accelerated to 450 GeV, and finally into the two LHC rings to achieve the nominal energy. The protons gain on average 0.5 MeV on each turn at

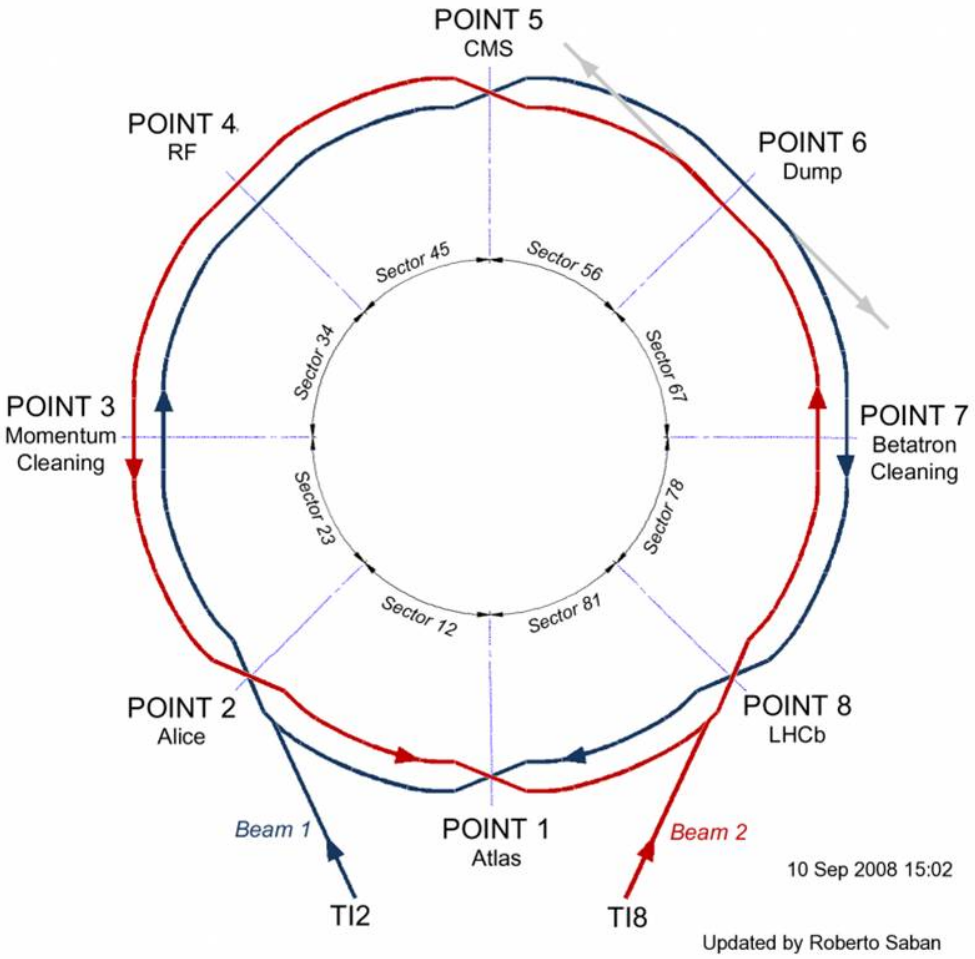

Figure 3.2: Schematic layout of the LHC (Beam 1 - clockwise, Beam 2 - anticlockwise). The ATLAS experiment is located at Point 1 and the CMS experiment at Point 5. The other two experiments ALICE and LHCb are at Point 2 and 8, respectively. The beams cross from one magnet bore to the other at these four locations. [35]

the LHC which makes it around 20 minutes for the beam to achieve 7 TeV from 450 GeV. Acceleration is driven by the electric fields that are fed into the RF cavities. The LHC RF system is operating at 400 MHz which creates the bunch structure. It is composed of 16 superconducting cavities, 8 cavities for each beam with a peak accelerating voltage of 16 MV.

One of the biggest challenges that the LHC has is the unprecedented design luminosity of $10^{34}\ cm^{-2}s^{-1}$. The event rate for a given physics process with cross section σ is proportional to the luminosity L.

$$N = L\sigma \tag{3.1}$$

The machine luminosity depends only on the beam parameters and can be written for a Gaussian beam distribution as Equation 3.2.

$$L = \frac{N_b^2 n_b f_{rev} \gamma_r}{4\pi\epsilon_n \beta^*} F \tag{3.2}$$

where N_b is the number of particles per bunch, n_b is the number of bunches per beam, f_{rev} is the revolution frequency, γ_r is the relativistic gamma factor, ϵ_n is the normalized transverse beam emittance, β^* is the beta function at the collision point, and F is the geometric luminosity reduction factor due to the crossing angle at the interaction point (IP). Therefore, both high beam intensities and high beam energies are required for the exploration of rare events in the LHC.

The high beam intensity required for the LHC excludes the use of proton-anti-proton beams. Therefore, separate magnet system and vacuum chambers are necessary to collide two counter-rotating proton beams. In order to incorporate two proton rings into a tunnel with an internal diameter of only 3.7 m, a two-in-one super-conducting magnet design is adopted, where two sets of coils and beam channels are installed within the same mechanical structure and cryostat. In Figure 3.4,

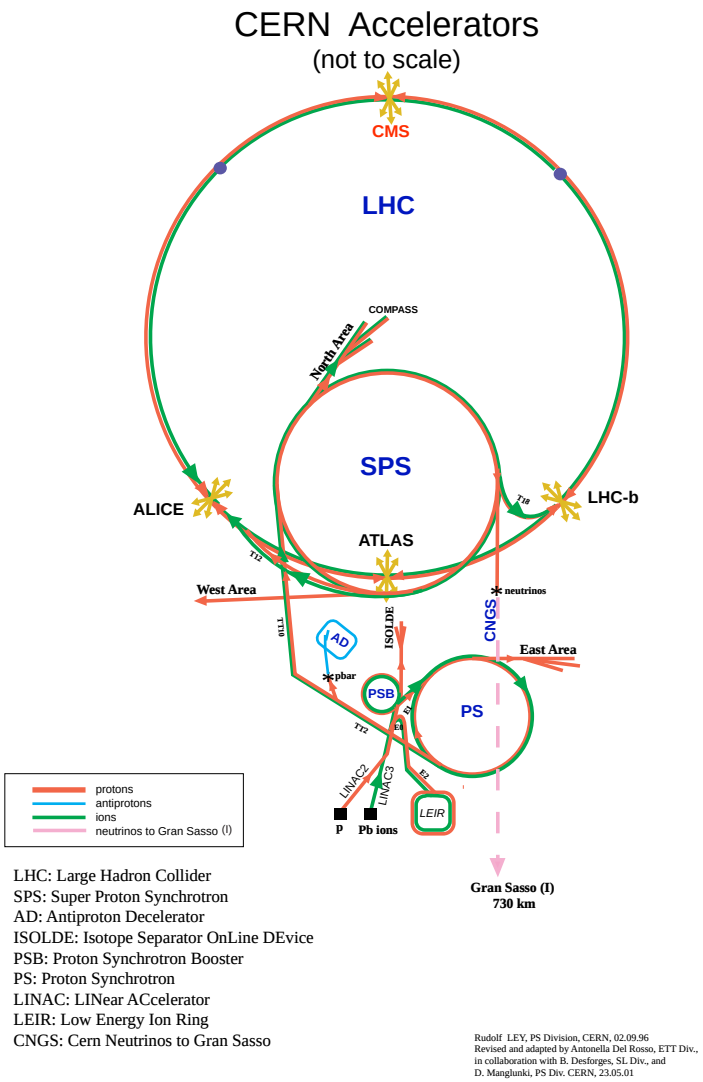

Figure 3.3: LHC and its injectors. The proton source is accelerated to 7 TeV through a series of accelerators: LINAC2, PSB, PS, SPS and finally LHC. [35]

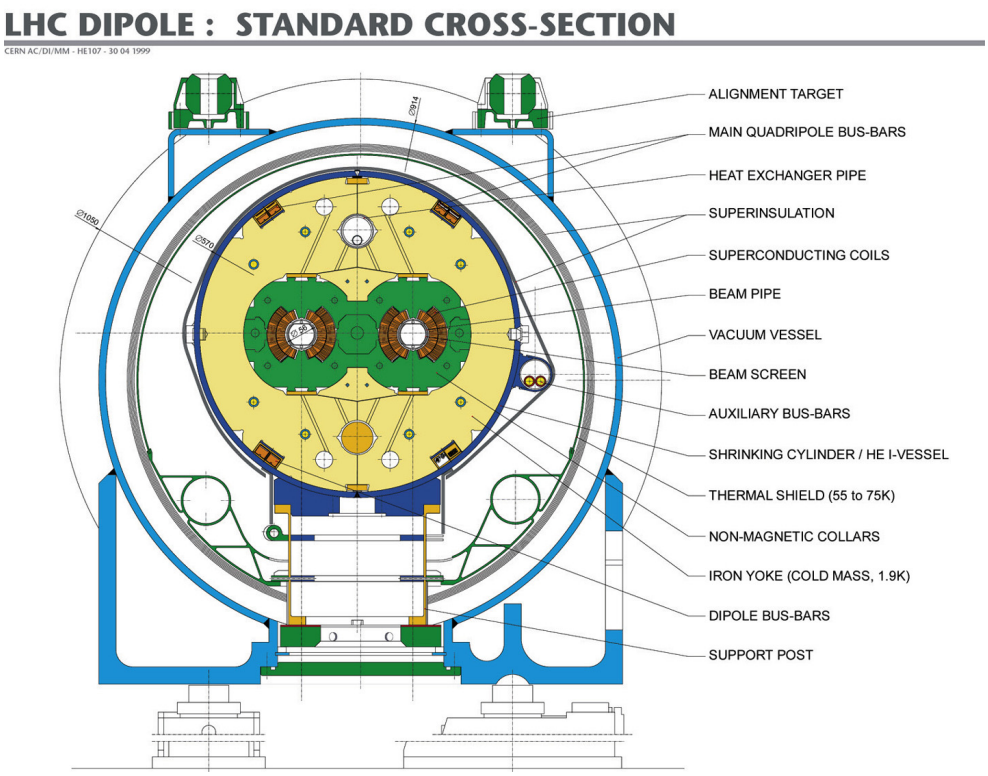

Figure 3.4: Cross-section of the LHC dipole [35]

one can see the cross-section of the dipole and the positions of the two beam pipes. The peak beam energy depends on the integrated dipole field around the storage ring. The nominal field is 8.33 Tesla, corresponding to an energy of 7 TeV. The NbTi superconduction magnets are cooled to less than 2 K with superfluid helium at 1.9 K so that a high dipole field can be achieved. Throughout the LHC a total of 1232 dipole magnets are used to bend the beam and define the reference path. The focusing of the beam is achieved using quadrupole magnets. Because a single quadrupole field can only focus the beam in one plane, alternating focusing and defocussing quadrupoles are installed to focus the beam in both horizontal and vertical planes. Figure 3.5 shows the LHC arc lattice in a LHC cell. The sextupole magnets correct the trajectories for off-momentum particles. There are also multipole-corrector magnets installed along the beam line used to compensate field imperfections of the dipole magnets and to stabilize the trajectories for particles at larger amplitudes.

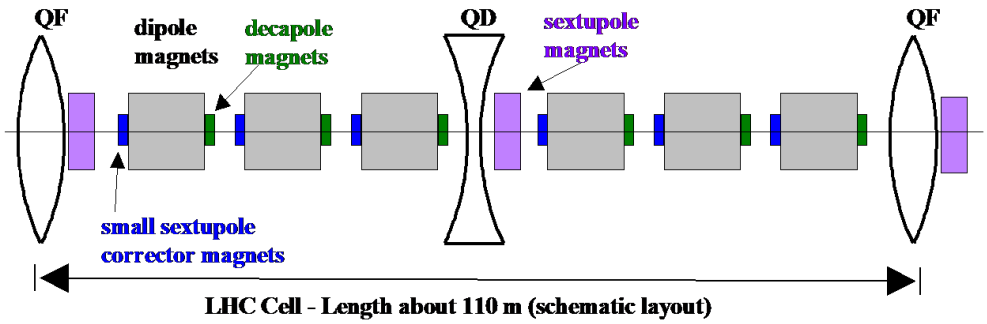

Figure 3.5: Magnets in the LHC arc lattice [35]

3.2 The ATLAS Detector

The ATLAS (A Toroidal LHC ApparatuS) detector [12] is one of the two general purpose detectors at the LHC. It is the largest detector ever built at a particle collider. The detector is a cylinder with a total length of 44 meters and a radius of 11 meters. The weight is approximately 7000 tonnes. Figure 3.6 shows the overall layout of the ATLAS detector. One can also see the size of the detector in comparison with a human body from this picture. The ATLAS detector consists of four major components, the inner tracker which measures the momentum of the charged particles, the calorimeter which measures the energies carried by the particles, the muon spectrometer which identifies and measures muons and the magnet system that bends charged particles for momentum measurement. Each of these four components will be addressed in Section 3.2.1, and Section 3.2.2- 3.2.4 in an outside-to-inside order. The expected performance of the sub-detectors are listed in Figure 3.7.

The coordinate system and nomenclature used to describe the ATLAS detector and the particles emerging from the p-p collisions are briefly summarized here, since they will be used repeatedly throughout this thesis. The ATLAS detector is designed to be forward-backward symmetric with respect to the interaction point. This nominal interaction point is defined as the origin of the coordinate system, while the beam direction defines the z-axis and the x-y plane is transverse to the beam direction. The positive x-axis is defined as pointing from the interaction point to the center

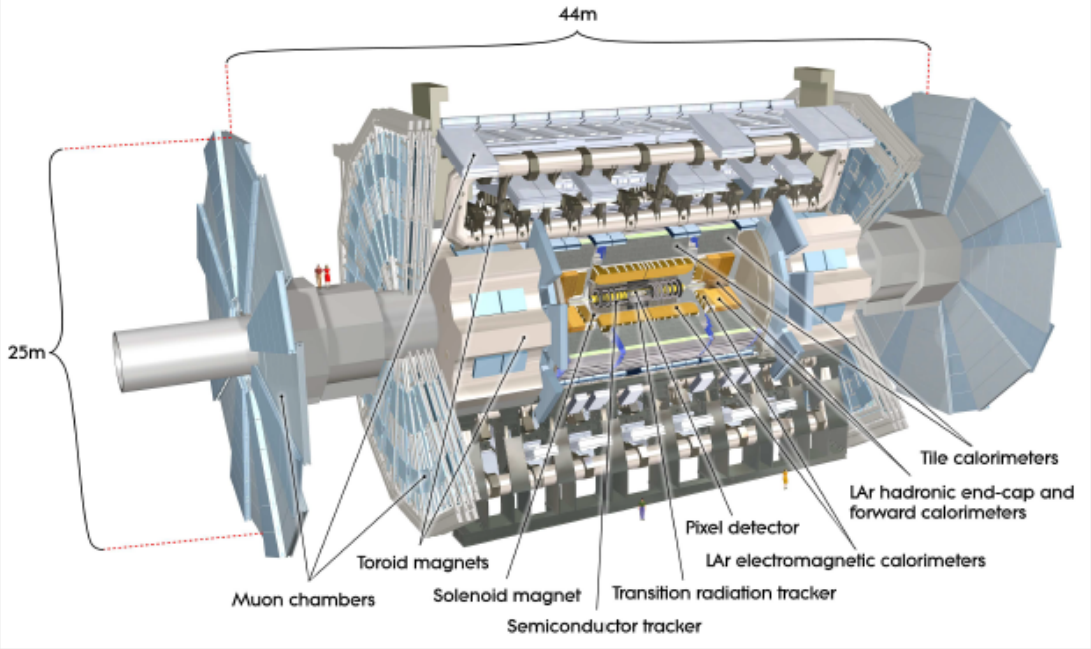

Figure 3.6: Cut-away view of the ATLAS detector showing the sub-systems and overall dimensions [12]

Detector component	**Required resolution**	**η coverage**	
		Measurement	Trigger
Tracking	$\sigma_{p_T}/p_T = 0.05\%\ p_T \oplus 1\%$	± 2.5	
EM calorimetry	$\sigma_E/E = 10\%/\sqrt{E} \oplus 0.7\%$	± 3.2	± 2.5
Hadronic calorimetry (jets)			
barrel and end-cap	$\sigma_E/E = 50\%/\sqrt{E} \oplus 3\%$	± 3.2	± 3.2
forward	$\sigma_E/E = 100\%/\sqrt{E} \oplus 10\%$	$3.1 < \lvert\eta\rvert < 4.9$	$3.1 < \lvert\eta\rvert < 4.9$
Muon spectrometer	σ_{p_T}/p_T=10% at p_T = 1 TeV	± 2.7	± 2.4

Figure 3.7: General performance goals of the ATLAS detector [12]

of the LHC ring. The positive y-axis is defined as pointing upwards. The side-A of the detector is the side with positive z, while side-C is that with negative z. The azimuthal angle ϕ is measured as usual around the beam axis. The polar angle θ is the angle from the beam axis. The rapidity used for massive objects such as jets is defined as $Y = 1/2 \ln[(E + p_z)/(E - p_z)]$. The pseudorapidity is defined as $\eta = -\ln \tan(\theta/2)$. In the relativistic limit, $E \gg mc^2$, the pseudorapidity approaches numerically to the rapidity. The distance ΔR in the pseudorapidity-azimuthal angle space is defined as $\Delta R = \sqrt{\Delta\eta^2 + \Delta\phi^2}$. The transverse momentum p_T, the transverse energy E_T and the missing transverse energy E_T^{miss} are defined in the x-y plane unless stated otherwise.

3.2.1 Magnet System and Magnetic Field

The magnet system as shown in Figure 3.8 comprises a thin superconducting solenoid surrounding the inner-detector cavity and three large superconducting toroids arranged with an eight-fold azimuthal symmetry around the calorimeters. There is one long toroid for the barrel and two inserted end-cap toroids. The main parameters of the magnet system are summarized in Figure 3.9.

The solenoid is aligned on the beam axis. It provides a 2 T axial magnetic field for the inner detector. It is designed to minimize the radiative thickness in front of the barrel electromagnetic calorimeter. Figure 3.10 shows the bare central solenoid after completion of the coil winding.

The air-core barrel toroid and the endcap toroids produce a toroidal magnetic field of approximately 0.5 T and 1 T for the muon detectors in the barrel and endcap region, respectively. Figure 3.11 shows the barrel toroid as installed in the underground cavern. The air-core magnet concept minimizes the amount of material traversed by the muons after exiting the calorimeters. The endcap toroid coil system is rotated by 22.5° with respect to the barrel toroid coil system in order to provide radial overlap

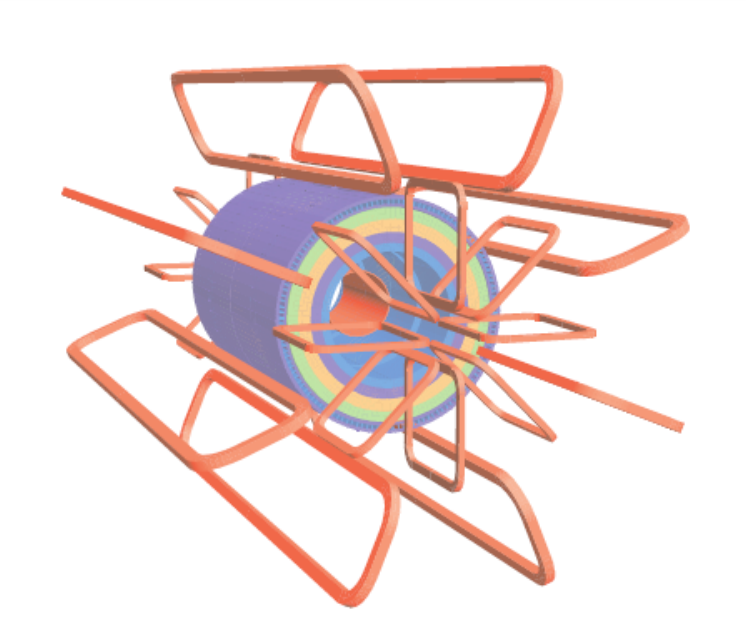

Figure 3.8: Geometry of magnet windings and tile calorimeter steel [12]. There are eight barrel toroid coils. The solenoid winding is inside the calorimeter.

Property	Feature	Unit	Solenoid	Barrel toroid	End-cap toroids
Size	Inner diameter	m	2.46	9.4	1.65
	Outer diameter	m	2.56	20.1	10.7
	Axial length	m	5.8	25.3	5.0
	Number of coils		1	8	2×8
Mass	Conductor	t	3.8	118	2×20.5
	Cold mass	t	5.4	370	2×140
	Total assembly	t	5.7	830	2 x 239
Coils	Turns per coil		1154	120	116
	Nominal current	kA	7.73	20.5	20.5
	Magnet stored energy	GJ	0.04	1.08	2 x 0.25
	Peak field in the windings	T	2.6	3.9	4.1
	Field range in the bore	T	0.9–2.0	0.2–2.5	0.2–3.5
Conductor	Overall size	mm^2	30 x 4.25	57 x 12	41 x 12
	Ratio Al:Cu:NbTi		15.6:0.9:1	28:1.3:1	19:1.3:1
	Number of strands (NbTi)		12	38–40	40
	Strand diameter (NbTi)	mm	1.22	1.3	1.3
	Critical current (at 5 T and 4.2 K)	kA	20.4	58	60
	Operating/critical-current ratio at 4.5 K	%	20	30	30
	Residual resistivity ratio (RRR) for Al		> 500	> 800	> 800
	Temperature margin	K	2.7	1.9	1.9
	Number of units $\times$ length	m	4×2290	$8 \times 4 \times 1730$	$2 \times 8 \times 2 \times 800$
	Total length (produced)	km	10	56	2 x 13
Heat load	At 4.5 K	W	130	990	330
	At 60–80 K	kW	0.5	7.4	1.7
	Liquid helium mass flow	g/s	7	410	280

Figure 3.9: Parameters of the ATLAS magnet system [12]

Figure 3.10: Picture of the barrel solenoid [12]

and to optimize the bending power at the interface between the two coil systems. The bending power is characterized by the field integral $\int B\,dl$, where B is the field component normal to the muon direction and the integral is computed along an infinite-momentum muon trajectory, between the inner-most and outer-most muon chamber planes. As shown in Figure 3.12, the barrel toroid provides 1.5 to 5.5 Tm of bending power in the pseudorapidity range $|\eta| < 1.4$, and the endcap toroids approximately 1 to 7.5 Tm in the region $1.6 < |\eta| < 2.7$. The bending power is lower in the transition regions $1.4 < |\eta| < 1.6$ where the two magnets overlap.

3.2.2 Muon Spectrometer

The Muon Spectrometer (MS) forms the outer part of the ATLAS detector. It is designed to detect charged particles exiting the barrel and endcap calorimeters and to measure their momentum in the pseudorapidity range $|\eta| < 2.7$. It is also designed to

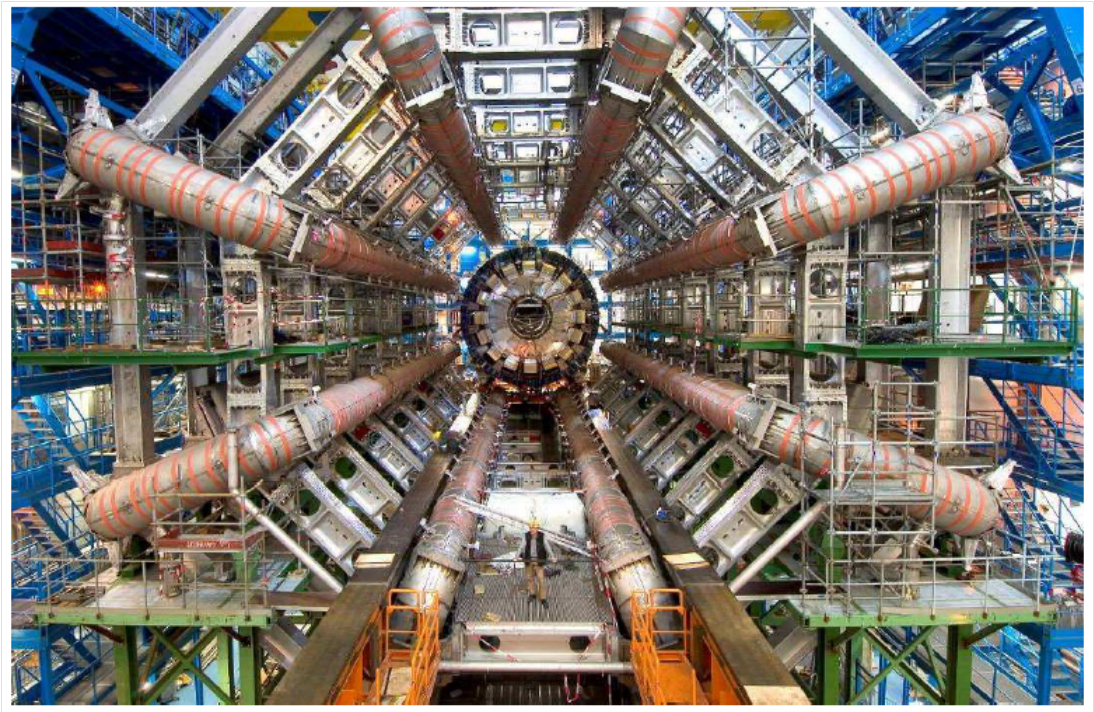

Figure 3.11: Picture of the barrel toroid [12]

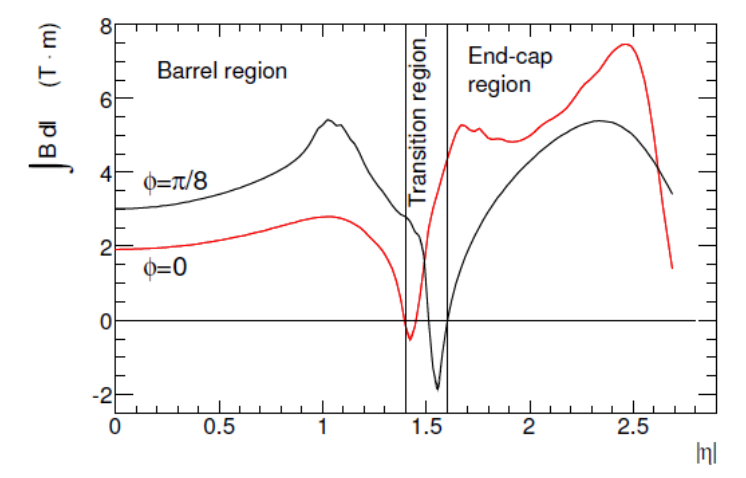

Figure 3.12: The integrated magnetic field strength of the toroids as a function of $|\eta|$ [12]

trigger on these particles in the region $|\eta| < 2.4$. The layout of the Muon Spectrometer (MS) is shown in Figure 3.13. The MS consists of high-precision tracking chambers and separate trigger chambers. The Monitored Drift Tubes (MDT) and Cathode Strip Chambers (CSC) are the two types of tracking chambers, while the Resistive Plate Chambers (RPC) and Thin Gap Chambers (TGC) are instrumented for trigger purpose. The design parameters of the muon chambers are listed in Figure 3.14 and Table 3.1.

Figure 3.15 shows the cross-section of the muon system in the bending plane, illustrating the positioning of all the chambers. The chambers in the barrel are arranged in three cylindrical layers around the beam axis forming three barrel stations. There are also three stations in each of the endcap region in the form of three disks perpendicular to the beam line at increasing distance from the interaction point. A high-p_T muon typically traverses all three stations but there are regions with support structures or passages for service that do not provide all three precision measurements. There are also regions with overlapped chambers allowing two measurements from a single station. Figure 3.16 shows the number of station measurements as a function of η and ϕ.

The expected momentum resolution and pseudorapidity coverage of the MS is included in Figure 3.7. It is important to note that the muon spectrometer performance as given in this Table is independent of the inner detector. The ATLAS muon system is a stand-alone muon spectrometer with approximately 10% transverse momentum resolution for 1 TeV tracks, which translates into a sagitta along the beam axis of about 500 μm, to be measured with a resolution of $\leq$ 50 μm. Muon momenta down to a few GeV (about 3 GeV, due to energy loss in the calorimeters) may be measured by the spectrometer alone. Figure 3.17 shows the contributions to the muon spectrometer momentum resolution for a p_T range from 0 to a few TeV. At low momentum, the resolution is dominated by fluctuations in the energy loss of

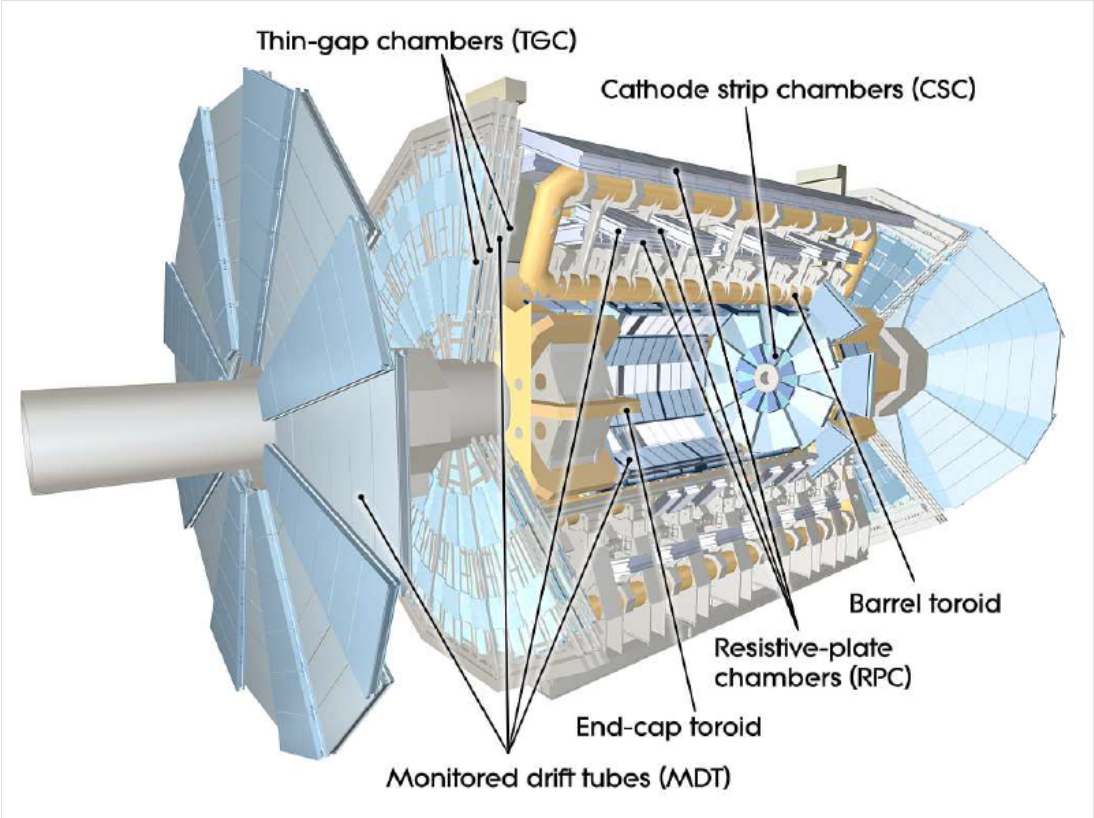

Figure 3.13: Cut-away view of the ATLAS muon system [12]

the muons passing through the material in front of the muon spectrometer. Multiple scattering plays an important role in the intermediate momentum range. For muons with $p_T > 250\ GeV/c$, the dominant contribution is from the single-hit resolution, limited by detector characteristics, alignment and calibration.

Table 3.1: Parameters of the four sub-systems of the muon spectrometer [12]

		Chamber resolution (RMS) in			**Measurements/track**		**Number of**	
Type	**Function**	z/R	ϕ	time	barrel	end-cap	chambers	channels
MDT	Precision	35 μm (z)	—	—	20	20	1150	354k
CSC	Precision	40 μm (R)	5 mm	7 ns	—	4	32	30.7k
RPC	Trigger	10 mm (z)	10 mm	1.5 ns	6	—	606	373k
TGC	Trigger	2-6 mm (R)	3-7 mm	4 ns	—	9	3588	318k

3.2.2.1 Monitored Drift Tube

The precision momentum measurement is performed by the Monitored Drift Tube chambers (MDT) in the majority of the pseudorapidity coverage region. The MDTs

Monitored drift tubes	**MDT**
- Coverage	$\|\eta\| < 2.7$ (innermost layer: $\|\eta\| < 2.0$)
- Number of chambers	1088 (1150)
- Number of channels	339 000 (354 000)
- Function	Precision tracking
Cathode strip chambers	**CSC**
- Coverage	$2.0 < \|\eta\| < 2.7$
- Number of chambers	32
- Number of channels	31 000
- Function	Precision tracking
Resistive plate chambers	**RPC**
- Coverage	$\|\eta\| < 1.05$
- Number of chambers	544 (606)
- Number of channels	359 000 (373 000)
- Function	Triggering, second coordinate
Thin gap chambers	**TGC**
- Coverage	$1.05 < \|\eta\| < 2.7$ (2.4 for triggering)
- Number of chambers	3588
- Number of channels	318 000
- Function	Triggering, second coordinate

Figure 3.14: Main parameters of the muon system [12]

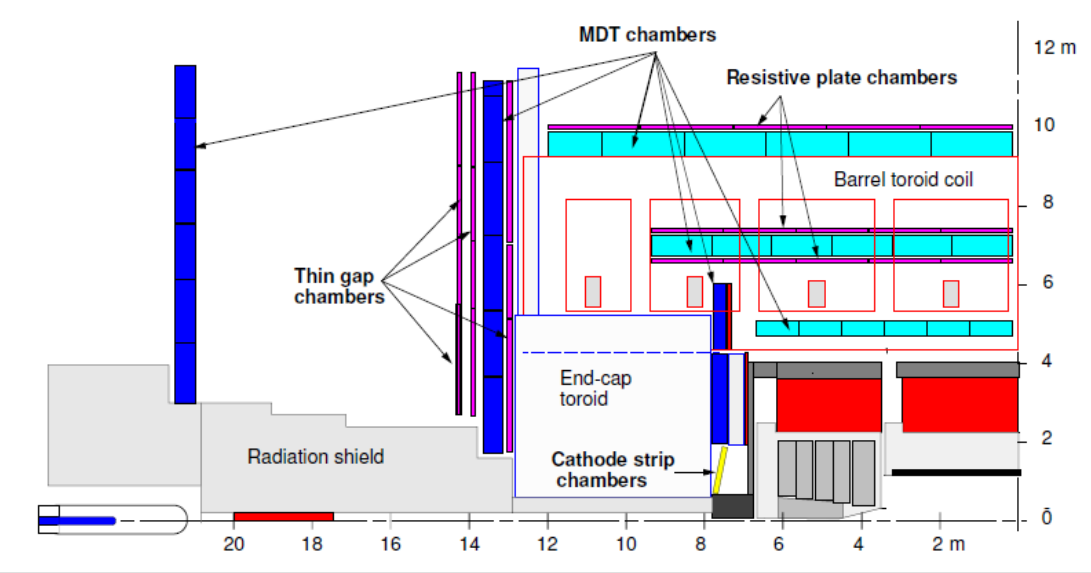

Figure 3.15: Cross-section of the muon system in a plane containing the beam axis [12]

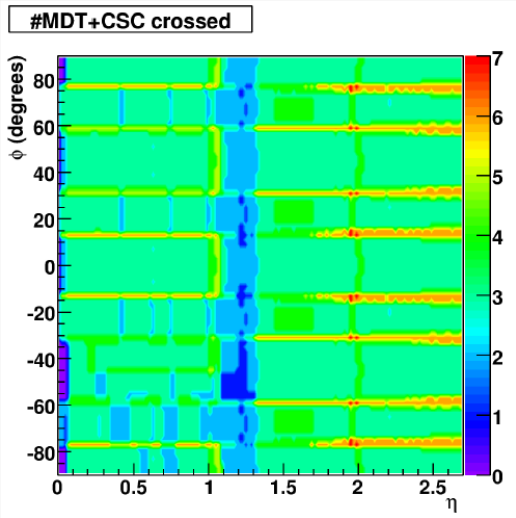

Figure 3.16: Number of muon detector stations traversed by muons as function of $|\eta|$ and ϕ [12]

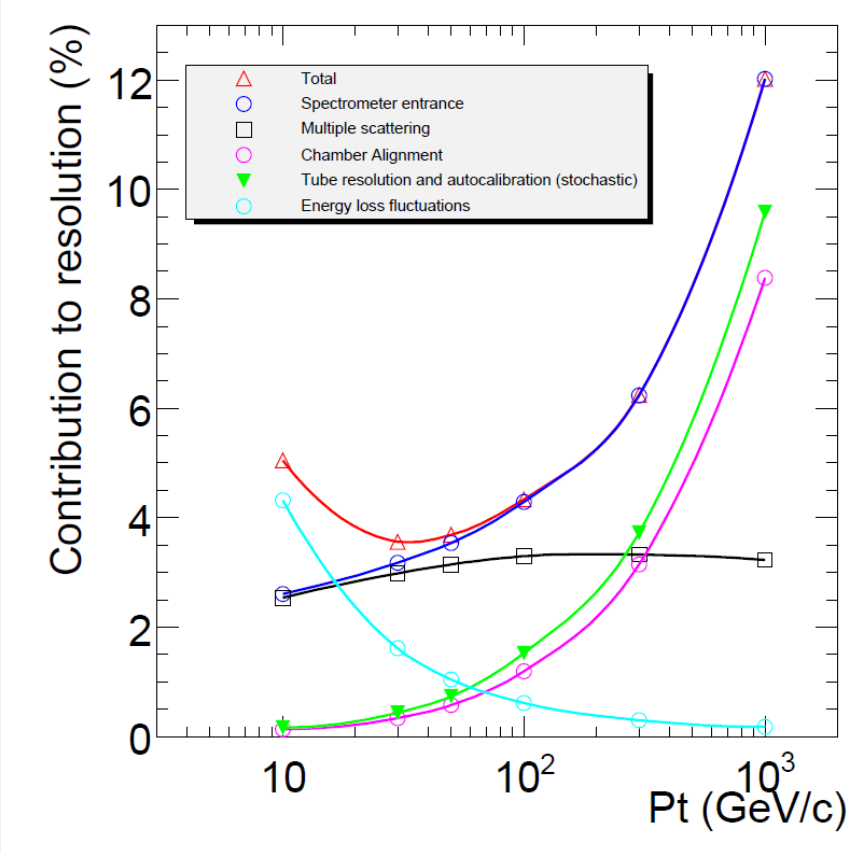

Figure 3.17: Contributions to the momentum resolution for the muon spectrometer as a function of transverse momentum for $|\eta| < 1.5$ [12]

cover the pseudorapidity range $|\eta| < 2.7$ (except in the inner most endcap layer where the coverage is limited to $|\eta| < 2.0$). The MDTs measure the track coordinates in the principal bending direction of the magnetic field, and hence are also referred t oas precision tracking chambers. The basic element of the MDT chambers is a pressurized drift tube, operating with an Ar/CO_2 (93% and 7%, respectively) gas mixture at 3 *bar* as shown in Figure 3.18. The parameters of the drift tubes is listed in Table 3.2.

The chambers in the barrel are arranged in three cylindrical layers around the beam axis at radii of approximately 5 m, 7.5 m, and 10 m. These three barrel layers are called Barrel Inner (BI), Barrel Middle (BM), and Barrel Outer (BO). In the two endcap regions, the chambers installed in planes perpendicular to the beam at 7.4 m, 10.8 m, 14 m, and 21.5 m from the nominal interaction point are called Endcap Inner (EI), Endcap Extra (EE), Endcap Middle (EM), and Endcap Outer (EO), respectively. An auxiliary set of chambers, called Barrel Endcap Extra (BEE), are installed on the cryostats of the endcap toroids. They are constructed like barrel chambers although functionally they serve in the endcap system. The barrel chambers are rectangular while the endcap chambers are trapezoidal. The chambers' dimensions increase inproportion to their distance from the interaction point. These chambers consist of three to eight layers of drift tubes, with an average resolution of 80 μm per tube, or about 35 μm per chamber.

3.2.2.2 Cathode Strip Chamber

The Cathode Strip Chambers (CSC) are multi-wire proportional chambers with cathode planes segmented into strips in orthogonal directions. This allows both coordinates to be measured from the induced-charge distribution on the two planes of orthogonal strips. The CSCs are used over $2 < |\eta| < 2.7$ in the inner most tracking layer due to their higher rate capability and time resolution. The resolution of a CSC

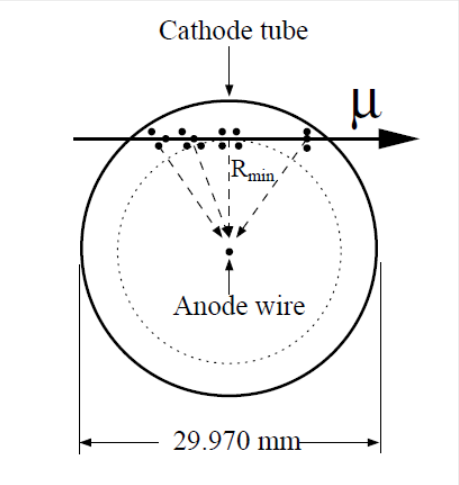

Figure 3.18: Cross-section of a monitored drift tube [12]

Table 3.2: Main MDT chamber parameters [12]

Tube material	Aluminum
Outer tube diameter	29.970 mm
Tube wall thickness	0.4 mm
Wire material	gold-plated W/Re (97/3)
Wire diameter	50 μm
Gas mixture	$Ar/CO_2/H_2O$ (93/7/$\leq$ 1000 ppm)
Gas pressure	3 bar (absolute)
Gas gain	2×10^4
Wire potential	3080 V
Maximum drift time	$\sim$ 750 ns
Resolution per tube	$\sim$ 80 μm

is 40 μm in the bending plane and about 5 mm in the transverse plane. The CSC system consists of two disks, one with eight large chambers and one with eight small ones. Each chamber has four CSC planes, resulting in four independent measurements in η and ϕ directions along the track. The operating parameters of the CSCs are listed in Table 3.3.

Table 3.3: Operating parameters of the CSCs [12]

Operating voltage	1900 V
Anode wire diameter	30 μm
Gas gain	6×10^4
Gas mixture	Ar/CO_2 (80/20)
Total ionization (typical track)	$\sim$ 90 ion pairs

3.2.2.3 Trigger Chambers

An essential design criterion of the muon system was the capability to trigger on muon tracks. The precision-tracking chambers have therefore been complemented by a system of fast trigger chambers capable of delivering track information within a few tens of nanoseconds after the passage of the particle. The muon trigger chambers are required to provide bunch-crossing identification, well-defined p_T thresholds and measurement the muon coordinate in the direction orthogonal to that determined by the precision tracking chambers. The purpose of the precision-tracking chambers is to determine the coordinate of the track in the bending plane. After matching of the MDT and trigger chamber hits in the bending plane, the trigger chamber's coordinate in the non-bending plane is used as the second coordinate of the MDT measurement. The design of the barrel and endcap trigger systems have different requirements. Increased granularity is required in the endcap region because of higher muon momenta for a given p_T with the increase of η, the complexity of magnetic field in the transition region $1.3 \leq |\eta| \leq 1.65$, and the increased radiation levels in the endcap. For these reasons, Resistive Plate Chambers (RPC) are installed for the

barrel region $|\eta| < 1.05$, while Thin Gap Chambers (TGC) are chosen for the endcap region $1.05 < |\eta| < 2.4$.

Resistive Plate Chambers The RPCs are wireless chambers using gaseous parallel electrode-plate technology. They have good spatial and time resolution as well as adequate rate capability. They have two parallel resistive plates made of phenolic-melaminic plastic laminate aseparated by a 2 mm gas gap. The parameters of RPC chambers are listed in Table 3.4. There are two independent RPC layers in each of the three barrel stations, resulting in six measurements in η and ϕ.

Table 3.4: Main parameters and performance of RPC [12]

E field in gap	4.9 kV/mm
Gas gap	2 mm
Gas mixture	$C_2H_2F_4$/Iso-C_4H_{10}/SF_6 (94.7/5/0.3)
Readout pitch of η and ϕ strips	23–35 mm
Intrinsic time jitter	$\leq$ 1.5 ns
Local rate capability	$\sim$ 1 kHz/cm^2

Thin Gap Chambers The TGCs operate on the same principle as multi-wire proportional chambers and measure both coordinates of a track. They have good time resolution and high rate capability. Their spatial resolution is mainly determined by the readout channel granularity, which is set by appropriate wire ganging. The main parameters of TGCs are summarized in Table 3.5. In addition to trigger capability, TGCs provide the second coordinate to complement the measurement of the MDTs. The middle layer of the MDTs in the endcap is complemented by seven layers of TGCs, while the inner layer is complemented by only two layers. The azimuthal coordinate in the outer MDT wheel is obtained by the extrapolation of the track from the middle layer, which can be done accurately due to the lack of magnetic field between EM and EO.

Table 3.5: Main parameters of TGCs [12]

Gas gap	2.8 mm
Wire pitch	1.8 mm
Wire diameter	50 μm
Wire potential	2900 V
Operating plateau	200 V
Gas mixture	CO_2/n-pentane (55/45)
Gas amplification	3×10^5

3.2.2.4 Alignment and Calibration

The muon spectrometer has an optical alignment system. The general process of alignment is to first obtain absolute position information from surveys and calibration of alignment bars, and relative position information from continuous monitoring of chamber motions (translations and rotations from thermal expansion). Then the information must be accurately associated to each chamber by means of a detailed, continuously updated database. The database information is applied during reconstruction.

Success of the muon system resides ultimately on the intrinsic resolution of the drift tubes. In order to obtain the optimal resolution for $>$ 350000 drift tubes distributed in 1200 chambers and changing drift gas, the collaborative efforts of three Tier-2 calibration centers in continuous operation are involved. The calibrations require that drift times be compensated for gas composition variations, temperature variations, both spatial and temporal, pressure variations, magnetic field, off-centered wires, drift time vs. charge dependence and space charge at high radiation rates. The muon drift tube timing offsets ($T0$'s) must be well-measured for MDT calibration as well as the time-to-space relationship be well monitored.

3.2.3 Calorimetry

Shown in Figure 3.19 are the ATLAS sampling calorimeters, which cover the pseudorapidity range of $|\eta| < 4.9$, using different techniques suited to the widely varying

requirements of the physics processes of interest and of the radiation environment over this large η-range. Over the η region matched to the inner detector, the fine granularity of the Electromagnetic (EM) Calorimeter is ideally suited for precision measurements of electrons and photons. The coarser granularity of the rest of the calorimeter is sufficient to satisfy the physics requirements for jet reconstruction and E_T^{miss} measurements. The calorimeters consist of a number of detectors with full ϕ-symmetry and coverage around the beam axis. The calorimeter closest to the beam-line are housed in three cryostats, one barrel and two endcaps. The barrel cryostat contains the EM barrel calorimeter, whereas the two endcap cryostats each contain an EM endcap calorimeter (EMEC), a hadronic endcap calorimeter (HEC), located behind the EMEC, and a forward calorimeter (FCal) to cover the region closest to the beam. All these calorimeters use liquid argon as the active detector medium. Liquid argon has been chosen for its intrinsic linear behavior and its stability of response over time as well as its intrinsic radiation-hardness. The main design parameters for the calorimeter system is listed in Table 3.2.3.

The energy resolution for a calorimeter can be written in the general form

$$\frac{\sigma_E}{E} = \frac{S}{\sqrt{E}} \oplus C \oplus \frac{N}{E}, \tag{3.3}$$

where the first term 'S' is a stochastic or sampling term, the constant term 'C' represents inhomogeneity, mis-calibration and non-linearity, and 'N' represents electronic and pile-up noise. There parameters are pseudorapidity dependent. At high energy, the constant term dominates.

The performance requirement of the calorimeters are mainly set by the Higgs search. The energy resolution is also crucial for many new physics searches because of its importance to the missing transverse energy measurement. The energy resolution

Table 3.6: Main parameters of the calorimeter system [12]

	Barrel		End-cap	
EM calorimeter				
Number of layers and $\|\eta\|$ coverage				
Presampler	1	$\|\eta\| < 1.52$	1	$1.5 < \|\eta\| < 1.8$
Calorimeter	3	$\|\eta\| < 1.35$	2	$1.375 < \|\eta\| < 1.5$
	2	$1.35 < \|\eta\| < 1.475$	3	$1.5 < \|\eta\| < 2.5$
			2	$2.5 < \|\eta\| < 3.2$
Granularity $\Delta\eta \times \Delta\phi$ versus $\|\eta\|$				
Presampler	0.025×0.1	$\|\eta\| < 1.52$	0.025×0.1	$1.5 < \|\eta\| < 1.8$
Calorimeter 1st layer	$0.025/8 \times 0.1$	$\|\eta\| < 1.40$	0.050×0.1	$1.375 < \|\eta\| < 1.425$
	0.025×0.025	$1.40 < \|\eta\| < 1.475$	0.025×0.1	$1.425 < \|\eta\| < 1.5$
			$0.025/8 \times 0.1$	$1.5 < \|\eta\| < 1.8$
			$0.025/6 \times 0.1$	$1.8 < \|\eta\| < 2.0$
			$0.025/4 \times 0.1$	$2.0 < \|\eta\| < 2.4$
			0.025×0.1	$2.4 < \|\eta\| < 2.5$
			0.01×0.1	$2.5 < \|\eta\| < 3.2$
Calorimeter 2nd layer	0.025×0.025	$\|\eta\| < 1.40$	0.050×0.025	$1.375 < \|\eta\| < 1.425$
	0.075×0.025	$1.40 < \|\eta\| < 1.475$	0.025×0.025	$1.425 < \|\eta\| < 2.5$
			0.1×0.1	$2.5 < \|\eta\| < 3.2$
Calorimeter 3rd layer	0.050×0.025	$\|\eta\| < 1.35$	0.050×0.025	$1.5 < \|\eta\| < 2.5$
Number of readout channels				
Presampler	7808		1536 (both sides)	
Calorimeter	101760		62208 (both sides)	
LAr hadronic end-cap				
$\|\eta\|$ coverage			$1.5 < \|\eta\| < 3.2$	
Number of layers			4	
Granularity $\Delta\eta \times \Delta\phi$			0.1×0.1	$1.5 < \|\eta\| < 2.5$
			0.2×0.2	$2.5 < \|\eta\| < 3.2$
Readout channels			5632 (both sides)	
LAr forward calorimeter				
$\|\eta\|$ coverage			$3.1 < \|\eta\| < 4.9$	
Number of layers			3	
Granularity $\Delta\eta \times \Delta\phi$			FCal1: 3.0×2.6	$3.15 < \|\eta\| < 4.30$
			FCal1: $\sim$ four times finer	$3.10 < \|\eta\| < 3.15$
			FCal1: $\sim$ four times finer	$4.30 < \|\eta\| < 4.83$
			FCal2: 3.3×4.2	$3.24 < \|\eta\| < 4.50$
			FCal2: $\sim$ four times finer	$3.20 < \|\eta\| < 3.24$
			FCal2: $\sim$ four times finer	$4.50 < \|\eta\| < 4.81$
			FCal3: 5.4×4.7	$3.32 < \|\eta\| < 4.60$
			FCal3: $\sim$ four times finer	$3.29 < \|\eta\| < 3.32$
			FCal3: $\sim$ four times finer	$4.60 < \|\eta\| < 4.75$
Readout channels			3524 (both sides)	
Scintillator tile calorimeter				
	Barrel		Extended barrel	
$\|\eta\|$ coverage	$\|\eta\| < 1.0$		$0.8 < \|\eta\| < 1.7$	
Number of layers	3		3	
Granularity $\Delta\eta \times \Delta\phi$	0.1×0.1		0.1×0.1	
Last layer	0.2×0.1		0.2×0.1	
Readout channels	5760		4092 (both sides)	

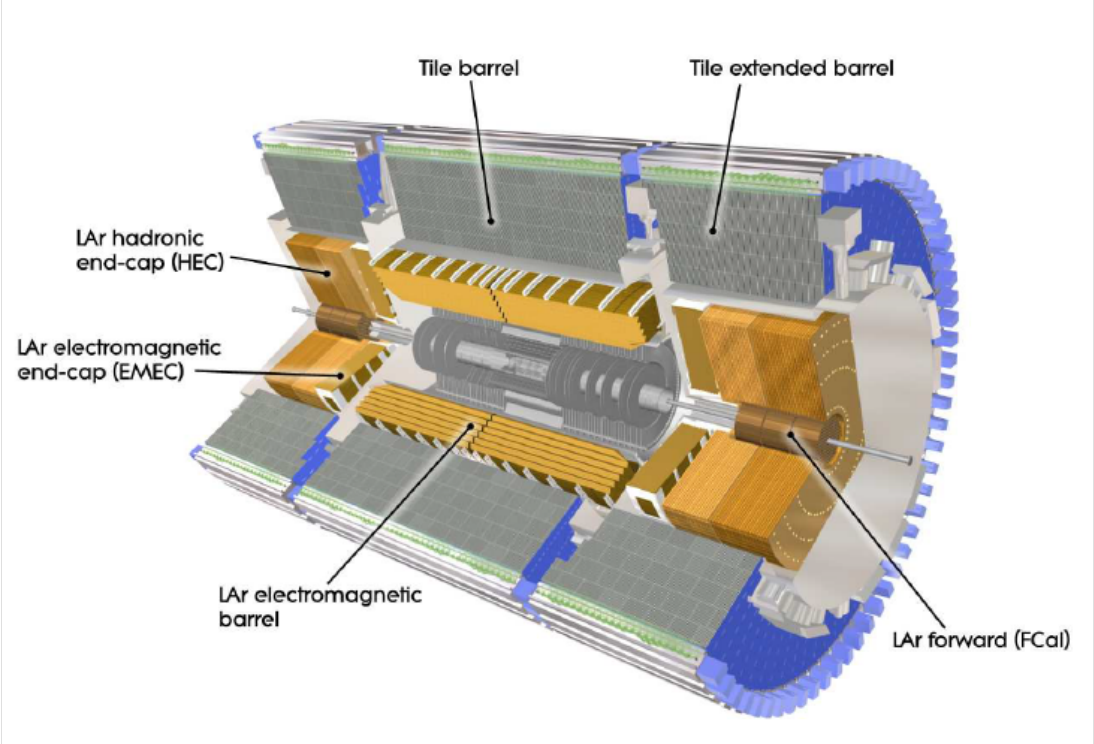

Figure 3.19: Cut-away view of the ATLAS calorimeter system [12]

of the EM calorimeter

$$\frac{\sigma_E}{E} = \frac{10\%}{\sqrt{E(GeV)}} \oplus 0.7\%. \tag{3.4}$$

The design goal for jets in combination with EM calorimeter is

$$\frac{\sigma_E}{E} = \frac{50\%}{\sqrt{E(GeV)}} \oplus 3\% \tag{3.5}$$

for $|\eta| < 3$ and

$$\frac{\sigma_E}{E} = \frac{100\%}{\sqrt{E(GeV)}} \oplus 5\%, \tag{3.6}$$

for $3 < |\eta| < 5$.

3.2.3.1 Electromagnetic Calorimetry

The high granularity liquid-argon (LAr) electromagnetic sampling calorimeters have excellent energy and position resolution. The pseudorapidity coverage is $|\eta| <$

3.2. The total thickness of the EM calorimeter, > 22 radiation length (X_0) in the barrel and > 24 X_0 in the endcaps, provides good containment of electromagnetic showers.

The EM calorimeter is made of sandwiches of lead absorbers and electrodes with LAr filling the gaps, as shown in Figure 3.20. The electric field is approximately 10 kV/cm. The drift of electrons liberated by ionization of charged particles from showers induces current in the electrodes. The readout segmentation is defined by the pattern on electrodes. The detector has an accordion geometry, which provides full ϕ coverage without azimuthal cracks by allowing the calorimeters to have several active layers in depth, three in the precision-measurement region ($0 < |\eta| < 2.5$) and two in the higher-η region ($2.5 < |\eta| < 3.2$) and in the overlap region between the barrel and the EMEC. In the precision-measurement region, an accurate position measurement is obtained by fine segmentation. Figure 3.21 shows a barrel module with an accordion design in three sampling layers. The dimensions of basic cells in each sampling are also shown. The segmentation in η and depth is achieved by etching cells on copper electrodes. The segmentation in ϕ is done by summing signals over electrodes: 16 in the first, 4 in the second and 4 in the third sampling. In the region of $|\eta| < 1.8$, a pre-sampler detector is used to correct for the energy lost by electrons and photons upstream of the calorimeter. The pre-sampler consists of an active LAr layer of thickness of 1.1 cm in the barrel and 0.5 cm in the endcap region.

3.2.3.2 Hadronic Calorimeters

The hadronic calorimetry in the range $|\eta| < 1.7$ is provided by a scintillator-tile calorimeter, which is separated into a large barrel and two smaller extended barrel cylinders, one on each side of the barrel. In the endcaps ($|\eta| > 1.5$), LAr technology is also used for the hadronic calorimeters, matching the outer $|\eta|$ limits of endcap electromagnetic calorimeters. The LAr forward calorimeters provide both electromag-

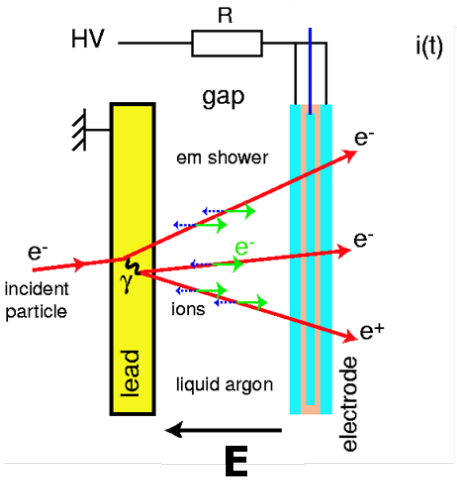

Figure 3.20: Drawing shows the structure of a basic LAr unit consisting of sandwich of absorber and electrodes [12]

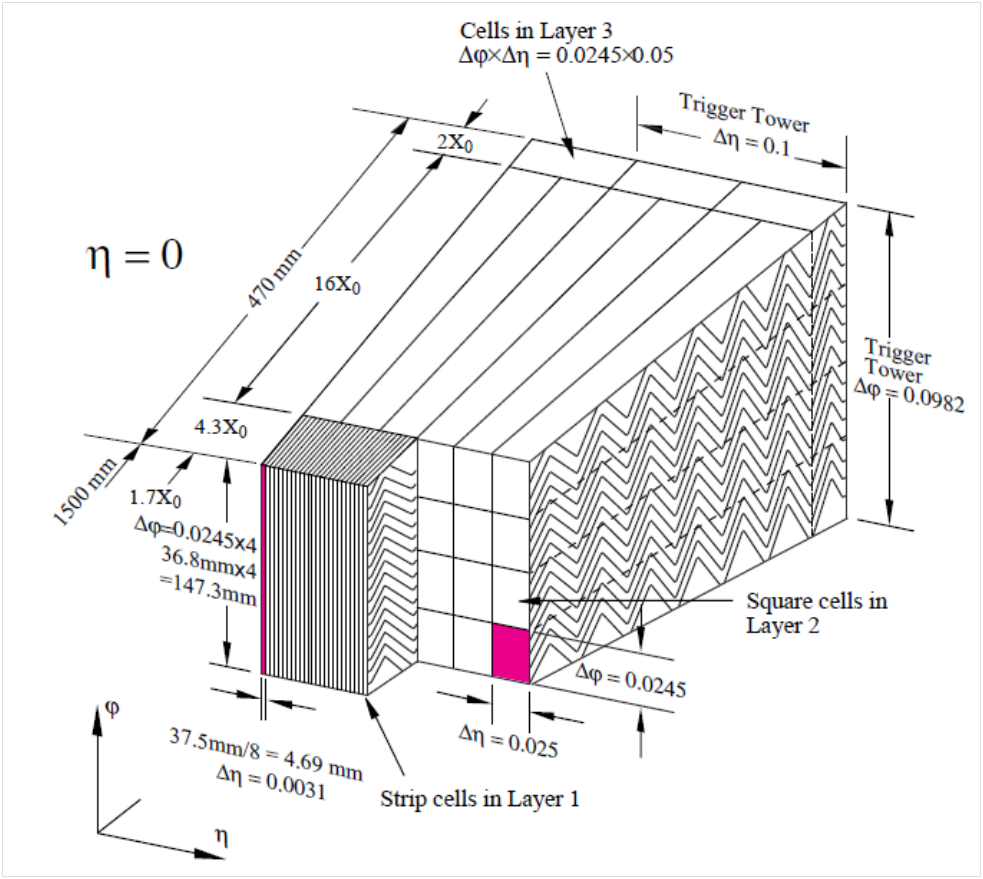

Figure 3.21: Sketch of a barrel module the granularity in η and ϕ of the cells of each of the three layers and of the trigger tower is also shown [12]

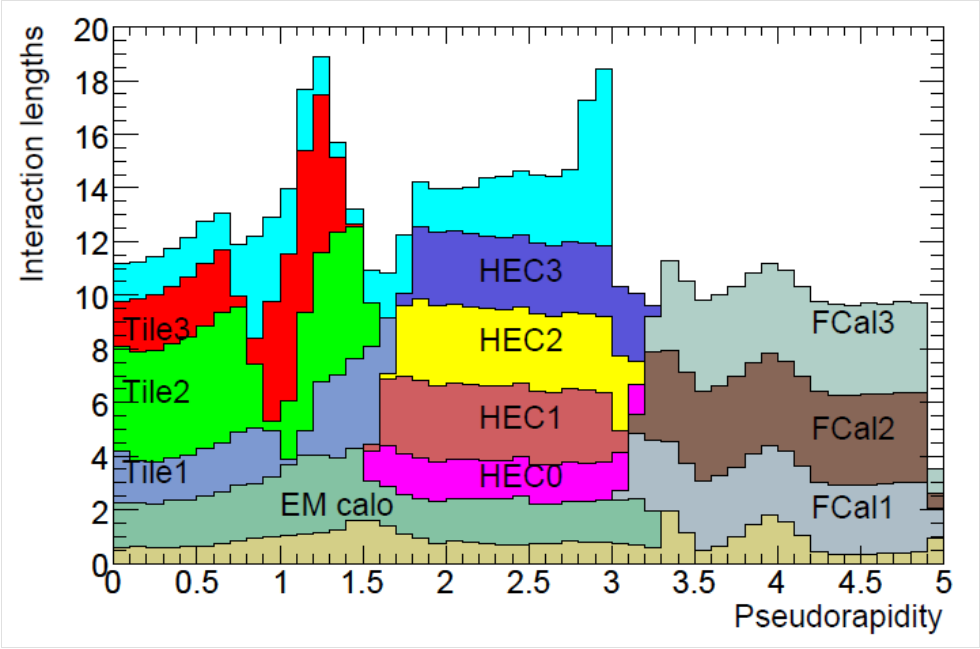

Figure 3.22: The cumulative amount of material in front of the muon spectrometer vs. pseudorapidity $|\eta|$, in units of interaction length [12]

netic and hadronic energy measurements, and extend the pseudorapidity coverage to $|\eta| = 4.9$. The approximate 9.7 interaction lengths (λ) of active calorimeter in the barrel and 10 λ in the endcaps are adequate to capture the hadronic showers and also provide good resolution for high-energy jets. The total thickness, including 1.3 λ from the outer support, is 11 λ at $\eta = 0$ and has been shown both by measurements and simulations to be sufficient to reduce punch-through into the muon system well below the irreducible level of prompt or decay muons. The cumulative amount of material in front of the muon spectrometer, in units of interaction length, is shown in Figure 3.22. Together with the large η-coverage, this thickness will also ensure a good missing transverse energy measurement.

The tile calorimeter is placed directly outside the EM calorimeter envelope with barrel coverage $|\eta| < 1.0$ plus coverage of $0.8 < |\eta| < 1.7$ by the two extended barrels. It uses steel as absorber and plastic scintillating tiles as the active material. The barrel and extended barrels are divided azimuthally into 64 modules. The LAr

hadronic endcap calorimeter is a copper/LAr sampling calorimeter with a flat-plate design consisting of two independent wheels per endcap, located directly behind the endcap EM calorimeter and sharing the same LAr cryostats. Each wheel is built from 32 identical wedge-shaped modules and divided into two segments in depth, for a total of four layers per endcap. The LAr forward calorimeter is integrated into the endcap cryostats, as this provides uniformity of the calorimetric coverage as well as reduced radiation background level in the muon spectrometer. The FCal consists of three modules in each endcap. The first module is made of copper optimized for electromagnetic measurements, while the other two, made of tungsten, measure predominantly the energy of hadronic interactions. Each module consists of a metal matrix, with regularly spaced longitudinal channels filled with electrode structures consisting of concentric rods and tubes parallel to the beam axis.

3.2.4 Inner Detector

The Inner Detector (ID) is the inner-most system of the ATLAS detector. It is designed to provide high-quality tracking for charged tracks above a p_T threshold of 0.5 GeV and within a pseudorapidity range $|\eta| < 2.5$ with excellent momentum resolution and precise vertex measurement. It also provides electron identification for p_T ranging between 0.5 GeV and 150 GeV and $|\eta| < 2.0$. The ID is immersed in a 2 T solenoidal field. Pattern recognition, momentum and vertex measurements and electron identification are achieved with a combination of discrete, high resolution semiconductor pixel and strip detectors, named as Pixel Detector and Semi-conductor Tracker (SCT), in the inner part of the tracking volume. Straw-tube tracking detectors – Transition Radiation Detector (TRT) with the capability to generate and detect transition radiation fill the outer part. The pixel detector and SCT uses semi-conductor technology while the TRT is a gas detector. The layout of the inner detector is shown in Figure 3.23. Each sub-detector has a cylindrical central barrel

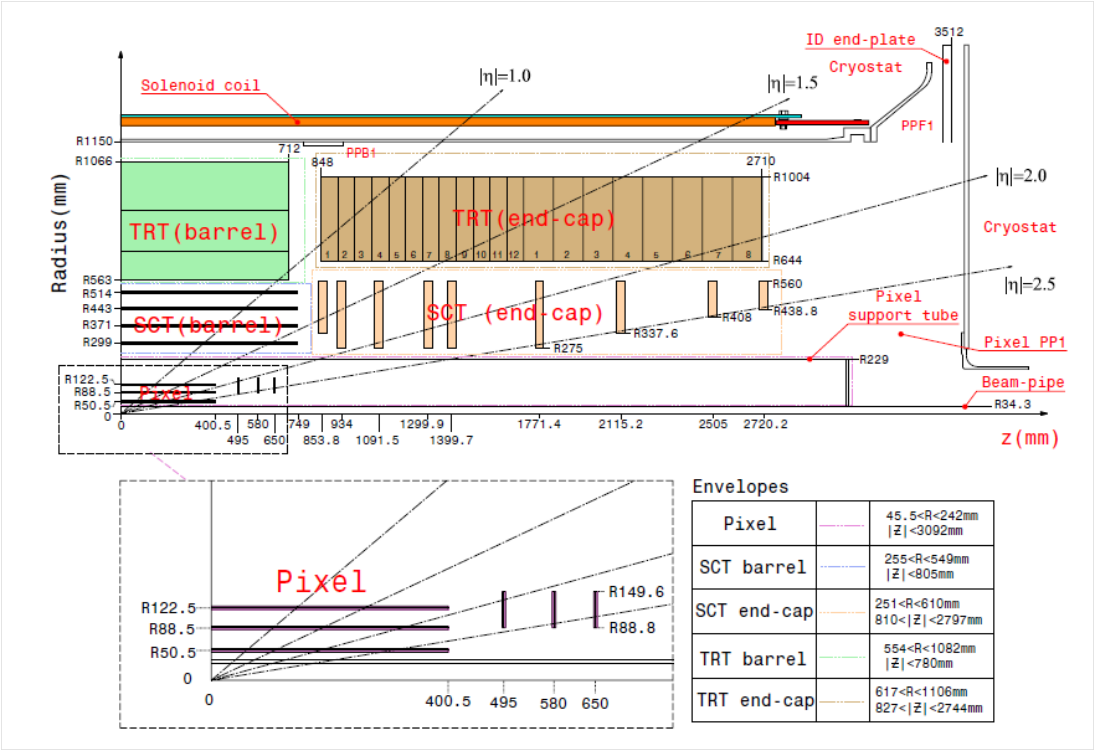

Figure 3.23: Plan view of a quarter-section of the inner detector showing each of the major detector elements with its active dimensions and envelopes [12]

and endcap disks or wheels. Figure 3.24 and 3.25 show the sensors and structural elements traversed by 10 GeV tracks in the barrel and endcap, respectively.

3.2.4.1 Pixel Detector

The Pixel Detector consists of three barrel layers at $R = 5.1, 8.9, 12.3\ cm$ and three disks of endcap pixel detectors on each side of the central barrel with $R_{in} = 9\ cm$ and $R_{out} = 15\ cm$. The barrel covers pseudorapidity range up to 1.9, coverage from 1.9 to 2.5 is achieved by both barrel and endcap detectors. There are 1744 modules of sensor and active electronics in the Pixel Detector, adding up to a total area of 1.8 m^2 . The barrel modules are mounted with a 20 degree angle so that a typical track passes through 2 to 3 pixels. Each module has 46080 channels and is 250 μm thick. The basic pixel unit measures $50 \times 400\ \mu m$. The partially depleted configuration allows operation after significant radiation dose. A 2×8 array of front-end readout

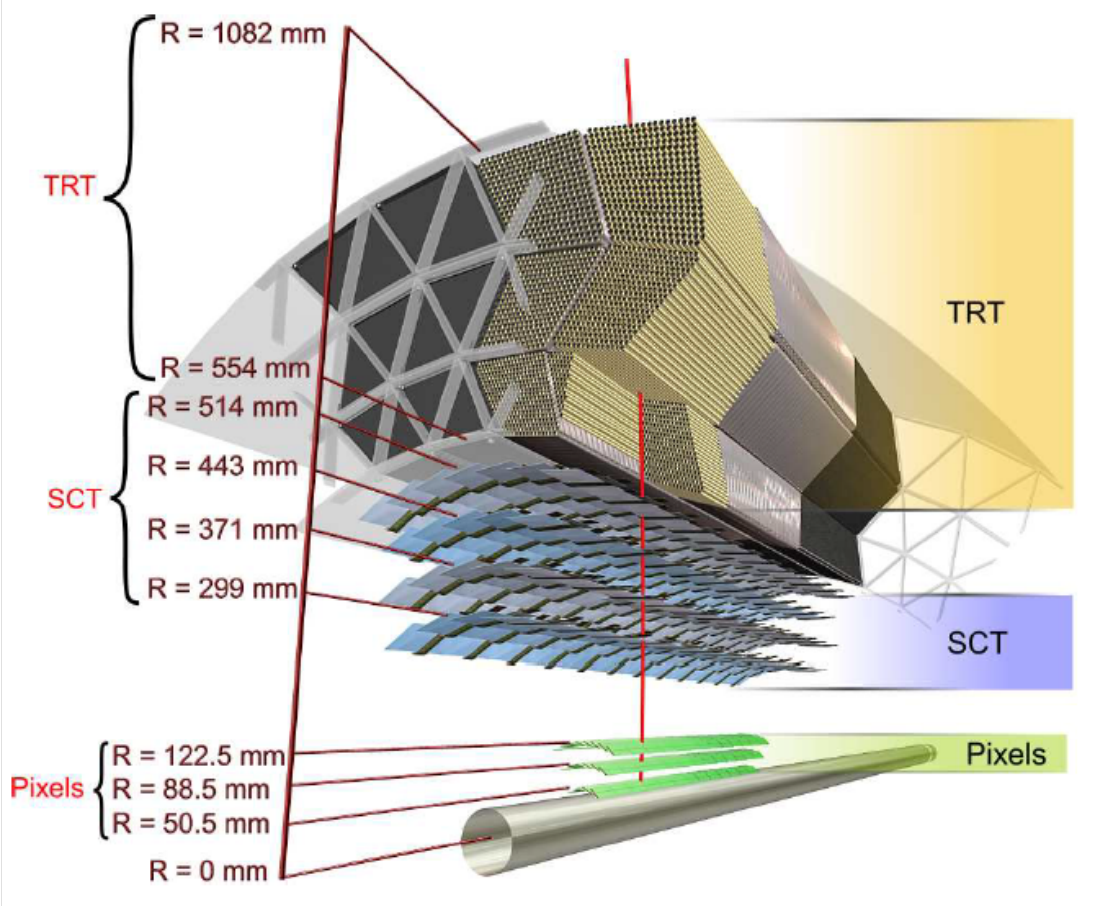

Figure 3.24: Drawing showing the sensors and structural elements traversed by a charged track with p_T of 10 GeV in the barrel inner detector ($\eta = 0.3$) [12]

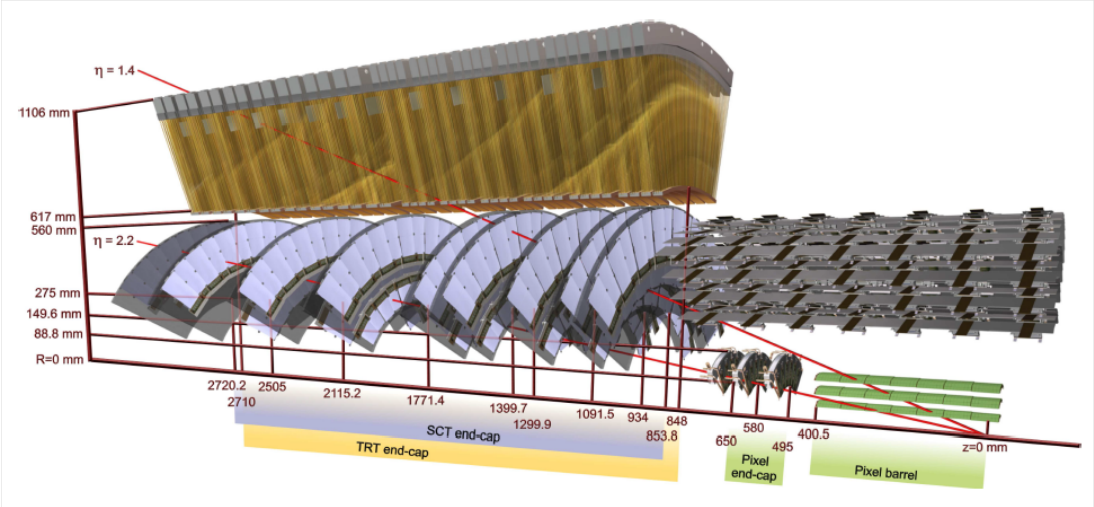

Figure 3.25: Drawing showing the sensors and structural elements traversed by two charged tracks with p_T of 10 GeV in the end-cap inner detector ($\eta = 1.4$ *and* 2.2) [12]

chips (FE-I) bump are bonded directly to sensors. Each module has a dedicated chip which controls loading of configuration of FE chip parameters, distributes clocks, timing information and etc. This control chip collects data from all 16 front end chips, formats, builds and serializes events, and optically outputs data. The Pixel Detector has very low noise ($> 200\ e^-$, while the hit threshold is 4000), very high efficiency ($> 99\%$) and excellent resolution of around 7.5 μm.

3.2.4.2 Semi-conductor Tracker

The Semi-conductor Tracker has four barrel cylinders of 1.5 meters long at $R = 30, 37, 44$ *and* 51 cm and nice endcap disks on each side with $R_{min} = 27\ cm$ and $R_{out} = 56\ cm$. The barrel covers the pseudorapidity range up to 1.2, the range between 1.2 and 1.6 is covered by barrel and endcap together and from 1.6 to 2.5 is covered by endcap only. It is made of 4088 modules and 6.2 million channels corresponding to an area of 63 m^2. The 2112 barrel modules are tilted at 11 degrees. There are 15912 single-sided silicon strip sensors in SCT, each consisting 768 active strips. The barrel SCT modules use 80 μm pitch micro-strip sensors, while the endcap modules use

radial strip pattern with $57 - 94\ \mu m$ pitch strips. The sensors are 285 μm thick and 6 cm long. Usually, two sensors are wire-bonded to make a 12 cm long unit. Within a barrel module, four sensors are glued back to back on a 380 μm thick baseboard with two on each side. The sensors are angled at $\pm 20\ mrad$ for stereo hit imaging. There are six front end chips on each side of a module. The SCT has very good noise performance with $< 5 \times 10^{-4}$ noise occupancy and is over 99% efficient. The resolution of SCT is 17 μm.

3.2.4.3 Transition Radiation Tracker

The Transition Radiation Tracker serves as the outer tracking chamber and also aids in electron identification. The barrel covers a pseudorapidity range up to 0.6, between 0.6 and 1.1 is covered by both barrel and endcap, from 1.1 to 2.1 is covered by endcap only. Unlike the Pixel Detector and SCT which run at a temperature of $-10°$ to $-5°$ Celsius, the TRT runs at room temperature. The basic unit is 4 mm diameter straw tube. The barrel consists of 52544 straws of 1.4 m long at $56.3\ cm < R < 106.6\ cm$ and $|z| < 71.2\ cm$, while the endcap has 245760 straws of 37 cm long with $64.4\ cm < R < 100.4\ cm$ and $84.8\ cm < |z| < 271.0\ cm$. The straws are accompanied by a radiator material that induces transition radiation for high-γ particles. The straw tubes are made from 72 μm thick kapton with aluminum layer. The coaxial wire is 31 μm diameter gold-plated tungsten. The gas mixture is 70% Xe, 27% CO_2 and 3% O_2. The straw shell is held at $-1500\ V$ with typical gas gain of 2.5×10^4. The TRT is tuned to reach 2% noise occupancy. The typical efficiency is around 95% and the intrinsic straw resolution is $130 \mu m$.

3.3 Performance of The LHC and ATLAS in 2010

2010 marks an exciting year of the LHC running. Starting from March 31, LHC successfully delivered pp collisions for a total integrated luminosity of 48.1 pb^{-1} at

Parameter	Nominal	2010
Beam Energy ($\rightarrow \gamma_r$)	7 TeV	3.5 TeV
Squeeze (β^*)	0.55 m	3.5 m
Transverse Emittance (ϵ_n)	3.75 $\mu m \cdot rad$	$2-3$ $\mu m \cdot rad$
Protons per Bunch (N_b)	1.15×10^{11}	up to 1.2×10^{11}
Bunch Separation	25 ns	150 ns
Number of Bunches (n_b)	2808	368

Table 3.7: LHC machine parameters at the end of pp collisions in 2010. Please note that fills with bunch separations at 75 ns and 50 ns have also been successfully achieved but not for physics.

$\sqrt{s} = 7\ TeV$. All the expected physics signatures have been established. Heavy ion runs started on November 8, only four days after extracting the final proton beam. The total integrated luminosity of Pb-Pb collisions delivered by the LHC is 9.7 μb^{-1} at center-of-mass energy of 2.76 TeV in Fall 2010. Out of $\sim$ 6600 hours of LHC running, there are 1074 hours of stable beam with 147 fills (110 for pp and 37 for Pb-Pb). The maximum peak luminosity achieved during pp run is $\sim 2 \times 10^{32} s^{-1} cm^{-2}$, which is an increase of 5 orders of magnitude from the initial $\sim 10^{27} s^{-1} cm^{-2}$. The machine parameters (as in Equation 3.2) achieved at the end of the pp collisions are summarized in Table 3.7. The LHC operated slightly above design parameters in terms of transverse emittance and number of protons per bunch.

Figure 3.26 shows the integrated luminosity delivered by the LHC (green), and recorded by ATLAS (yellow) versus day during the 2010 pp collisions at $\sqrt{s} = 7\ TeV$. ATLAS recorded 45 pb^{-1} in 2010 pp collisions with an overall data taking efficiency of 93.6%. The integrated luminosity of Pb-Pb collisions recorded by ATLAS in 2010 is 9.2 μb^{-1} corresponding to an average data taking efficiency of 94.6%.

The ATLAS detector had stable performance despite a dramatic increase in luminosity. Over 97% of channels of most sub-detectors were operational as shown in Table 3.8. 80%-85% of recorded luminosity were used for analysis.

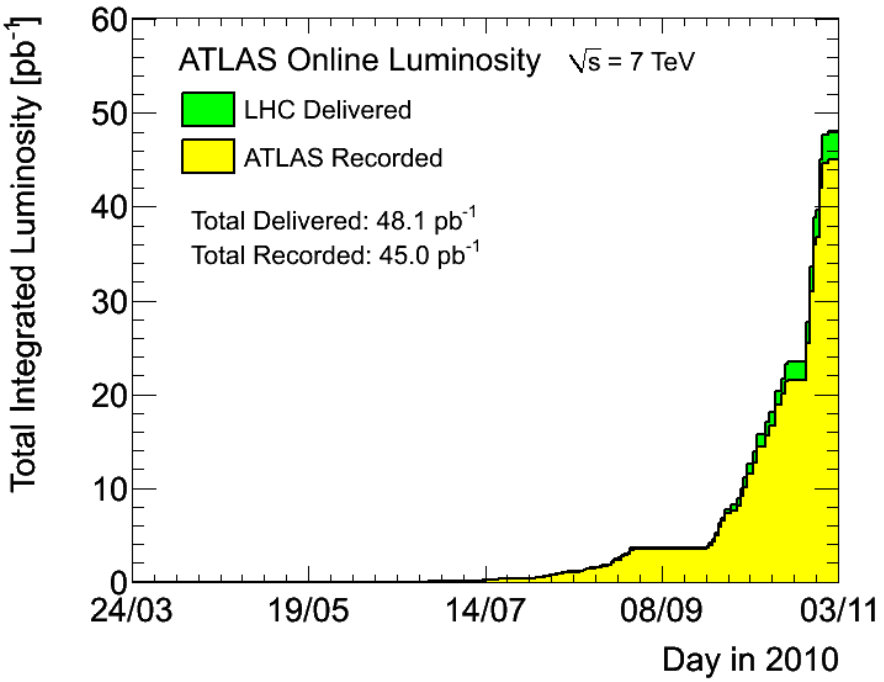

Figure 3.26: Online plot of the cumulative luminosity versus day LHC delivered to (green), and recorded by ATLAS (yellow) during stable beams and for pp collisions at 7 TeV center-of-mass energy [2].

Sub-detector	Component	Number of Channels	Operational Fraction
Inner Tracker	Pixel	80 M	99.0%
	SCT	6.3 M	99.9%
	TRT	350 k	100%
Calorimeters	LAr EM	170 k	90.5%
	LAr Hadronic	5600	96.6%
	LAr Forward	3500	97.8%
	Tile	9800	94.3%
Muon Spectrometer	MDT	350 k	99.9%
	CSC	31 k	96.2%
	RPC	370 k	99.8%
	TGC	320 k	99.8%

Table 3.8: ATLAS detector status showing number of channels of each sub-detector and the approximate operational fraction.

CHAPTER IV

Data Samples

A description of collision data and Monte Carlo (MC) simulated samples used in this $W \to \mu\nu$ analysis are described in this chapter. The results of collision data are always shown along with comparison to that of MC.

4.1 Data Samples and Luminosity

The data used in this thesis were collected by the ATLAS experiment from March 30 to October 31, 2010 and correspond to an integrated luminosity of $35.2 \pm 1.2\ pb^{-1}$ in proton-proton collision at a center of mass energy of 7 TeV. Data for the analysis are from the muon stream *MuonswBeam* for Run Period A-D (Run Number 152166-159224) and *Muons* for Run Period E-I (160387-167844). Both streams are inclusive express data dedicated for physics analysis selected by single muon triggers (Section 5.6).

The total integrated luminosity is determined by standard ATLAS tools from the *Good Run List* (GRL) [4] which is based on data quality flags in different run periods. Table 4.1 lists the triggers applied in the analysis for different run periods and the corresponding integrated luminosities. The uncertainty of the integrated luminosity obtained from van der Meer scans is ±3.4% [10] and is dominated by current knowledge of beam currents.

Run Period	L1_ MU10 $\int Ldt\ (pb^{-1})$	EF_ mu10_ MG $\int Ldt\ (pb^{-1})$	EF_ mu13_ MG $\int Ldt\ (pb^{-1})$	EF_ mu13_ MG_ tight $\int Ldt\ (pb^{-1})$
A - E3	0.776			
E4 - G1		3.02		
G2 - I1 (167576)			15.83	
I1 (167607) - I2				15.57
Total (A-I2)	35.2 pb^{-1}			

Table 4.1: Integrated luminosities for different run periods and different triggers used in the analysis.

The data format called D3PD used in this analysis is a flat ntuple from *Derived Physics Data* (DPD). These datasets are developed by the Michigan ATLAS group for the *Standard Model ElectroWeak working group* (SMEW) at ATLAS. SMEW DP3Ds are converted from *Analysis Object Data* (AOD) with a pre-filter that requires at least one muon or electron candidate with $p_T > 10\ GeV$. The AODs (nominal size of 100 KB/event) are produced from *Event Summary Data* (ESD) (size of 500 KB/event) with sufficient information for common analyses. The ESDs contain the detailed output of the detector reconstruction and are produced from the raw data. The ATLAS central production produced these datasets using ATHENA software framework v15.6.13.2.

4.2 Monte-Carlo Samples

In order to compare the data with theoretical expectations and to estimate the backgrounds from various physics processes, Monte-Carlo simulations were performed. Dedicated $W \to \mu\nu$ samples were generated as the signal process. The leptonic decay of a tau lepton $\tau \to \mu\nu$ in the $W \to \tau\nu$ process is also treated as signal because the experimental signature of this process is identical to that of $W \to \mu\nu$. For the backgrounds the following processes were considered:

- $Z \to \mu\mu$: this process is considered an important background when one muon is outside the muon-spectrometer coverage and generates apparent missing transverse energy.

- $Z \to \tau\tau$: this process has a small contribution via leptonic tau decay.
- $t\bar{t}$ and single top: W production from top introduces an additional background.
- Drell-Yan: these processes contribute to background through the same physics processes as $Z \to \mu\mu$ and $Z \to \tau\tau$.
- QCD di-jet: $b\bar{b}$ and $c\bar{c}$ are significant components because of semi-leptonic decays of heavy quarks and misidentified jets as muons.

The production of W and Z boson and the Drell-Yan processes are modeled by PYTHIA [46], a *leading-order* (LO) Monte Carlo generator. The top events are modeled by MC@NLO [36], which is a *next-to-leading-order* (NLO) MC generator incorporating the NLO matrix elements into the parton shower. Events with heavy flavor di-jets are modeled with PYTHIAB. To be consistent with the data, the MC datasets used in this analysis are also produced by the ATLAS central production using ATHENA software framework v15.6.13.2.

Table 4.2 includes relevant information for all the MC processes: cross-section, k-factor, filter efficiency, number of events and the generator used for the simulation. The cross sections quoted in this table, corrected by k-factors and filter efficiency ε_{filter}, are used to normalize predicted event counts for the corresponding MC samples. The k-factor, a correction for higher-order QCD calculation, is defined as the cross section ratio, $d\sigma(NLO)/d\sigma(LO)$. So processes generated by LO event generators have k-factors larger than 1. The filter efficiency ε_{filter} is less than 1 if a pre-filter is applied when generating this MC process. N_{MC} is the total number of events generated.

During the data-taking period, as the instantaneous luminosity increased from the initial 10^{27} to 2.1×10^{32} $cm^{-2}s^{-1}$, the number of interactions in each event increased from 1 to about 3.7. This is called the *pile-up*. Pile-up produces more tracks and more energy deposition in the calorimeter, thus affecting event selection. In this analysis, pile-up affects the muon identification and measurement of the missing transverse

Process	cross-section (pb)	k-factor	ε_{filter}	N_{MC}	Generator
$W \to \mu\nu$	8.89406E+3	1.17	1.0	6992799	Pythia
$W \to \tau\nu$	8.824E+3	1.17	1.0	1998801	Pythia
$Z \to \mu\mu$	8.51011E+2	1.15	1.0	4998410	Pythia
$Z \to \tau\tau$	8.56967E+2	1.15	1.0	1998598	Pythia
$t\bar{t}$	1.6457E+2	1.0	0.5562	773167	MC@NLO
st_tchan$\to e\nu$	7.1522E+0	1.0	1.0	5945	MC@NLO
st_tchan$\to \mu\nu$	7.1767E+0	1.0	1.0	5983	MC@NLO
st_tchan$\to \tau\nu$	7.1277E+0	1.0	1.0	5928	MC@NLO
st_schan$\to e\nu$	4.6856E-1	1.0	1.0	8424	MC@NLO
st_schan$\to \mu\nu$	4.6837E-1	1.0	1.0	8432	MC@NLO
st_schan$\to \tau\nu$	4.6978E-1	1.0	1.0	8480	MC@NLO
Wt	1.4581E+1	1.0	1.0	13277	MC@NLO
Drell-Yan$\to \mu\mu$	1.2529E+3	1.167	1.0	999503	Pythia
Drell-Yan$\to \tau\tau$	3.4540E+0	1.15	1.0	99984	Pythia
ccmu4X	2.84E+4	1.0	0.9	1499257	PythiaB
bbmu4X	7.39E+4	1.0	0.9	4443898	PythiaB

Table 4.2: The cross-section, k-factor, generator level filter efficiency, total number of events and generator name for the MC processes used in this analysis. st_Xchan (X=t, s) are single top processes in t or s channel. ccmu4X/bbmu4X are di-jet processes with muon (transverse momentum larger than 4 GeV) in the final states. The names of the other MC processes are selfexplanatory.

energy and the transverse mass of the muon plus neutrino system. To account for this effect, the MC samples were simulated with pile-up with an average of two primary vertices and then weighted to the primary vertex multiplicity distribution observed in the data.

CHAPTER V

Object Reconstruction and Identification

This chapter describes the reconstruction and identification of relevant objects in $W \to \mu\nu$ analysis. Muons are reconstructed and identified using a variety of strategies combining information collected by the muon spectrometer, inner detector and calorimeters. These algorithms will be briefly described in Section 5.1. Muon performance in terms of identification efficiency and momentum resolution are studied with data-driven methods documented in Section 5.2 and Section 5.3. Neutrinos escape from the detectors. Measurement of neutrinos are inferred from an imbalance of the transverse energy, namely the missing transverse energy described in Section 5.4. Section 5.5 summarizes the jet finding algorithm employed in this thesis when the W^+/W^- ratio depends on the number of jets in the event. Finally, a description of the ATLAS trigger system and study on trigger efficiency are presented in Section 5.6.

5.1 Muon Reconstruction

The ATLAS detector has been designed to provide clean and efficient muon identification and precise momentum measurement. The muon spectrometer is the primary detector system to achieve this goal. However, the reconstruction of muons also incorporates information from the inner detector and the calorimeters. The inner detector provides precision tracking information within pseudorapidity coverage of $|\eta| < 2.5$.

Over most of the acceptance, for p_T roughly in the range between 30 and 200 GeV, the momentum measurements from the inner detector and muon spectrometer may be combined to give a precision better than either alone. The muon spectrometer dominates in the region above this range, while the inner detector dominates below it. Energy measurements in the calorimeter can aid in muon identification because of their minimum ionizing signature and can provide a useful direct measurement of the energy loss.

The goal of the muon reconstruction is to identify muons and measure their properties with high precision. Tracks are defined in terms of five parameters at the perigee, which is defined as the point of closest approach of the track to the z-axis. The five parameters are the transverse impact parameter d_0, longitudinal impact parameter z_0, the polar angle θ_0, the azimuthal angle ϕ_0, and the inverse momentum signed by the charge of the track q/p. There are two sets of muon reconstruction algorithms in ATLAS, Staco and MuID. Both algorithm sets will be discussed in this chapter. In this thesis results with muon reconstructed using the Staco algorithm are presented, while MuID is used for validation purpose.

5.1.1 Standalone Muons

The standalone algorithms utilize information provided by the muon spectrometer only. They first build track segments in each of the three muon stations and then link the segments to form tracks. The Staco algorithm that finds the spectrometer tracks and extrapolates them to the beam line is called Muonboy, while the Muid algorithm uses Moore to find MS tracks and then perform the inward extrapolation. The energy loss and multiple scattering in the calorimeters are account for during the extrapolation process.

Standalone algorithms have slightly greater $|\eta|$ coverage, up to 2.7 compared for 2.5 for the inner detector, but there are holes at $|\eta|$ near 0 and 1.2. Muons with very

low momentum (around a few GeV) may be difficult to reconstruct because they do not penetrate to the outer-most stations. The standalone algorithm may also find 'fake' muons from pion and kaon decays in the calorimeter.

5.1.2 Tagged Muons

The spectrometer tagging algorithms, MuTag and MuGirl, propagate all inner detector tracks with sufficient momentum out to the first station of the muon spectrometer and search for nearby segments. MuTag defines a tag chi-square using the difference between any nearby segment and its prediction from the extrapolated track. MuGirl uses an artificial neural network to define a discriminant. In both cases, if a segment is sufficiently close to the predicted track position, the inner detector track is tagged as corresponding to a muon. This approach is especially powerful for low p_T muons, which do not form complete tracks in the muon spectrometer, and for regions in the muon spectrometer with insufficient detector layers on the passage of the muon. The most important difference between these algorithms is that MuGirl considers all inner-detector tracks and redoes segment finding in the region around the track while MuTag only makes uses of inner detector tracks and muon spectrometer segments not used by Staco. Thus Mutag serves as a compliment to Staco. MuGirl is recorded in MuID family.

5.1.3 Combined Muons

Combined muon algorithms incorporate tracking in both the muon spectrometer and the inner detector. The match chi-square is defined as the difference between outer and inner track vectors weighted by their combined covariance error matrix.

$$\chi^2_{match} = (\mathbf{T_{MS}} - \mathbf{T_{ID}})^{\mathbf{T}}(\mathbf{C_{MS}} + \mathbf{C_{ID}})^{-\mathbf{1}}(\mathbf{T_{MS}} - \mathbf{T_{ID}}) \tag{5.1}$$

Where $\mathbf{T}$ denotes a vector of five track parameters, expressed at the point of closest approach to the beam line. $\mathbf{C}$ is its covariance matrix. The subscript MS refers to the muon spectrometer and ID is the inner detector. The chi-square is an important measure of the quality of the match. It is used to decided which combined tracks are retained.

Staco does a statistical combination of the inner and outer track vectors to obtain the combined track vector:

$$\mathbf{T} = (\mathbf{C_{MS}^{-1}} + \mathbf{C_{ID}^{-1}})^{-1}(\mathbf{C_{MS}^{-1}}\mathbf{T_{MS}} + \mathbf{C_{ID}^{-1}}\mathbf{T_{ID}}) \tag{5.2}$$

Muid does a partial refit by starting from the inner track vector and covariance matrix and adding the measurements from the outer track, instead of using the measurements of the inner track directly. The fit also accounts for multiple scattering and energy loss in the calorimeters, as well as magnetic field in the muon spectrometer.

Shown in Figure 5.1 is the di-muon invariant mass spectrum for ATLAS first year data corresponding to a integrated luminosity of 40 pb^{-1}, from opposite-sign combined muons in EF_MU15 triggered events. The agreement between data and Monte-Carlo demonstrates excellent muon reconstruction performance of the ATLAS detector.

5.2 Muon Identification and Efficiencies

The muon identification efficiencies are determined using the *tag-and-probe* method on $Z \to \mu\mu$ events from the data. The following three efficiencies are considered:

1. Muon *Muon Spectrometer* (MS) efficiency (ϵ_{CB}): the probability for an isolated ID muon to match with a muon identified as a *combined* (CB) muon;

2. Muon *Inner Detector* (ID) efficiency (ϵ_{ID}): the probability for an MS muon to match with a CB muon;

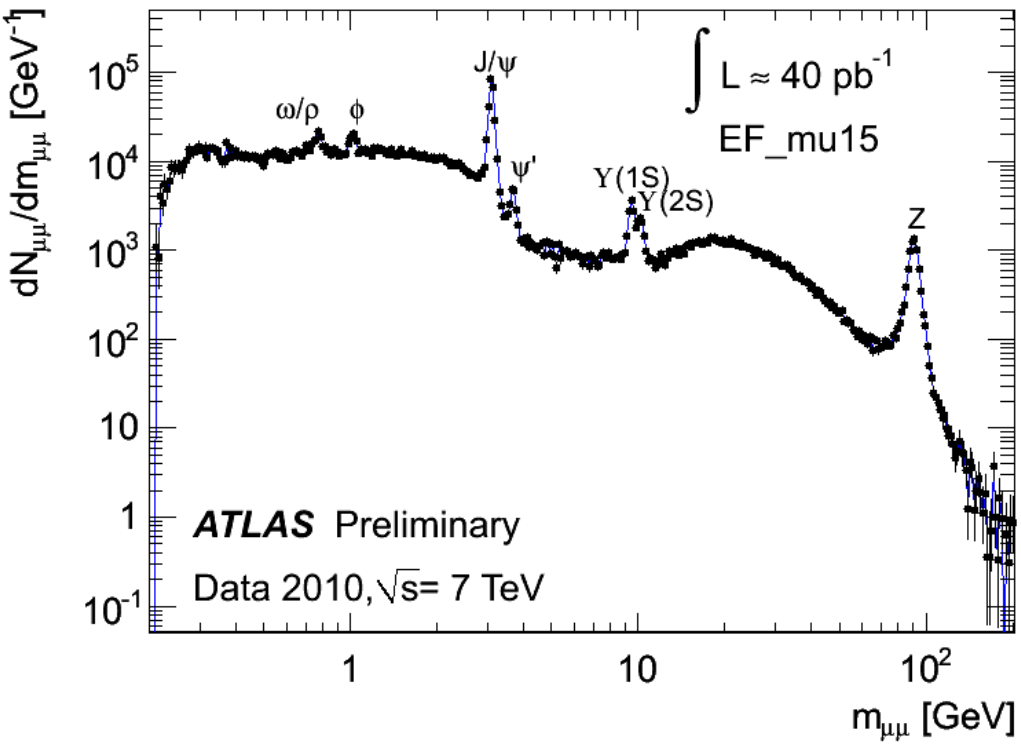

Figure 5.1: The invariant mass spectrum of $\mu^+\mu^-$ with 2010 collision data of 40 pb^{-1} using combined muons triggered by EF_MU15 at p_T threshold at 15 GeV. The plot labels all the known particles decaying to $\mu^+\mu^-$ [3].

3. Muon isolation efficiency (ϵ_{iso}): the probability for a CB muon to pass the isolation requirement.

The plots in Figure 5.2 illustrate how these efficiencies are determined.

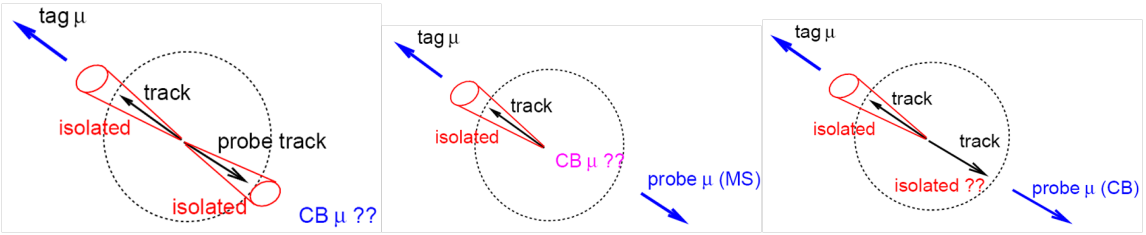

Figure 5.2: Illustration of the definitions for muon MS efficiency (left), ID efficiency (middle) and isolation efficiency (right).

The results are then compared with the efficiencies from the simulated $Z \to \mu\mu$ events with pile-up. Only statistical uncertainties are shown on the comparison plots.

5.2.1 Muon Spectrometer Efficiency (ϵ_{MS})

For the muon MS efficiency measurement, the *tag* muon is defined as a combined muon that is isolated and passes all the muon selection requirements. The *probe* muon is an isolated ID track that combines with the *tag* muon to be consistent with a good Z boson. The muon MS efficiency ϵ_{MS} is calculated by taking the ratio of the *probe* muons matching with CB muons to the total number of *probe* muons.

The quality cuts for a *tag* muon are:

- reconstructed as a combined muon
- transverse momentum of the muon $p_T > 15$ GeV
- pseudorapidity of the muon within the range $|\eta| < 2.4$
- transverse impact parameter w.r.t. the primary vertex within the range $|\Delta d_0| < 10$ mm
- muon isolation: sum of track p_T in cone $\Delta R = 0.2$ weighted by p_T of the muon $ptcone20/p_T < 0.1$

The *probe* ID track is required to pass the following cuts:

- transverse momentum of the track $p_T > 20$ GeV
- pseudorapidity of the track within the range $|\eta| < 2.4$
- transverse impact parameter w.r.t. the primary vertex within the range $|\Delta d_0| < 10$ mm
- at least 6 TRT hits if pseudorapidity of the track is within the range $|\eta| < 1.9$
- track isolation: sum of track p_T in cone $\Delta R = 0.2$ weighted by p_T of the track $ptcone20/p_T < 0.1$

In addition, the following cuts are applied to the *probe* ID track in order to ensure it is the second muon from the Z:

- opposite charge to the *tag* muon
- the invariant mass of the *tag* muon and the *probe* track must be within the Z mass window $|M_{\mu+track} - M_Z| < 15$ GeV
- The azimuthal angle ϕ between the *tag muon* and the *probe* track must be back-to-back, $|\Delta\phi| > 2$
- transverse momentum of the *tag* muon and the *probe* track $P_T(\mu + track) < 65$ GeV
- The *tag* muon and the *probe* track must come from the same primary vertex with $|\Delta d_0(\mu, trk)| < 0.1$ mm and $|\Delta z_0(\mu, trk)| < 2$ mm

For each *probe* track, all possible combined muons in the event are found. If a combined muon has transverse momentum $P_T > 10$ GeV, $|\eta| < 2.4$ and the distance between the *probe* track and the combined muon in $\eta - \phi$ space with $\Delta R < 0.01$, then the two objects are matched with each other. The muon MS efficiency as function of muon P_T, η and ϕ are shown in Fig. 5.3. The matching efficiency is found to be $(93.2 \pm 0.18)\%$ in data and $(94.9 \pm 0.05)\%$ in MC.

To estimate the systematic uncertainties, different isolation definitions of the *probe* track are used and the isolation cut values are varied. As shown in Table 5.1 the measured data efficiency varies by 0.4%. The background fraction is also examined using MC simulated data. The amount of background is estimated to be 0.4% from W+jets, 0.5% from QCD di-jet, 0.1% from $t\bar{t}$ and 0.3% from $W \to \mu\nu$ events. This

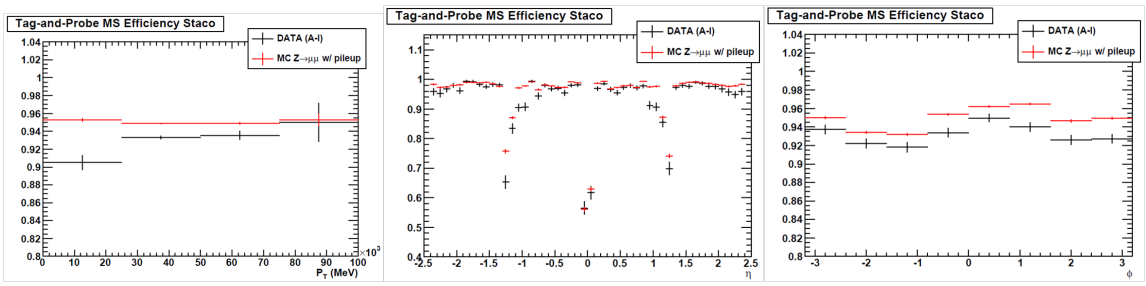

Figure 5.3: The muon MS efficiency as function of muon transverse momentum p_T (left), pseudorapidity η (middle) and azimuthal angle ϕ (right). Black is for data and red is for MC.

has a negligible effect on the efficiency measurement. The efficiency is observed to vary by 0.6% for different run periods, as shown in Figure 5.4. The final data/MC scale factor for the muon MS efficiency is estimated to be $0.982 \pm 0.002(stat) \pm 0.007(syst)$.

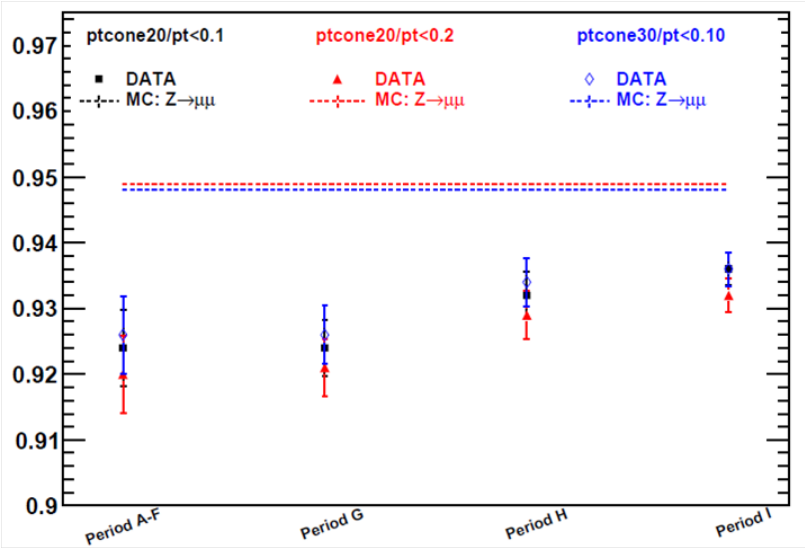

Figure 5.4: The muon MS efficiency for different run periods. Solid lines represent data and dashed lines represent MC. Black, red and blue is for isolation cut $ptcone20/p_T < 0.1$, $ptcone20/p_T < 0.2$ and $ptcone30/p_T < 0.1$ respectively.

Cone size	Isolation cut	ϵ_{MS} (Data)	ϵ_{MS} (MC)	Data/MC SF
0.2	0.05	$(93.3 \pm 0.18)\%$	$(94.9 \pm 0.05)\%$	98.3%
0.2	0.10	$(93.2 \pm 0.18)\%$	$(94.9 \pm 0.05)\%$	98.2%
0.2	0.15	$(93.0 \pm 0.18)\%$	$(94.9 \pm 0.05)\%$	98.0%
0.2	0.20	$(92.8 \pm 0.18)\%$	$(94.9 \pm 0.05)\%$	97.8%
0.3	0.05	$(93.3 \pm 0.19)\%$	$(94.8 \pm 0.05)\%$	98.4%
0.3	0.10	$(93.3 \pm 0.18)\%$	$(94.8 \pm 0.05)\%$	98.4%
0.3	0.15	$(93.2 \pm 0.18)\%$	$(94.9 \pm 0.05)\%$	98.2%
0.3	0.20	$(93.0 \pm 0.18)\%$	$(94.9 \pm 0.05)\%$	98.0%
0.4	0.05	$(93.5 \pm 0.21)\%$	$(94.8 \pm 0.05)\%$	98.6%
0.4	0.10	$(93.5 \pm 0.18)\%$	$(94.8 \pm 0.05)\%$	98.6%
0.4	0.15	$(93.4 \pm 0.18)\%$	$(94.8 \pm 0.05)\%$	98.5%
0.4	0.20	$(93.4 \pm 0.18)\%$	$(94.9 \pm 0.05)\%$	98.3%

Table 5.1: ϵ_{MS} and data/MC scale factor measured for different isolation cone sizes and isolation cut values applied to the probe track. The isolation cut with cone size of 0.2 and cut value at 0.10 is the standard isolation cut used in this analysis.

5.2.2 Muon Inner Detector Efficiency (ϵ_{ID})

For the muon ID efficiency measurement, the *tag* muon has the same definition and same quality requirements as the *tag* muon used for muon MS efficiency measurement. The *probe* muon is an MS track that combines with the *tag* muon to be consistent with a good Z boson. The muon ID efficiency ϵ_{ID} is calculated by taking the ratio of the *probe* muons matching with ID tracks to the total number of *probe* muons.

The quality cuts for the *probe* MS track are:

- transverse momentum measured by muon spectrometer with correction for energy loss in the calorimeter $p_T(MS) > 10$ GeV
- pseudorapidity measured by muon spectrometer within the range $|\eta(MS)| < 2.4$
- muon isolation: sum of track p_T in cone $\Delta R = 0.2$ weighted by p_T of the muon $ptcone20/p_T < 0.1$

The following list are the requirements of kinematics with respect to the *tag* muon applied to the *probe* MS track.

- opposite charge to the *tag* muon

- the invariant mass of the *tag* muon and the *probe* MS track must be within the Z mass window $|M_{\mu+track} - M_Z| < 15$ GeV
- The azimuthal angle ϕ between the *tag* muon and the *probe* track must be back-to-back, $|\Delta\phi| > 2$

In the next step, the *probe* MS track with a matching ID track is simply determined by it being a combined muon. The muon ID efficiency as function of muon p_T, η and ϕ are shown in Fig. 5.5. The matching efficiency is found to be $(99.8 \pm 0.03)\%$ in data and $(99.8 \pm 0.01)\%$ in MC.

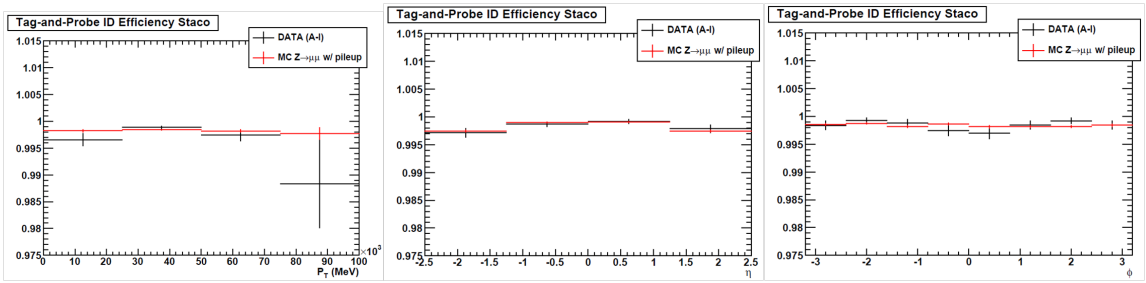

Figure 5.5: The muon ID efficiency as function of muon transverse momentum p_T (left), pseudorapidity η (middle) and azimuthal angle ϕ (right). Black is for data and red is for MC.

This measurement is repeated using different definition of muon isolation and cut values. The ID efficiency is found to be insensitive to the change in muon isolation requirement. Figure 5.6 shows the efficiency for different run periods. The background fractions are estimated using MC simulated events. The background contamination is 0.009% from W+jets, 0.245% from QCD di-jet, 0.07% from $t\bar{t}$ and 0.003% from $W \to \mu\nu$ events. These backgrounds have negligible effects on the efficiency measurement. The data/MC scale factor is $0.999 \pm 0.000(stat) \pm 0.001(syst)$.

5.2.3 Muon Isolation Efficiency (ϵ_{iso})

The *tag* muon in the muon isolation efficiency measurement is subject to the same requirements as in ϵ_{MS} and ϵ_{ID} measurements. The *probe* muon is a combined muon

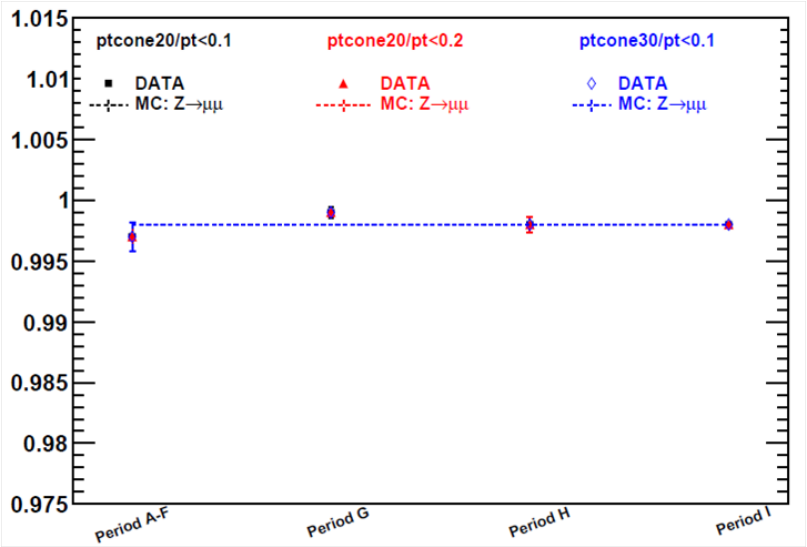

Figure 5.6: The muon ID efficiency for different run periods. Solid lines represent data and dashed lines represent MC. Black, red and blue is for isolation cut $ptcone20/p_T < 0.1$, $ptcone20/p_T < 0.2$ and $ptcone30/p_T < 0.1$ respectively.

without requiring isolation. The muon isolation efficiency ϵ_{iso} is defined as the number of isolated probe muons divided by the number of all the probe muons.

The cuts on the *probe* muon are:

- reconstructed as a combined muon
- transverse momentum of the muon $p_T > 15$ GeV
- pseudorapidity of the muon within the range $|\eta| < 2.4$
- transverse impact parameter w.r.t. the primary vertex within the range $|\Delta d_0| < 10$ mm
- muon isolation: sum of track p_T in cone ΔR=0.2 weighted by p_T of the muon $ptcone20/p_T < 0.1$

The additional cuts applied to the *probe* muon to make it consistent with a good muon from a Z are:

- opposite charge to the *tag* muon
- the invariant mass of the *tag* muon and the *probe* muon must be within the Z mass window $|M_{\mu\mu} - M_Z| < 15$ GeV
- The azimuthal angle ϕ between the two muons must be back-to-back, $|\Delta\phi| > 2$

- The two muons must come from the same primary vertex with $|\Delta d_0(\mu\mu)| < 0.2$ mm and $|\Delta z_0(\mu\mu)| < 2$ mm

The isolation requirement ptcone20/$p_T < 0.1$ is then added to the *probe* muon to determine the isolation efficiency. The muon isolation efficiency as function of muon p_T, η and ϕ are shown in Fig. 5.7. The isolation efficiency is found to be $(99.1 \pm 0.07)\%$ in data and $(99.3 \pm 0.02)\%$ in MC.

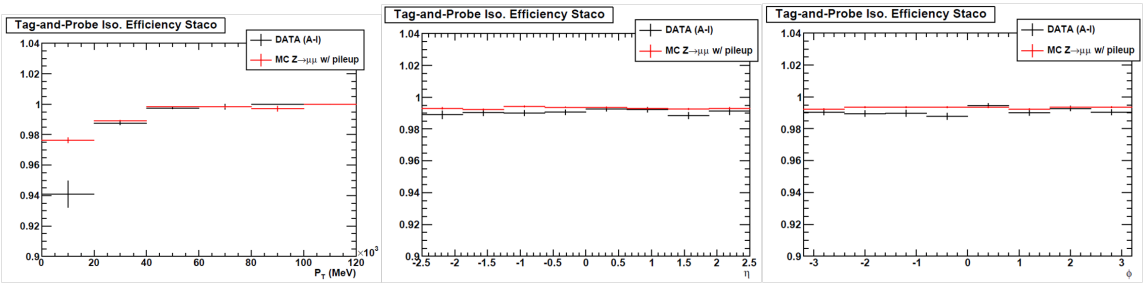

Figure 5.7: The muon isolation efficiency as function of muon transverse momentum p_T (left), pseudorapidity η (middle) and azimuthal angle ϕ (right). Black is for data and red is for MC.

Figure 5.8 shows the efficiency for different run periods. The efficiency varies by 0.2%. Using MC simulated events, the fraction of background contamination is estimated to be 0.04% from W+jets, 0.21% from QCD di-jet, 0.07% from $t\bar{t}$ and 0.04% from $W \to \mu\nu$ events. These backgrounds have negligible effects on the efficiency measurement. The data/MC scale factor is found to be $0.998 \pm 0.0007(stat) \pm 0.004(syst)$.

This study is also repeated with different muon isolation cuts in an effort to find the optimal muon isolation cut. $ptcone20/p_T < 0.1$ is found to be the best choice because it is less sensitive to pile-up with the small cone size and it yields a relatively high efficiency as well as a high data/MC scale factor while keeping the background at similar level. Therefore, this cut has been adopted throughout this analysis. Figure 5.9 shows how the isolation efficiency changes for different cone sizes and different cut values in all the run periods. Table 5.2 includes the efficiencies and the scale factors for different isolation cuts.

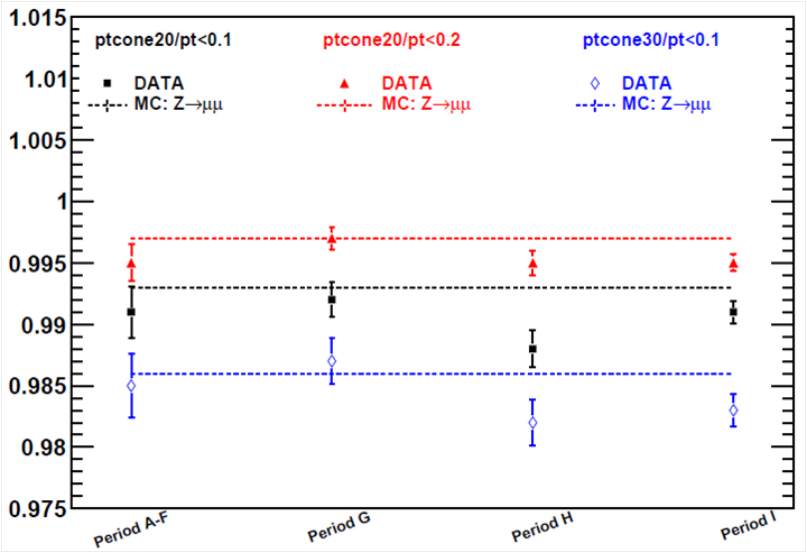

Figure 5.8: The muon isolation efficiency vs run periods. Solid lines represent data and dashed lines represent MC. Black, red and blue is for isolation cut $ptcone20/p_T < 0.1$, $ptcone20/p_T < 0.2$ and $ptcone30/p_T < 0.1$ respectively.

5.3 Muon Momentum Resolution and Scale

The dimuon mass spectrum from $Z \rightarrow \mu^+\mu^-$ process is used as the *standard candle* to check the muon momentum resolution and scale. From the early analysis on Z production in the muon decay channel, the muon momentum resolution in data was not well-reproduced in the MC simulation [33]. Additional muon momentum smearing in MC is necessary to reduce the uncertainties on detection efficiencies and background estimation. The momentum smearing formula used in this analysis is

$$(1/P_T)_{smear} = 1/C_1 \times (1/P_T)_{MC} \times (1 + x \times C_2) \tag{5.3}$$

where $(1/P_T)_{smear}$ is the smeared muon curvature and $(1/P_T)_{MC}$ is the muon curvature from the default MC simulation, C_1 is the momentum scale term and C_2 is the additional momentum smearing term, x is a random number generated with a Gaussian distribution with zero mean and unit width. The muon trajectory curvature is the smeared quantity due to the fact that the muon system measures this curvature

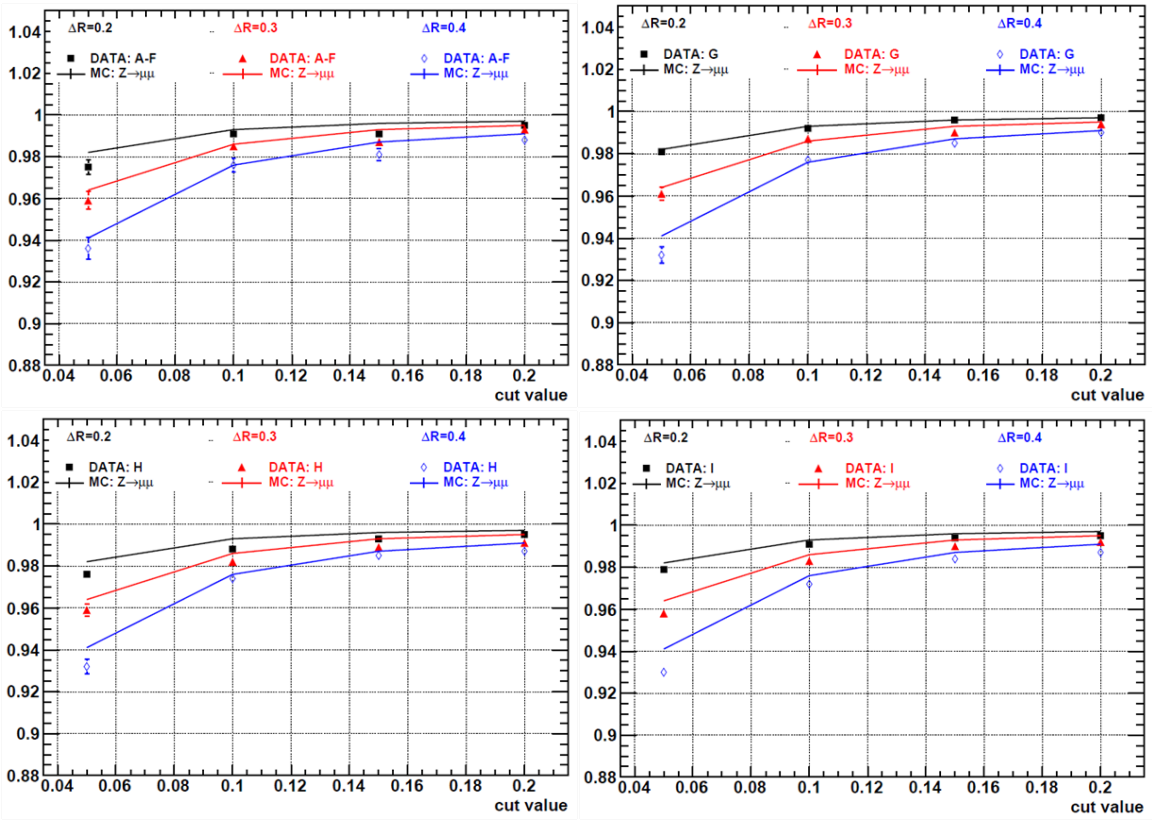

Figure 5.9: The muon isolation efficiency vs cut value for run period A-F (top left), G (top right), H (bottom left) and I (bottom right). The black is for $ptcone20/p_T$, the red is for $ptcone30/p_T$ and blue for $ptcone40/p_T$. The markers represent data and lines represent MC.

and the resolution on the curvature has a Gaussian distribution.

The muon momentum scale and smearing parameters are determined for the barrel and endcap separately. In total, four parameters are needed. The distributions sensitive to these four parameters are the combined muon mass distributions for barrel-barrel, barrel-endcap and endcap-endcap events. The peak positions (widths) are sensitive to the scale (resolution) parameters. The muon momenta in MC are smeared according to Eqn. 5.3. The smeared mass distributions are compared with the corresponding distributions in data, and a negative log-likelihood variable is calculated. The best smearing parameters are determined by minimizing the log-likelihood

Cone size	Isolation cut	ϵ_{iso} (Data)	ϵ_{iso} (MC)	Data/MC SF
0.2	0.05	$(97.8 \pm 0.10)\%$	$(98.2 \pm 0.03)\%$	99.6%
0.2	0.10	$(99.1 \pm 0.07)\%$	$(99.3 \pm 0.02)\%$	99.8%
0.2	0.15	$(99.4 \pm 0.05)\%$	$(99.6 \pm 0.01)\%$	99.8%
0.2	0.20	$(99.5 \pm 0.05)\%$	$(99.7 \pm 0.01)\%$	99.8%
0.3	0.05	$(95.9 \pm 0.14)\%$	$(96.4 \pm 0.04)\%$	99.5%
0.3	0.10	$(98.4 \pm 0.09)\%$	$(98.6 \pm 0.02)\%$	99.8%
0.3	0.15	$(98.9 \pm 0.07)\%$	$(99.3 \pm 0.02)\%$	99.6%
0.3	0.20	$(99.2 \pm 0.06)\%$	$(99.5 \pm 0.01)\%$	99.7%
0.4	0.05	$(93.2 \pm 0.17)\%$	$(94.1 \pm 0.05)\%$	99.0%
0.4	0.10	$(97.4 \pm 0.11)\%$	$(97.6 \pm 0.03)\%$	99.8%
0.4	0.15	$(98.4 \pm 0.09)\%$	$(98.7 \pm 0.02)\%$	99.7%
0.4	0.20	$(98.8 \pm 0.08)\%$	$(99.1 \pm 0.02)\%$	99.7%

Table 5.2: ϵ_{iso} and data/MC scale factor measured for different isolation cone sizes and isolation cut values applied to the probe muon. The isolation cut with cone size of 0.2 and cut value at 0.10 is determined to be used as the standard isolation cut in this analysis.

value using the Minuit program [5]. The parameters are also determined for two run periods A-F and G separately since worse momentum resolution was obtained in periods A-F.

For the barrel region, the momentum scale parameter C_1 is 1.0000 ± 0.0025 for period A-F and 0.9992 ± 0.0007 for period G. The momentum smearing parameter C_2 is $(2.72 \pm 0.56)\%$ for period A-F and $(1.50 \pm 0.20)\%$ for period G. For the endcap region, the momentum scale parameter C_1 is 0.9945 ± 0.0031 for period A-F and 1.0006 ± 0.0011 for period G. The momentum smearing parameter C_2 is $(3.82 \pm 0.65)\%$ for period A-F and $(3.51 \pm 0.26)\%$ for period G. Figure 5.10 and 5.11 show the dimuon invariant mass distributions for barrel-barrel, barrel-endcap and endcap-endcap events in data and MC for period A-F and G-I separately.

Table 5.3 show the measured muon momentum scale and additional smearing needed for different run periods. The systematics are assigned to cover possible variations for different run periods. The smearing parameters together with the statistical and systematic uncertainties are listed in Table 5.4 and 5.5.

Period	C_1 (Barrel)	C_1 (Endcap)	C_2 (Barrel)	C_2 (Endcap)
A-E	0.9994 ± 0.0034	0.9927 ± 0.0050	$(2.38 \pm 0.79)\%$	$(4.78 \pm 0.77)\%$
F	1.0005 ± 0.0033	0.9963 ± 0.0037	$(2.86 \pm 0.67)\%$	$(3.06 \pm 0.78)\%$
A-F	1.0000 ± 0.0025	0.9945 ± 0.0031	$(2.72 \pm 0.56)\%$	$(3.82 \pm 0.65)\%$
G1-6	0.9982 ± 0.0013	1.0005 ± 0.0021	$(1.31 \pm 0.34)\%$	$(3.11 \pm 0.46)\%$
H1	0.9992 ± 0.0015	1.0007 ± 0.0023	$(1.88 \pm 0.08)\%$	$(3.66 \pm 0.49)\%$
H2	0.9971 ± 0.0021	1.0070 ± 0.0032	$(0.96 \pm 0.49)\%$	$(2.58 \pm 0.66)\%$
I1	0.9993 ± 0.0010	1.0006 ± 0.0016	$(1.34 \pm 0.27)\%$	$(3.57 \pm 0.39)\%$
I2	1.0013 ± 0.0015	0.9982 ± 0.0020	$(1.98 \pm 0.36)\%$	$(3.32 \pm 0.43)\%$
G-I	0.9992 ± 0.0007	1.0006 ± 0.0011	$(1.50 \pm 0.20)\%$	$(3.51 \pm 0.26)\%$

Table 5.3: Muon momentum scale and resolution parameters measured for different run periods. They are determined using a negative log-likelihood minimization with Minuit. The correlations between C_1 and C_2 are negligible, and the correlations are $\sim 30\%$ between C_1 (Barrel) and C_1 (Endcap) and 20% between C_2 (Barrel) and C_2 (Endcap).

Period	C_1 (Barrel)	C_1 (Endcap)
A-F	$1.0000 \pm 0.0025 \pm 0.0006$	$0.9945 \pm 0.0031 \pm 0.0018$
G-I	$0.9992 \pm 0.0007 \pm 0.0021$	$1.0006 \pm 0.0011 \pm 0.0024$

Table 5.4: Muon momentum scale parameters together with statistical and systematic uncertainties for different run periods.

The transition region ($1.05 < |\eta| < 1.6$) and the CSC region ($2 < |\eta| < 2.4$) can have different momentum resolution, while they are treated as part of the endcap detector ($1.05 < |\eta| < 2.4$) here due to limited Z event statistics with both muons in transition or CSC regions. The momentum resolution parameters are varied by $\pm 1\sigma$ in MC simulation and compared to the data mass distributions with the smeared mass distributions with normal smearing parameters and with $\pm 1\sigma$ variations. The comparison plots can be found in Fig. 5.12, the data points are all within the two MC predictions with $\pm 1\sigma$ variation of the smearing parameters.

Period	C_2 (Barrel)	C_2 (Endcap)
A-F	$(2.72 \pm 0.56 \pm 0.34)\%$	$(3.82 \pm 0.65 \pm 0.96)\%$
G-I	$(1.50 \pm 0.20 \pm 0.54)\%$	$(3.51 \pm 0.26 \pm 0.93)\%$

Table 5.5: Muon momentum resolution parameters together with statistical and systematic uncertainties for different run periods.

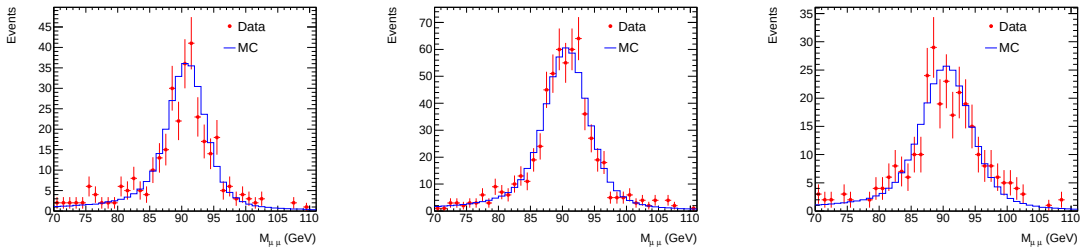

Figure 5.10: Dimuon invariant mass comparison between data and smeared MC for period A-F. The three plots are for barrel-barrel, barrel-endcap and endcap-endcap events. The average smearing parameters for period A-F are used.

5.4 Missing Transverse Energy

The missing transverse energy (E_T^{miss}) recovers information about non-interacting particles by inferring from the conservation of energy in the transverse plane. The missing transverse energy is ATLAS is primarily reconstructed from energy deposits in the calorimeter and reconstructed muon tracks. In practice, besides the hard scattering process of interest, there are many other sources such as the underlying events, multiple interactions, pile-up effect and coherent electronics noise, which lead to energy deposition and muon tracks. It is essential to classify the energy deposits into various types and calibrate them accordingly in order for an optimal E_T^{miss} measurement. Compensation for energy loss in dead regions and readout channels for the E_T^{miss} measurement is also important, but challenging.

The E_T^{miss} used in this thesis is reconstructed with a cell-based reconstruction algorithm, which includes contributions from transverse energy deposits in the calorime-

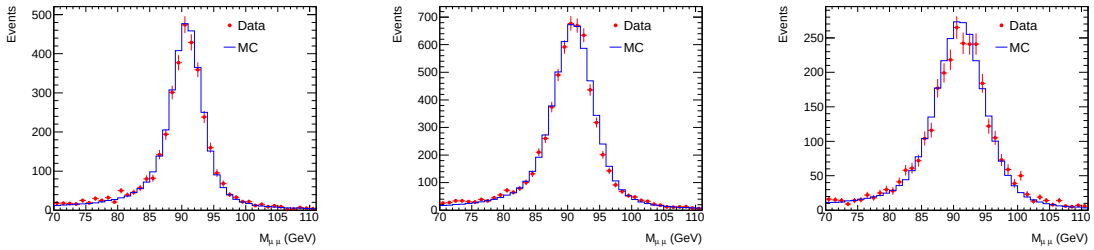

Figure 5.11: Dimuon invariant mass comparison between data and smeared MC for period G-I. The three plots are for barrel-barrel, barrel-endcap and endcap-endcap events. The average smearing parameters for period G-I are used.

ters, corrections for energy loss in the cryostat and measured muons:

$$\vec{E}_T^{miss} = \vec{E}_{T,\ LocHadTopo}^{miss} + \vec{E}_{T,\ muon}^{miss} - \vec{E}_{T,\ energy\ loss}^{miss} \tag{5.4}$$

where $E_{T,\ topo}^{miss}$ (`MET_LocHadTopo`) is the missing transverse energy calculated from topological cluster cells calibrated locally to electromagnetic and hadronic scale depending on the energy deposit classification. The term $E_{T,\ muon}^{miss}$ (`MET_MuonBoy`) accounts for the momentum carried by muons which escape the calorimeters. For isolated muons, the combined muon momentum is used. In this case an isolated muon is defined as one for which the ΔR to the nearest jet is at least 0.3, for all jets found by the anti-k_T algorithm with a cone of 0.4. For non-isolated muons and muons outside the inner detector acceptance ($2.4 < |\eta| < 2.7$), the muon momentum is obtained from the muon spectrometer track only. The third term $E_{T,\ energy\ loss}^{miss}$ (`MET_RefMuon_Track`) is sum of calo cells energy crossed by isolated muons, and is nonzero only for events with isolated muons as defined in the previous case. This term is subtracted from the sum of the first two to avoid double-counting the energy loss already taken into account by the combined muon momentum. This definition of E_T^{miss} is consistent with the recommendation by the JetEtMiss group at ATLAS [6].

Figure 5.13 is the E_T^{miss} distribution of a data sample corresponding to an integrated luminosity of 0.3 nb^{-1} at 7 TeV center-of-mass energy recorded in April 2010.

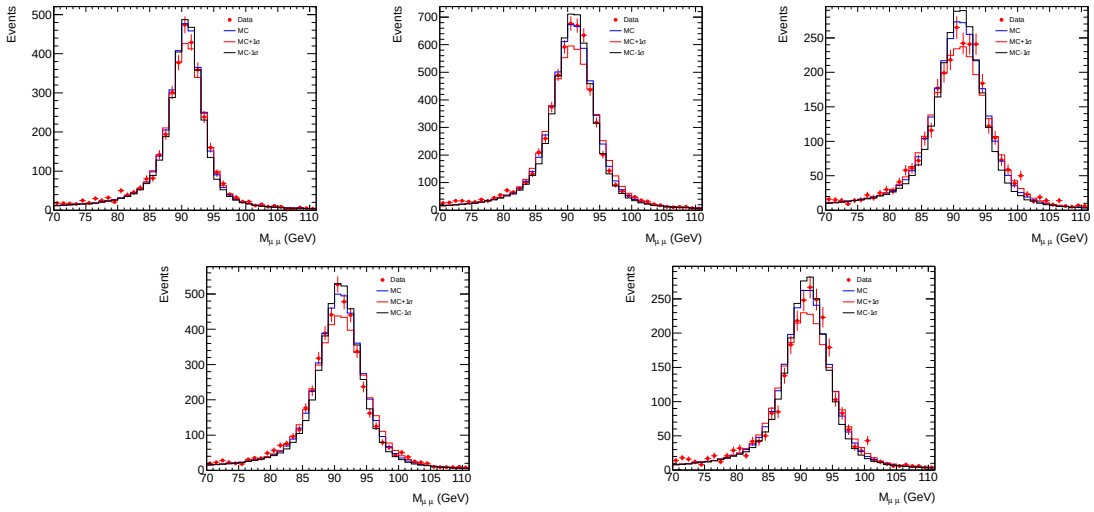

Figure 5.12: Dimuon invariant mass comparison between data and smeared MC. The smeared MC are made with normal smearing parameters and also the smearing parameters varied by $\pm 1\sigma$. The five plots are for events in barrel-barrel, barrel-endcap, endcap-endcap, at least one muon in transition region ($1.05 < |\eta| < 1.6$) and at least one muon in CSC region ($2 < |\eta| < 2.4$). These plots demonstrate the uncertainties on these smearing parameters are reasonable.

These events were triggered by the Minimum Bias Trigger Scintillators (MBTS) located outside the end-caps of the inner detector. The E_x^{miss} and E_y^{miss} resolution as a function of $\sum E_T$ shown in Figure 5.14 is a more quantitative evaluation of the E_T^{miss} performance. Both distributions of the data are found to be in good agreement with the Monte Carlo simulation.

5.5 Jet Finding

Jets are collections of particles that emerge from the fragmentation and hadronization of partons. ATLAS has implemented several jet finding algorithms including fixed sized cone algorithms, sequential recombination (k_T) algorithms and an algorithm based on event shape analysis. With this approach, different jet finders can be chosen for the hadronic final state depending on the topologies of interest. The anti-k_T algorithm using *topological cell clusters* (topo-clusters) has been used in this

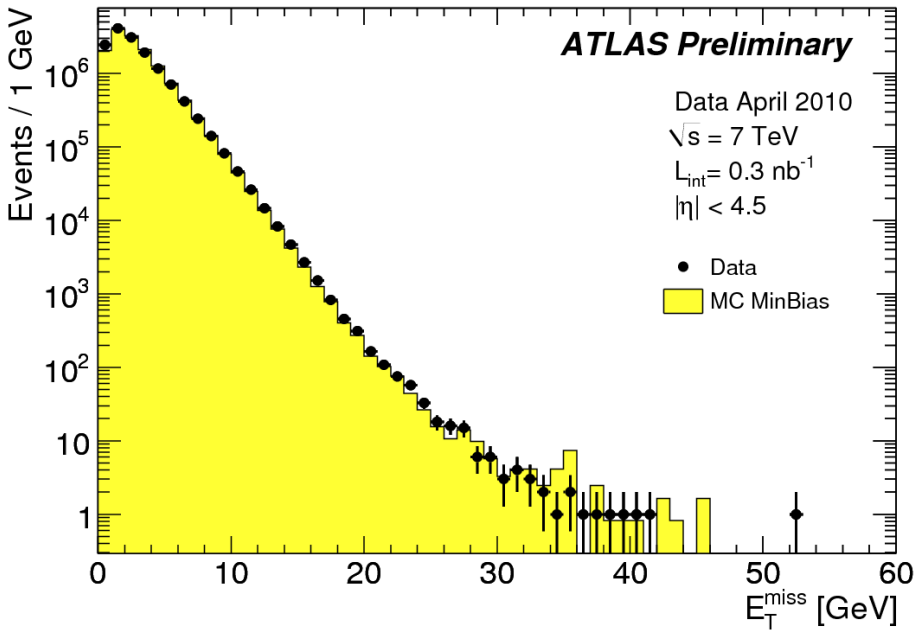

Figure 5.13: Distribution of missing transverse energy as measured in a data sample of 14.4 million selected minimum bias events (black dots) at 7 TeV center-of-mass energy, recorded in April 2010 [7]. The total integrated luminosity of this sample is about 0.3 nb^{-1}. The expected distribution from Monte Carlo is normalized to the number of events in data and then superimposed (yellow histogram).

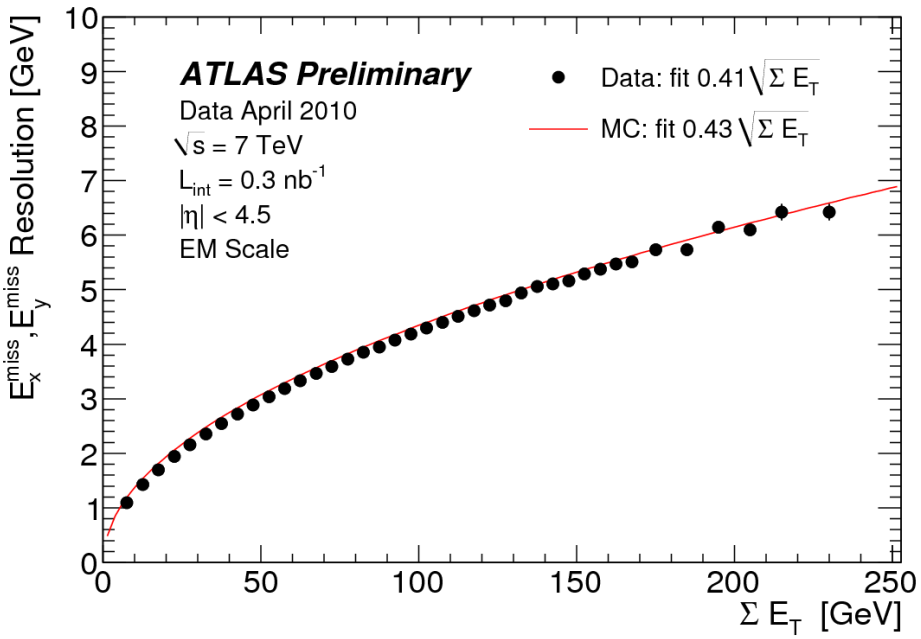

Figure 5.14: E_x^{miss} and E_y^{miss} resolution as a function of the total transverse energy as measured in a data sample of 14.4 million selected minimum bias events (black dots) at 7 TeV center-of-mass energy, recorded in April 2010 [7]. The total integrated luminosity of this sample is about 0.3 nb^{-1}. The red line represents a fit to the resolution obtained in the Monte Carlo simulation.

analysis because it has the best performance at ATLAS.

The calorimeter system is the most important detector for the jet reconstruction. There are about 200000 cells of various sizes and with different readout technologies and electrode geometries in the calorimeters. The topo-clusters are *proto-jets* with physically meaningful 4-momenta reconstructed from these cells. A variable called signal-to-noise ratio, or signal significance $\Gamma = E_{cell}/\sigma_{noise,cell}$ is used to select cells. The clustering starts with seed cells with $|\Gamma|$ above a certain threshold, i.e. >4. All directly neighboring cells and neighbors of neighboring cells with a $|\Gamma|$ above a secondary threshold, i.e. >2, are sequentially added to the cluster, iteratively. Finally, a ring of all nearest neighbors is collected into the cluster. The cells are combined using the 4-vector addition. The jet reconstruction rejects clusters with negative energy. The transverse energy of the cluster is:

$$E_T^{cluster} = \sum_{i \in cluster} E_{Ti}, \tag{5.5}$$

where i is the index of all cells in this topo-cluster. The pseudorapidity and azimuthal angle of the cluster are weighted by the transverse energy of each cell:

$$\eta^{cluster} = \frac{1}{E_T^{cluster}} \sum_{i \in cluster} E_{Ti}\eta_i, \qquad \phi^{cluster} = \frac{1}{E_T^{cluster}} \sum_{i \in cluster} E_{Ti}\phi_i. \tag{5.6}$$

Depending on local maxima or minima within these clusters, they can then be split or merged using a splitting algorithm.

In the next stage, the anti-k_T algorithm analyzes all pairs ij of input topo-clusters using a distance measure defined as:

$$d_{ij} = min(p_{T,i}^{-2}, p_{T,j}^{-2}) \frac{\Delta R_{ij}^2}{R^2} = min(p_{T,i}^{-2}, p_{T,j}^{-2}) \frac{\Delta\eta_{ij}^2 + \Delta\phi_{ij}^2}{R^2} \tag{5.7}$$

$$d_{ii} = p_{T,i}^{-2} \tag{5.8}$$

Here, $R = 0.4$ or 0.6. The algorithm searches the minimum d_{min} of d_{ij} and d_{ii} in the list of all topo-clusters. If $d_{min} = d_{ij}$, then cluster i and j are combined to be cluster k using 4-vector sum. This cluster k is added to the list, in the mean time cluster i and j are removed from it. Otherwise, cluster i is considered to be a jet by itself and removed from the list. This procedure is repeated until the list is empty.

The transverse momentum of the jets needs to be converted from the electromagnetic calibration of the ATLAS calorimeters to the calibrated hadronic scale. This is done by a calibration scheme with p_T- and η-dependence based on the Monte Carlo simulation. A jet energy scale correction is also applied to correct for noise, pile-up and additional calibration algorithmic effects. The jets at this stage are called physics jets.

Figure 5.15 shows the transverse momentum of topo-cluster jets with cone size $\Delta R = 0.6$ with first year ATLAS collision data. Figure 5.16 is the differential cross section as a function of jet transverse momentum for topo-cluster jets with cone size $\Delta R = 0.4$. Good agreement between data and MC indicate that the ATLAS jet reconstruction and calibration performance are in good shape.

5.6 Triggers

5.6.1 ATLAS Trigger System

The ATLAS trigger system consists of three stages: the hardware-based *Level 1* (L1) trigger and the software-based *Level 2* (L2) and *Event Filter* (EF) triggers, which are known collectively as the *High Level Trigger* (HLT). These three trigger levels are designed to reduce the LHC bunch crossing rate of 40 MHz to ~ 200 Hz, corresponding to an average data rate of ~ 300 MB/s.

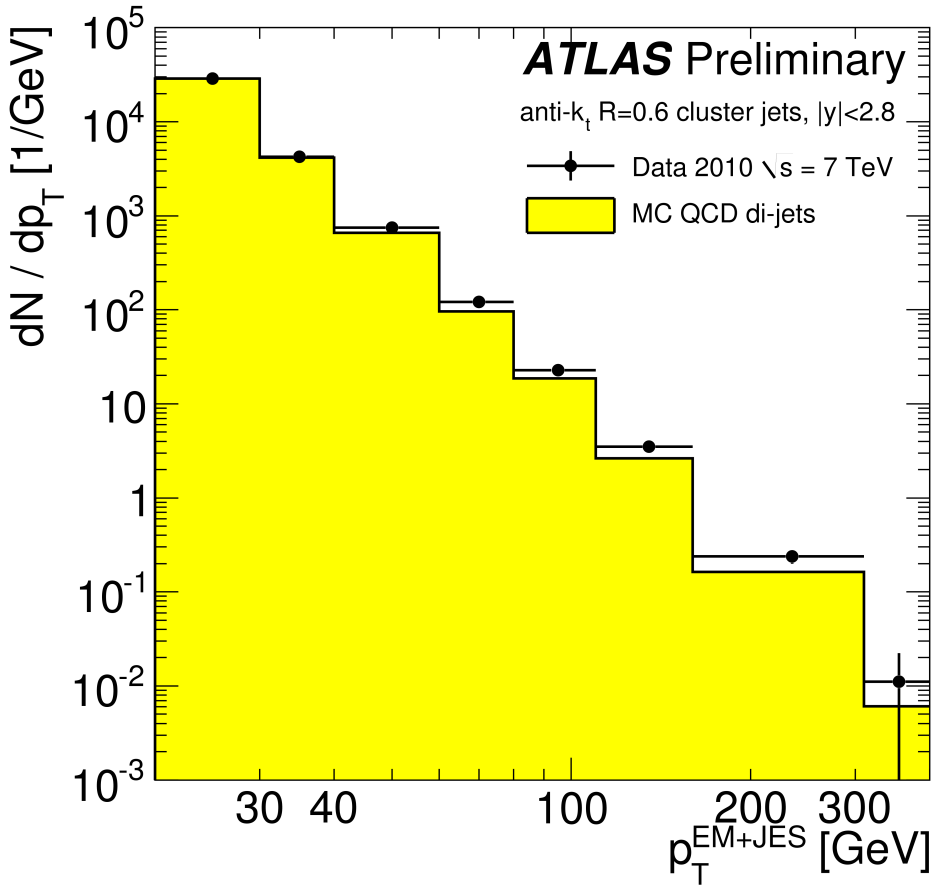

Figure 5.15: Distribution of jet transverse energy with 2010 collision data of 400 μb^{-1}. Black is data and yellow is for MC [8].

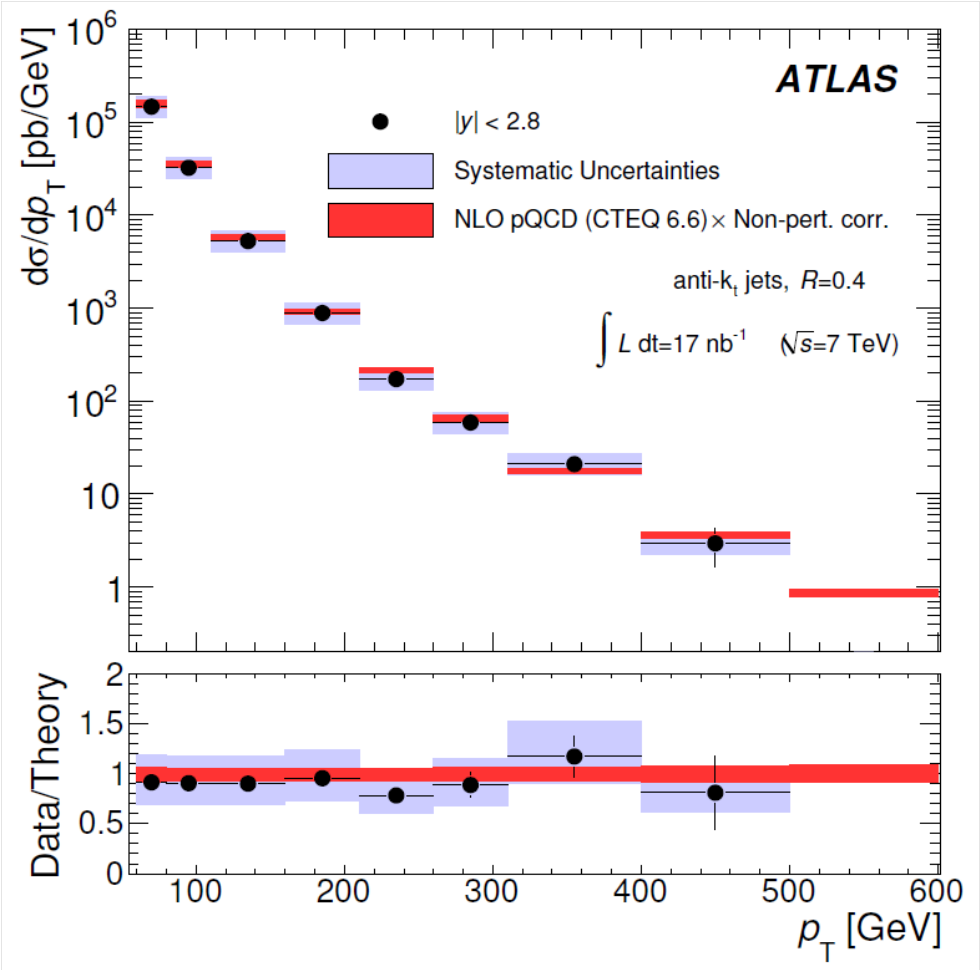

Figure 5.16: Distribution of inclusive jet differential cross section as a function of jet p_T integrated over the full rapidity region $|Y| < 2.8$ for topo-cluster jets with cone size $\Delta R = 0.4$. This plot corresponds to an integrated luminosity of 17 nb^{-1}. The black is data and red is MC. The error bars indicate the statistical uncertainty of the measurement, the gray shaded bands are systematic uncertainties. The ratio of data distribution and the MC distribution is shown below the plot [13].

Figure 5.17 is a schematic diagram of the ATLAS trigger system. The L1 trigger uses information from the calorimeter trigger towers and dedicated triggering layers in the muon spectrometer stored in front-end data pipelines. It is designed to achieve a latency of less than 2.5 μs with the implementation of fast custom electronics. The maximum output rate of the L1 trigger is 75 kHz (30 kHz in 2010 running). The L1 triggers also define *Regions of Interest* (RoIs) within the detector for HLT. The data for events accepted by the L1 trigger are transferred to and stored in the detector-specific Readout Buffers (ROB) pending the L2 decision. The L2 selection is based on fast algorithms processing partial event data within the RoIs identified by L1 and reduces the rate to $\sim$ 3 kHz. The average processing time of L2 is designed to be $\sim$ 40 ms/event. This number was $\sim$ 50 ms/event during the runs with instantaneous luminosity of $\sim 10^{32}\ cm^{-2}s^{-1}$ in 2010. The Event Builder assembles all event fragments from the ROBs for events accepted by L2, which will be used by the EF. The EF, mostly based on offline algorithms adapted to online running in the trigger system, reduces the rate to $\sim$ 200 Hz. The average EF processing time is designed to be $\sim$ 4 s/event. This number was $\sim$ 0.4 s/event during the runs with instantaneous luminosity of $\sim 10^{32}\ cm^{-2}s^{-1}$ in 2010.

The trigger system is configured via a trigger menu. This trigger menu defines trigger chains that start from a L1 trigger and specify a sequence of selection cuts for the specific trigger signatures. There are $\sim$ 500 triggers defined in the year 2010 trigger menu. Table 5.6 shows the key physics objects identified by the trigger system, the abbreviated trigger menu names and the L1 thresholds applied to transverse energy/momentum for calorimeter/muon triggers. These single object triggers can be combined to form more complex triggers to trigger multiple objects or RoI's. The trigger rate can be controlled by adjusting the trigger menu. In order to cope with the rapidly increasing luminosity, prescale factors can be applied to each L1 trigger and each HLT chain, such that only 1 in N events passing the trigger causes an event

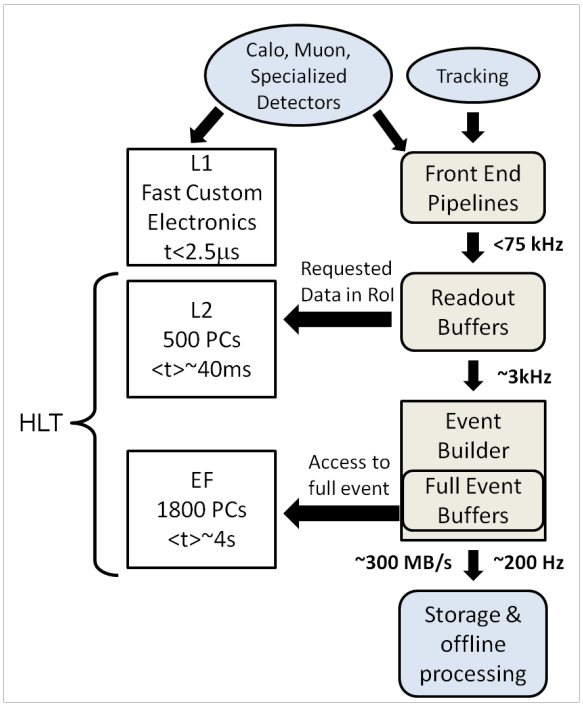

Figure 5.17: Schematic of the ATLAS trigger system [15].

to be accepted at that trigger level.

The L1 muon trigger utilizes a measurement of particle trajectories made by two parts of the muon detector: the Resistive Plate Chambers (RPC) in the barrel region and the Thin Gap Chambers (TGC) in the endcap region. L2 triggers refine the candidate from L1 with the precision data from the MDT's. At the EF level the full event data are accessible. W candidate events with muon final states are recorded with single muon triggers. The different triggers applied in different run periods are shown in Table 4.1. The trigger P_T thresholds are different in these four run periods due to the rapid increase in luminosity during the first year of LHC operation. At the start of data-taking the HLT was not enabled, therefore only the L1 trigger could be used.

Trigger Signature	L1	Representation HLT	L1 Thresholds [GeV]							
electron	EM	e	2	3	5	10	10i	14	14i	85
photon	EM	g	2	3	5	10	10i	14	14i	85
muon	MU	mu	0	6	10	15	20			
jet	J	j	5	10	15	30	55	75	95	115
forward jet	FJ	fj	10	30	55	95				
tau	TAU	tau	5	6	6i	11	11i	20	30	50
E_T^{miss}	XE	xe	10	15	20	25	30	35	40	50
$\sum E_T$	TE	te	20	50	100	180				
total jet energy	JE	je	60	100	140	200				
b jet	-	b								
MBTS	MBTS	mbts								
BCM	BCM	-								
ZDC	ZDC	-								
LUCID	LUCID	-								
Beam Pickup(BPTX)	BPTX	-								

Table 5.6: The key trigger objects with the abbreviation in the trigger menu and the L1 thresholds for each trigger signature in the menu at $\mathscr{L} = 10^{32}\ cm^{-2}s{-}1$. Thresholds are applied to transverse energy for calorimeter triggers and transverse momentum for muon triggers. Letter i appended to the threshold value indicates isolation cuts applied.

5.6.2 Muon Trigger Efficiencies

The muon trigger efficiencies $\epsilon_{trigger}$ are measured using the *tag-and-probe* method on $Z \to \mu\mu$ events. A *scale factor* (SF) quantifying the difference between the trigger efficiency measured in data and MC can be defined as:

$$SF = \frac{\epsilon(Z, Data)}{\epsilon(Z, MC)} \tag{5.9}$$

It is assumed that this scale factor measured using the *tag-and-probe* method is equivalent to the true scale factor. Both muons are required to pass all default offline muon selection cuts as described in Section 6.2. Here, the probe muon is only required to have p_T measured in the muon spectrometer with a correction for energy loss in calorimeter $P_T(MS) > 10\ GeV$. The *tag* muon must additionally pass a combination of *Muon Spectrometer* (MS-only), *Combined* (CB) and *Muon-Girl* MG muon triggers. This combination yields higher statistics. The invariant mass of the di-muon system must be within the Z mass window ($|M_{\mu\mu} - M_Z| < 20$ GeV) to ensure that the probe muon is from Z decays. Both muons are also required to be separated in azimuthal angle ϕ with $\Delta\phi > 0.5\pi$, and come from the same primary vertex with $|\Delta d_0(\mu\mu)| < 0.2$ mm and $|\Delta z_0(\mu\mu)| < 1$ mm.

Matching is then performed between each muon and the trigger RoI to determine if it was that particular muon which fired the trigger. A muon is considered matched if the ΔR between the trigger RoI and the offline muon object is less than 0.4 for L1 triggers or less than 0.2 for EF triggers. If a muon matches the trigger RoI, it is considered the *tag* muon. The other lepton is then identified as the *probe* muon and the trigger efficiency is calculated as:

$$\epsilon = \frac{N_{probes}^{matched}}{N_{probes}} \tag{5.10}$$

During the initial data taking period the muon trigger timing was still being tuned, thus the muon trigger signals were stretched to have an acceptance of 3 Bunch Crossings (BC) for a L1 trigger signal (-3 BC $< T_{L1\_MU} - T_{MBTS} < 1$ BC). Those events with a positive BC difference were not collected by the data acquisition system. The fraction of triggers at the correct bunch crossing is 86% (95%) for RPC (TGC) in the first trigger period and almost 100% for both RPC and TGC in the other trigger periods.

Figure 5.18 and 5.19 show the single muon trigger efficiency in data as a function of muon P_T for four trigger periods in barrel and endcap regions. The trigger efficiency reaches the plateau region for $P_T > 20$ GeV within the statistical uncertainty. Figure 5.20 shows the trigger efficiency in MC.

The average muon trigger efficiency is calculated by taking into account the integrated luminosity in different trigger periods. The efficiencies as a function of offline muon P_T, η and ϕ for data and MC are shown in Fig. 5.21 to 5.23. Fourteen η bins (-1.05, -0.908, -0.791, -0.652, -0.476, -0.324, -0.132, 0, 0.132, 0.324, 0.476, 0.652, 0.791, 0.908, 1.05) and sixteen ϕ bins (from $-15/16\pi$ to $17/16\pi$) are used for the RPC. Four η bins (-2.4, -1.95, -1.05 1.05 ,1.95, 2.4) and eight ϕ bins (from $-13/12\pi$ to $11/12\pi$) are used for the TGC. The choices of binnings are determined by the RPC and TGC geometry.

Table 5.7 shows the trigger efficiency for muons with $P_T > 20$ GeV for four trigger periods together with the average trigger efficiency and data/MC scale factor. The luminosity-weighted trigger efficiency is $(77.12 \pm 0.37)\%$ for the barrel and $(93.42 \pm 0.22)\%$ for the endcap. The corresponding trigger efficiency in MC is $(79.07 \pm 0.10)\%$ for the barrel and $(95.12 \pm 0.05)\%$ for the endcap. The data/MC scale factor is 0.9754 ± 0.0048(stat) for the barrel and 0.9821 ± 0.0024(stat) for the endcap.

To estimate the systematic uncertainty of the scale factor, the following sources are considered:

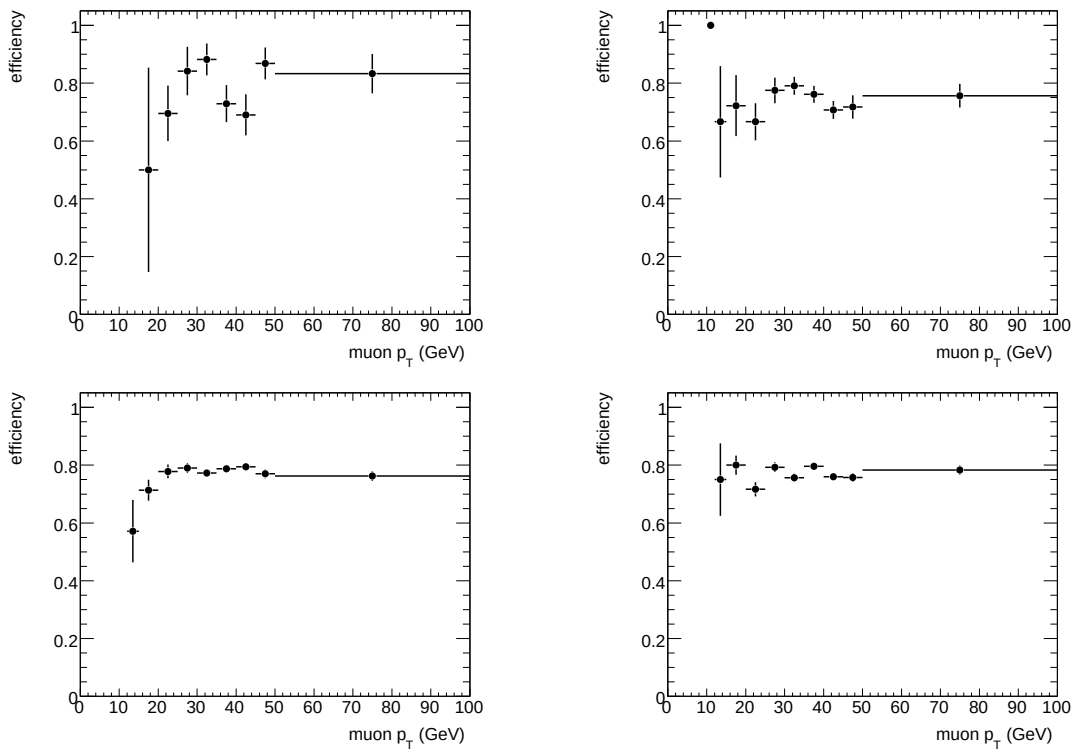

Figure 5.18: Muon trigger efficiency as a function of muon P_T in the barrel region for four trigger periods: top left for A to E3; top right for E4 to G1; bottom left for G2 to H1 run 167576 and bottom right for H1 run 167607 to I2

1. The matching cone size for the offline muon and online trigger objects is varied. The default cone size used is 0.4 (0.2) for L1 (HLT), and the studies are repeated using 0.3 (0.1) for L1 (HLT) and also 0.5 (0.3) for L1 (HLT). The scale factor changes by 0.0005 (0.0043) for barrel (endcap).

2. The η-dependence of the data/MC scale factor is checked. The scale factor changes by 0.0044 (0.0025) for the barrel (endcap) across the whole η range.

3. The number of same sign events is used to estimate the QCD background. The resulting variation on the scale factor is less than 0.01%.

4. The size of the mass window is varied ($\pm 15, \pm 20$ GeV) and the scale factor is found to change by 0.0020 (0.0006) for the barrel (endcap).

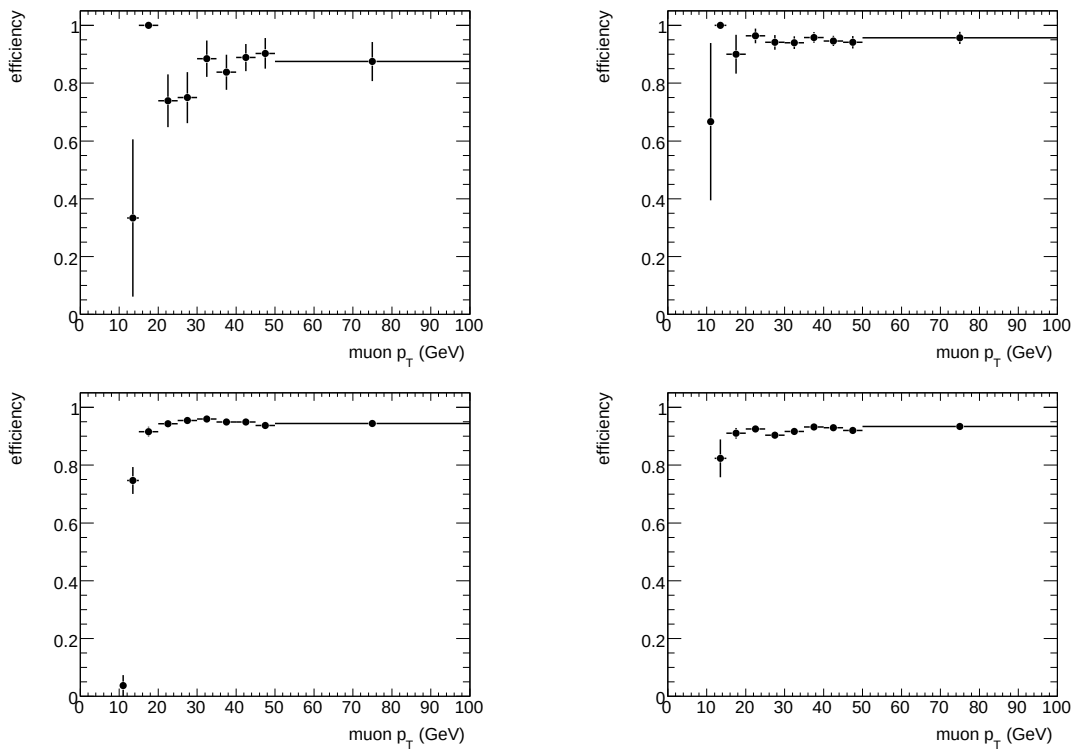

Figure 5.19: Muon trigger efficiency as a function of muon P_T in the endcap region for four trigger periods: top left for A to E3; top right for E4 to G1; bottom left for G2 to H1 run 167576 and bottom right for H1 run 167607 to I2

The final data/MC scale factor including systematic errors is found to be 0.9769 ± 0.0084 (0.9835 ± 0.0057) for the barrel (endcap).

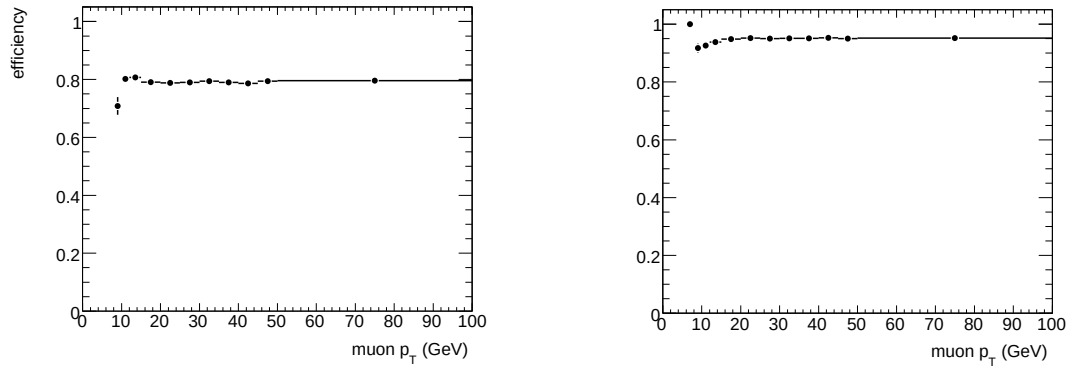

Figure 5.20: Muon trigger efficiency as a function of muon P_T for the barrel (left plot) and endcap regions (right plot) in MC.

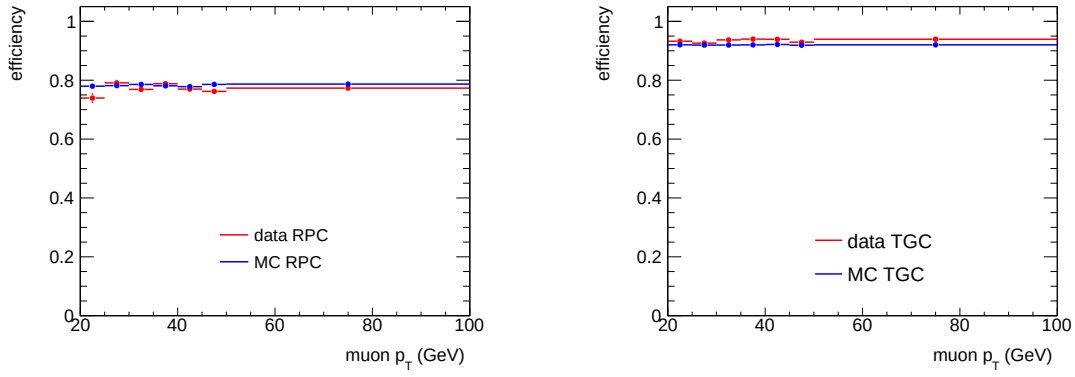

Figure 5.21: Data and MC comparison for average muon trigger efficiencies as a function of muon p_T for the barrel (left plot) and endcap (right plot) regions. HLT triggers are used in data while only L1_MU10 is used in MC. The interesting region for the W analysis is for muons with $P_T > 20$ GeV.

Period	RPC efficiency	TGC efficiency
A - E3	$(78.3 \pm 2.7)\%$	$(84.8 \pm 2.5)\%$
E4 - G1	$(74.5 \pm 1.4)\%$	$(94.9 \pm 0.8)\%$
G2 - I1 (167576)	$(78.1 \pm 0.6)\%$	$(94.8 \pm 0.3)\%$
I1 (167607) - I2	$(77.0 \pm 0.6)\%$	$(92.5 \pm 0.4)\%$
Luminosity-weighted average	$(77.3 \pm 0.4)\%$	$(93.6 \pm 0.2)\%$
MC	$(79.1 \pm 0.1)\%$	$(95.1 \pm 0.1)\%$
Data/MC SF	$(97.7 \pm 0.8)\%$	$(98.4 \pm 0.6)\%$

Table 5.7: Trigger efficiency for muons with $P_T > 20$ GeV for four trigger periods together with the average trigger efficiency and data/MC scale factor.

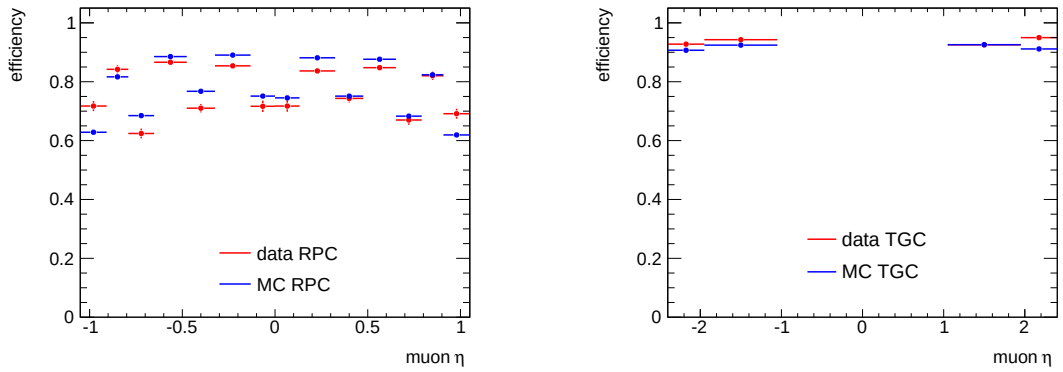

Figure 5.22: Data and MC comparison for average muon trigger efficiencies as a function of muon η for the barrel (left plot) and endcap (right plot) regions. Only probe muons with $P_T > 20$ GeV are used.

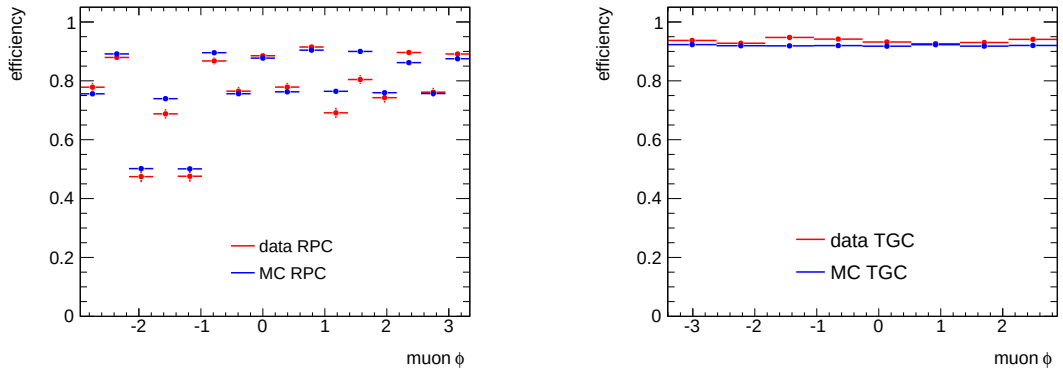

Figure 5.23: Average muon trigger efficiency as a function of muon ϕ for the barrel and endcap regions in data and MC. Only probe muons with $P_T > 20$ GeV are used.

CHAPTER VI

Measurement of $W \to \mu\nu$ Cross Section

6.1 Method of Cross Section Extraction

The formula used to extract the cross section is

$$\sigma_W \times Br = \frac{N_{obs} - N_{bkg}}{\varepsilon \cdot \mathscr{A} \cdot \mathscr{L}} \tag{6.1}$$

where,

- σ_W is the total W production cross section, Br is the branching ratio for W decay to a muon and muon-neutrino;
- N_{obs} is the number of observed events in data. This number can be extracted from the event selection cut flow tables in Section 6.2;
- N_{bkg} is the number of background events. It is estimated using MC simulation and/or data driven methods described in Section 6.4;
- $\varepsilon \cdot \mathscr{A}$ is the product of efficiency and acceptance which are combined and treated as one number. This number is determined from MC simulations with corrections using data control samples. It is presented in Section 6.3;
- $\mathscr{L}$ is the integrated luminosity of the data and is $35.2 \pm 1.2\ pb^{-1}$.

The systematic uncertainties associated with above terms are studied in detail and reported in corresponding sections as well. The W production cross section measurement is reported in section 6.5 based on Equation 6.1.

6.2 Event Selection

The selection of $W \rightarrow \mu\nu$ candidates is divided into two steps. A *pre-selection* consists of requirements to ensure a good event and preliminary cuts to select high transverse momentum muons from pp collisions in the event. The second step is the *final selection* with stronger cuts applied to the muon and the neutrino system for W selection.

6.2.1 Pre-selection

The first stage of the event selection is the pre-filter applied when converting AOD to D3PD ntuples. This pre-filter requires at least one muon or electron candidate with $p_T > 10GeV$ and $|\eta| < 2.7$. Collision candidates are selected by requiring a primary vertex with at least three tracks, consistent with the beam-spot position. To reduce contamination from cosmic-ray or beam-halo events, the primary vertex position along the beam axis should be within 15 cm of the nominal position (this primary vertex distribution has a measured longitudinal RMS of 6.2 cm). This event has to be in the *Good Run List* (GRL), i.e. in the luminosity blocks for which the sub-detectors were fully functional, and passes the trigger requirement corresponding to the run period as shown in Table 4.1.

To remove effects from EM coherent noise, HEC spikes, cosmics and beam background on jet and missing transverse energy reconstruction, "Loose" jet cleaning cuts, as defined by the jet/MET group [6], are applied. An event is removed if at least one bad jet with E_T^{jet} (EM scale with JES correction) $\geq 20\ GeV$ is found. This process is called MET cleaning.

Lastly, if at least one muon satisfies the following criteria, an event is considered to have passed the pre-selection.

- Reconstructed as a combined staco muon.
- Transverse momentum of the muon $p_T > 15\ GeV$, for good trigger efficiency.
- Pseudorapidity of the muon within the range $|\eta| < 2.4$ because of the muon spectrometer trigger coverage.
- Transverse momentum of the muon measured standalone in the muon spectrometer corrected for calorimeter energy loss $p_T(MS) > 10\ GeV$. This cut ensures that this muon is well identified by the muon spectrometer and removes muons from pion and kaon decays.
- The difference in transverse momentum of the muon measured by muon spectrometer and by inner detector is within the range $|p_T(MS) - p_T(ID)| < 15\ GeV$. This cut also removes poorly reconstructed tracks and muons from pion and kaon decays.
- Longitudinal impact parameter w.r.t. the primary vertex within the range $|z_0| < 10$ mm to remove muons from cosmic rays.

The distributions of muon kinematic variables and missing transverse energy after the pre-selection are shown in Figure 6.1-Figure 6.3 and Figure 6.4. All the Monte-Carlo events are normalized to the total integrated luminosity of data except the QCD events which are normalized to the muon low p_T spectrum. A scale factor of 0.5 is applied to the MC QCD samples in addition to luminosity normalization. As seen in these plots, the events are dominated by the QCD background at this stage of the selection. In these plots, dots with error bars represent data, the stacked histograms with different colors indicate different background contributions, the open histograms are the sum of the expected W signal and the background contributions, which can be compared directly with data. The shapes of these distributions from data and MC are in good agreement.

6.2.2 $W \to \mu\nu$ Event Selection

The selection cuts at the second stage ensure a good $W \to \mu\nu$ event by further requiring one and only one good muon and large missing transverse energy, as well as

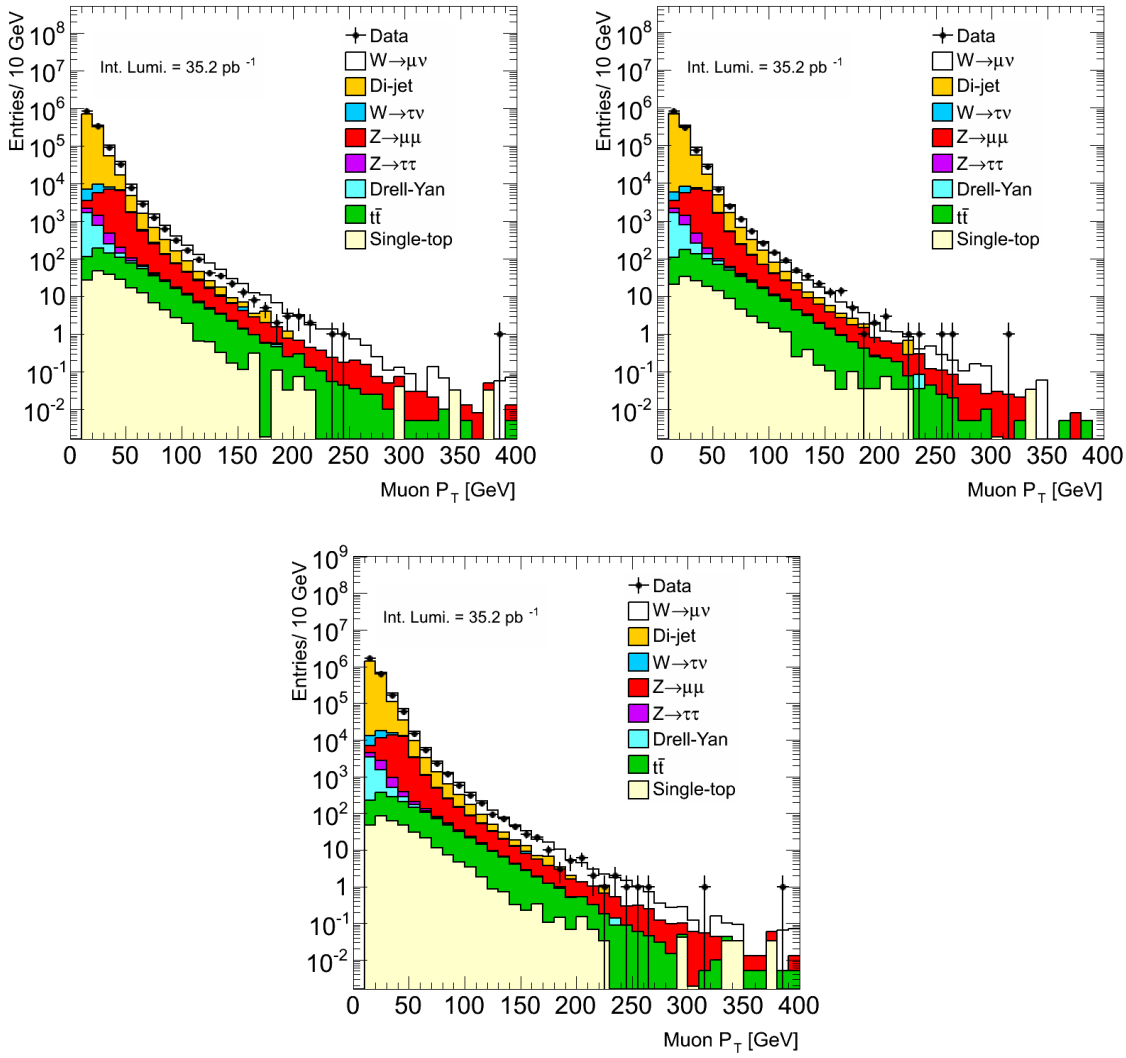

Figure 6.1: Muon transverse momentum after preselection for μ^+ (top left), μ^- (top right) and all muons (bottom). Black dots are for data, the color blocks are for various MC processes.

the muon plus neutrino to be consistent with a W. This set of selection cuts is also referred to as *final selection*. The detail selection criteria are given below:

- The transverse momentum of the muon, p_T, must be greater than 20 GeV. The increased transverse momentum cut compared to that used in pre-selection is due to the muon trigger threshold increase in later run periods with increased luminosity.
- Muon isolation is required such that the sum of track p_T in a cone $\Delta R = 0.2$ weighted by p_T of the muon, $ptcone20/p_T$ must be less that 0.1. The isolation requirement mainly rejects QCD backgrounds.

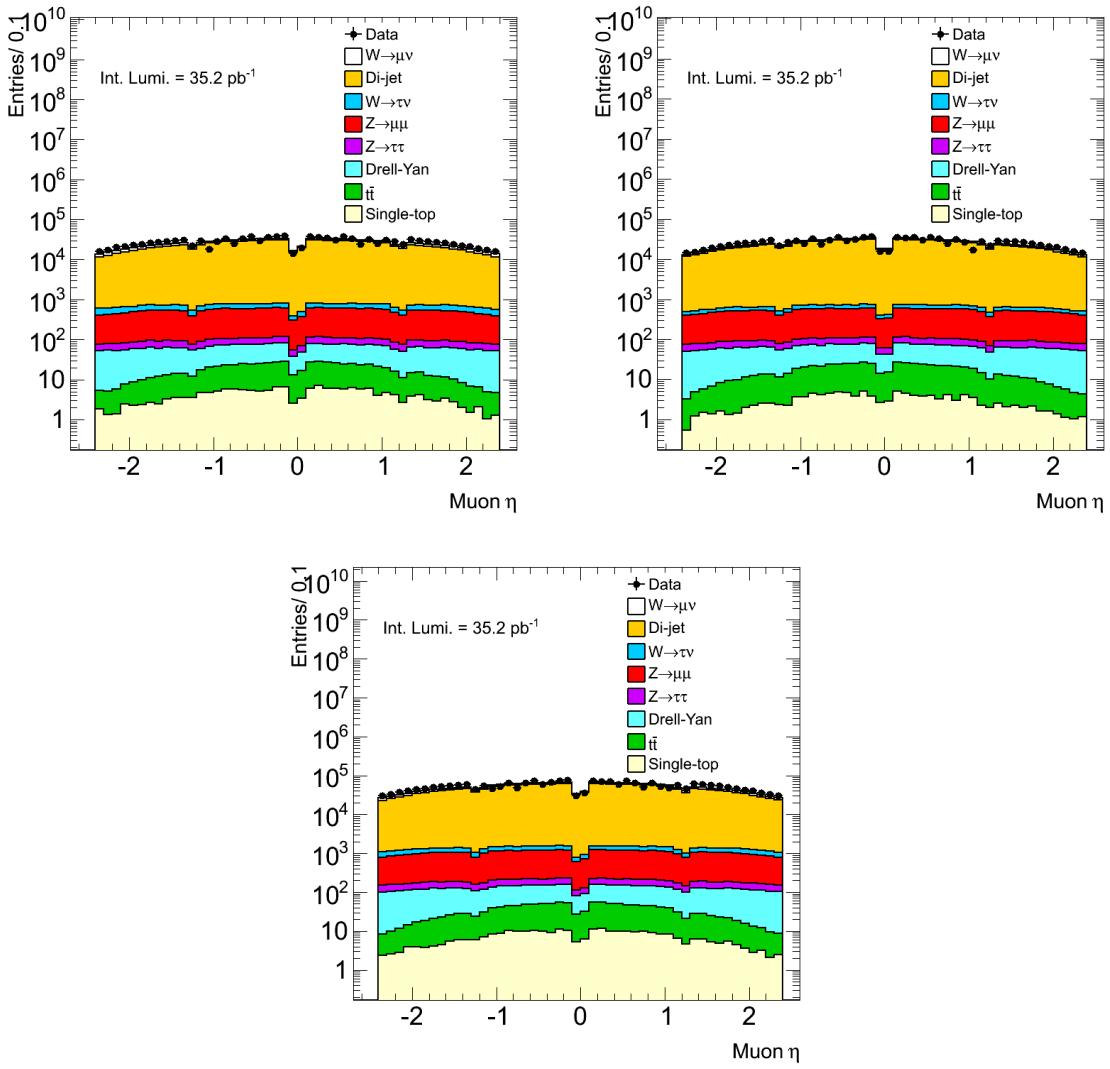

Figure 6.2: Muon pseudorapidity after preselection for μ^+ (top left), μ^- (top right) and all muons (bottom). Black dots are for data, the color blocks are for various MC processes.

- Missing transverse energy E_T^{miss} must be greater than 25 GeV.
- Transverse mass of the muon and missing energy, M_T, is required to be greater than 40 GeV.

The distribution of muon kinematic variables and missing transverse energy after the final selection are shown in Figure 6.5-Figure 6.7 and Figure 6.8. Figure 6.9 and Figure 6.10 are the transverse momentum and transverse mass of the W candidates, respectively. Data and MC predictions are in good agreement in this final selection

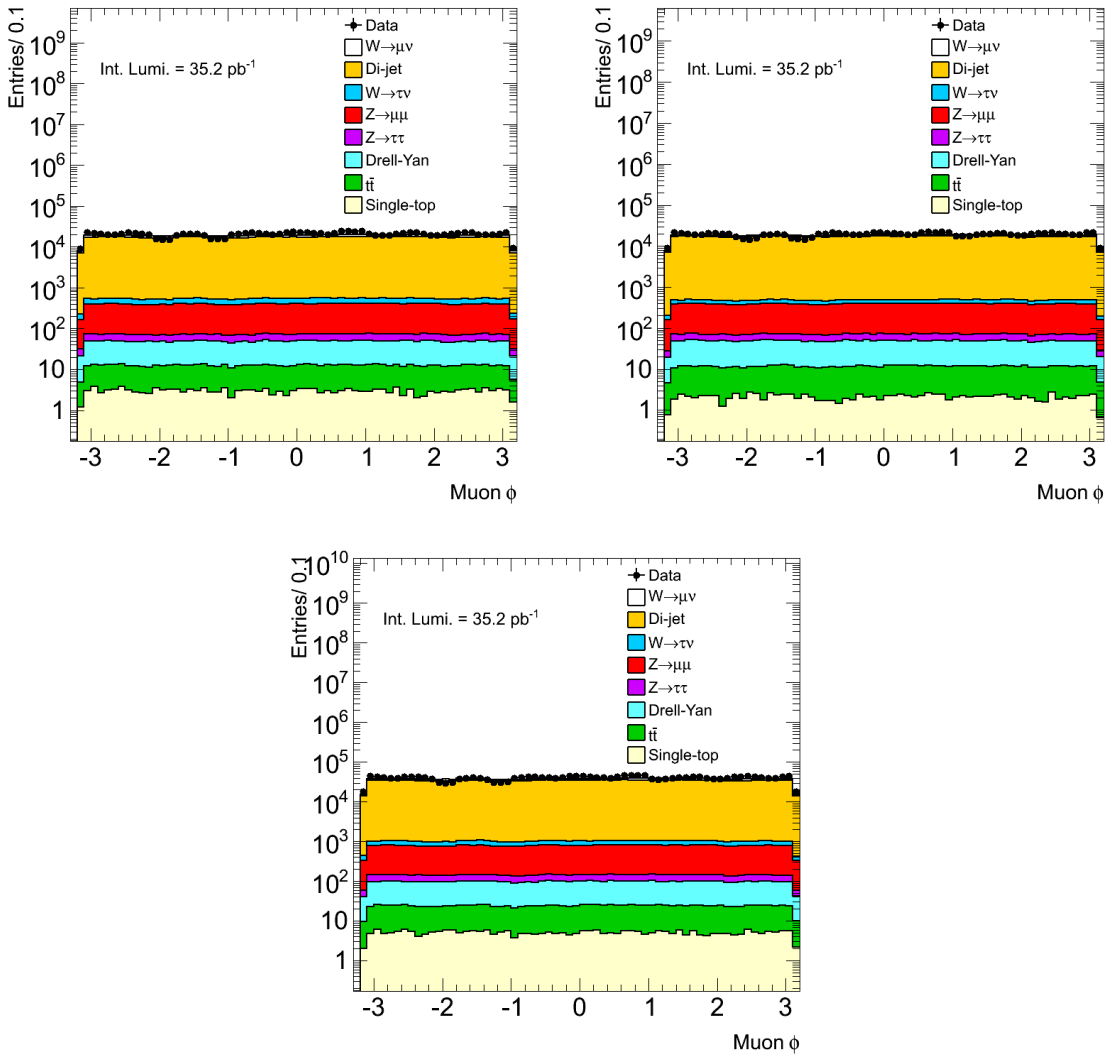

Figure 6.3: Muon azimuthal angle after preselection for μ^+ (top left), μ^- (top right) and all muons (bottom). Black dots are for data, the color blocks are for various MC processes.

stage.

The event selection cut flow, with the numbers of $W \to \mu\nu$ candidates remaining after each cut, are divided into four tables as in Table 6.1, 6.2, 6.3 and 6.4. This division is in accordance with the change of muon triggers in different data runs as listed in Table 4.1. The cut flow for MC samples is shown in the next section to determine signal detection efficiency.

Cut	Events	Rel. Eff.	W^+	W^-
D3PD Pre-filter	5281877	-	-	-
GRL	4544497	86.0%	-	-
MET Cleaning	4526359	99.6%	-	-
Primary Vertex	3337208	73.1%	-	-
Muon P_T, η, z_0	69056	2.1%	36085	32971
Muon $P_T(MS)$, $P_T(ID)$	54960	79.6%	28363	26597
Muon $P_T > 20\ GeV$	18853	34.3%	10086	8767
Muon Isolation	7687	40.8%	4335	3352
Missing E_T	3214	41.8%	1921	1293
Transverse Mass M_T	3097	96.4%	1858	1239
Trigger	2892	93.4%	1739	1153

Table 6.1: Event selection cut flow for Run Period A-E3

Cut	Events	Rel. Eff.	W^+	W^-
D3PD Pre-filter	4094365	-	-	-
GRL	3568708	87.2%	-	-
MET Cleaning	3560841	99.8%	-	-
Primary Vertex	3172844	89.1%	-	-
Muon P_T, η, z_0	102562	3.2%	53518	49044
Muon $P_T(MS)$, $P_T(ID)$	86988	84.8%	44823	42165
Muon $P_T > 20\ GeV$	30065	34.6%	15822	14243
Muon Isolation	12306	40.9%	6854	5452
Missing E_T	5126	41.7%	3114	2012
Transverse Mass M_T	4940	96.4%	3014	1926
Trigger	4798	97.1%	2942	1856

Table 6.2: Event selection cut flow for Run Period E4-G1

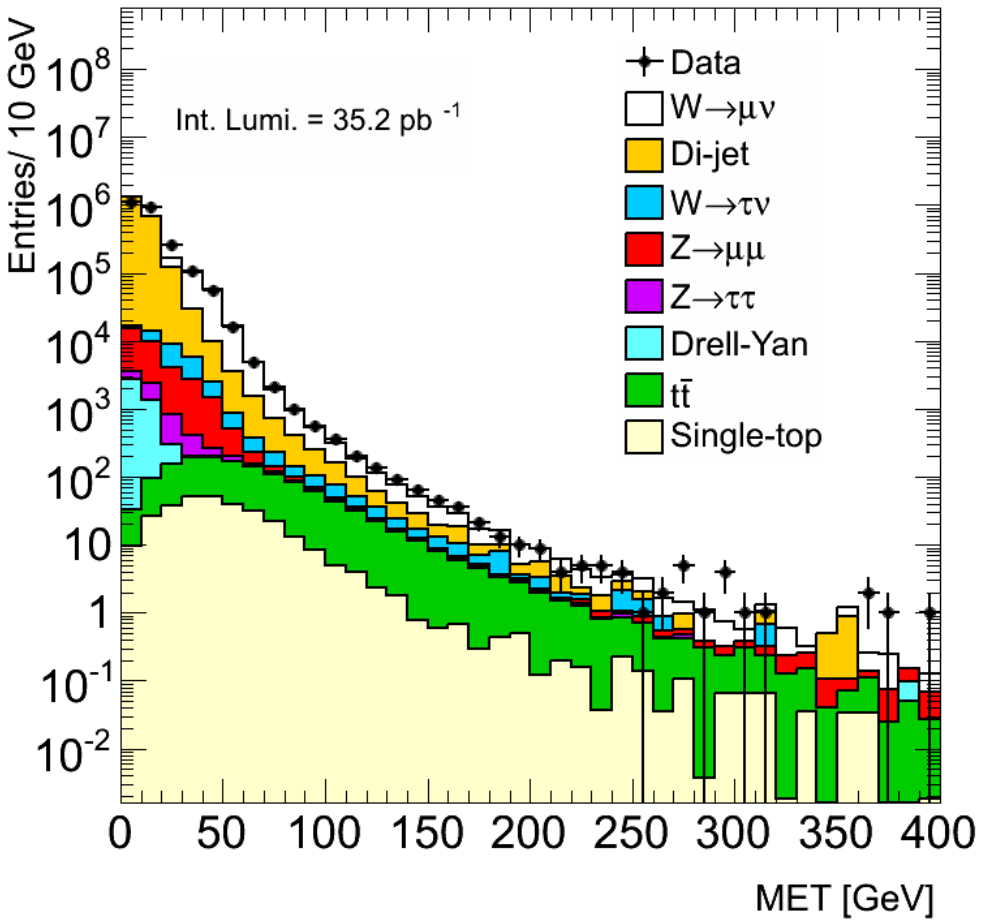

Figure 6.4: The distribution of missing transverse momentum after preselection. Black dots are for data, the color blocks are for various MC processes.

6.3 Acceptance and Uncertainties

The same event selection process is applied to Monte Carlo samples, except that the GRL cut and MET cleaning are used for data only. Table 6.5 shows the event selection cut flow of the signal processes including prompt muon decay from W ($W \to \mu\nu$) and cascade muon decay from tau in the $W \to \tau\nu$ process ($W \to \tau\nu \to \mu\nu$). The total number of MC events in the first row of the table are inferred from the total cross section, branching ratio, the k-factor of the corresponding process, and the total integrated luminosity of data ($\sigma_W \times Br \times k \times \mathscr{L}$). The other rows are extracted from

Cut	Events	Rel. Eff.	W^+	W^-
D3PD Pre-filter	15848109	-	-	-
GRL	12098000	76.3%	-	-
MET Cleaning	12083736	99.9%	-	-
Primary Vertex	11639703	96.3%	-	-
Muon P_T, η, z_0	1220374	10.5%	632558	587816
Muon $P_T(MS)$, $P_T(ID)$	1114677	91.3%	573360	541317
Muon $P_T > 20\ GeV$	386243	34.7%	203805	182438
Muon Isolation	158736	41.1%	88696	70040
Missing E_T	68116	42.9%	41078	27038
Transverse Mass M_T	65538	96.2%	39699	25839
Trigger	64976	99.1%	39374	25602

Table 6.3: Event selection cut flow for Run Period G2-I1(till run 167576)

Cut	Events	Rel. Eff.	W^+	W^-
D3PD Pre-filter	9490632	-	-	-
GRL	9034736	95.2%	-	-
MET Cleaning	9025027	99.9%	-	-
Primary Vertex	8838203	97.9%	-	-
Muon P_T, η, z_0	1352714	15.3%	700213	652501
Muon $P_T(MS)$, $P_T(ID)$	1251081	92.5%	643357	607724
Muon $P_T > 20\ GeV$	434965	34.8%	228768	206197
Muon Isolation	178933	41.1%	99800	79133
Missing E_T	77047	43.1%	46146	30901
Transverse Mass M_T	73872	95.9%	44385	29487
Trigger	72560	98.2%	43587	28973

Table 6.4: Event selection cut flow for Run Period I1(from run 167607)-I2

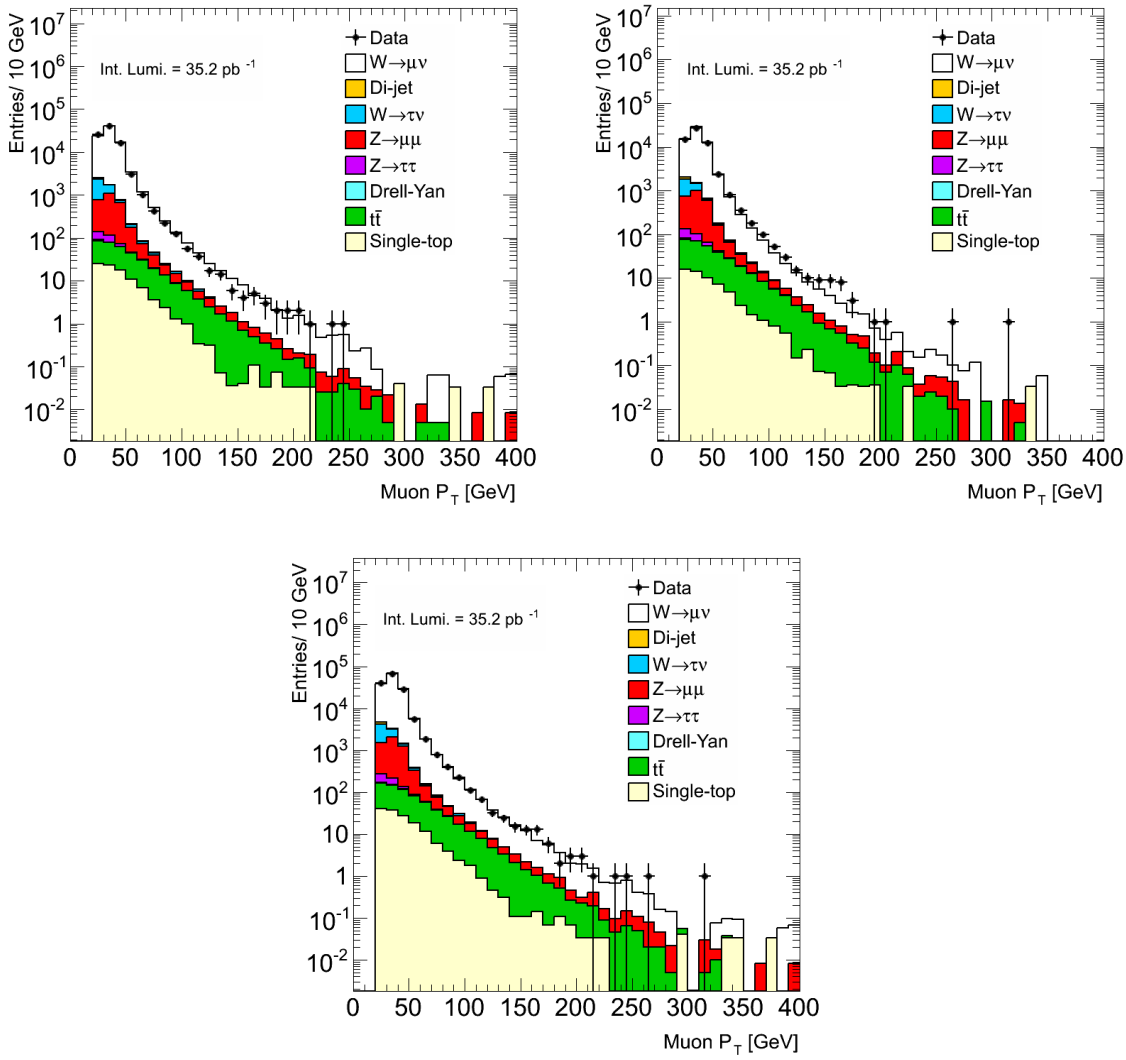

Figure 6.5: Distribution after final selection of muon transverse momentum for W^+ candidates (top left), W^- (top right) and all W candidates (bottom). Black dots are for data, the color blocks are for various MC processes.

the MC event selection. The number of events are normalized to the total integrated luminosity. The cut "D3PD PF, PV" includes D3PD pre-filter and primary vertex cut. "Muon cuts" groups selection of all cuts related to the muon quality, including cuts on muon kinematics and muon isolation. The combined efficiency-acceptance is then determined from the cut flow by comparing the number of events passing the full event selection to the number of total MC events, i.e. $\varepsilon \cdot \mathscr{A} = N_{trigger}/N_{totalMC}$. The

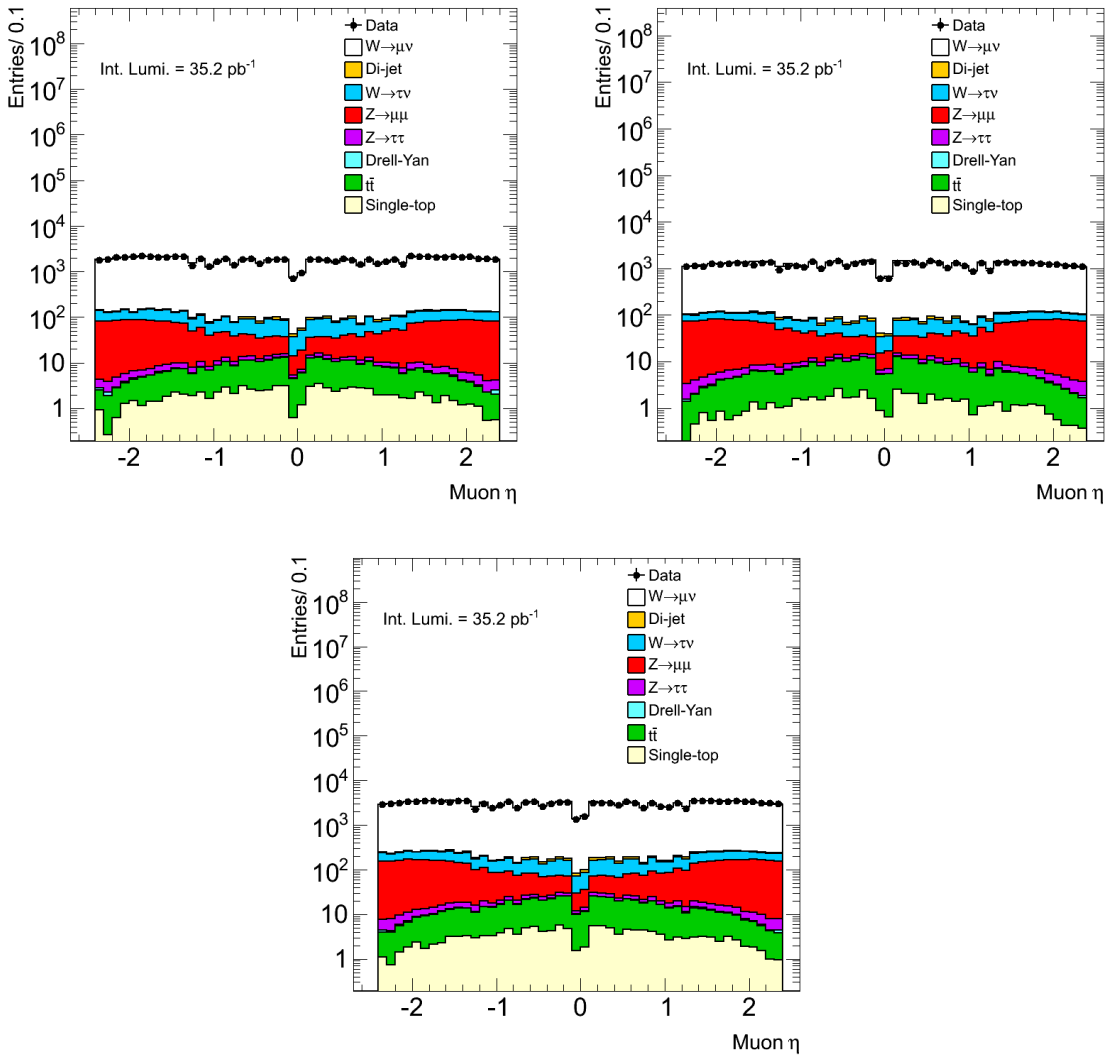

Figure 6.6: Distribution after final selection of muon pseudorapidity for W^+ candidates (top left), W^- (top right) and all W candidates (bottom). Black dots are for data, the color blocks are for various MC processes.

efficiency-acceptance of $W \to \mu\nu$ process, $(\varepsilon \cdot \mathscr{A})_\mu$, is determined to be (37.38±0.03)%, and that of $W \to \tau\nu \to \mu\nu$ process, $(\varepsilon \cdot \mathscr{A})_\tau$, is $(6.30 \pm 0.04)\%$. The final detection acceptance is the combination of both processes: $\varepsilon \cdot \mathscr{A} = (\varepsilon \cdot \mathscr{A})_\mu + (\varepsilon \cdot \mathscr{A})_\tau Br(\tau \to \mu\nu)$, which is found to be $(38.48 \pm 0.03)\%$. Only statistical uncertainties are shown at this point. The branching ratio of muon decay from tau, $Br(\tau \to \mu\nu)$, used here is $(17.39 \pm 0.04)\%$ [43].

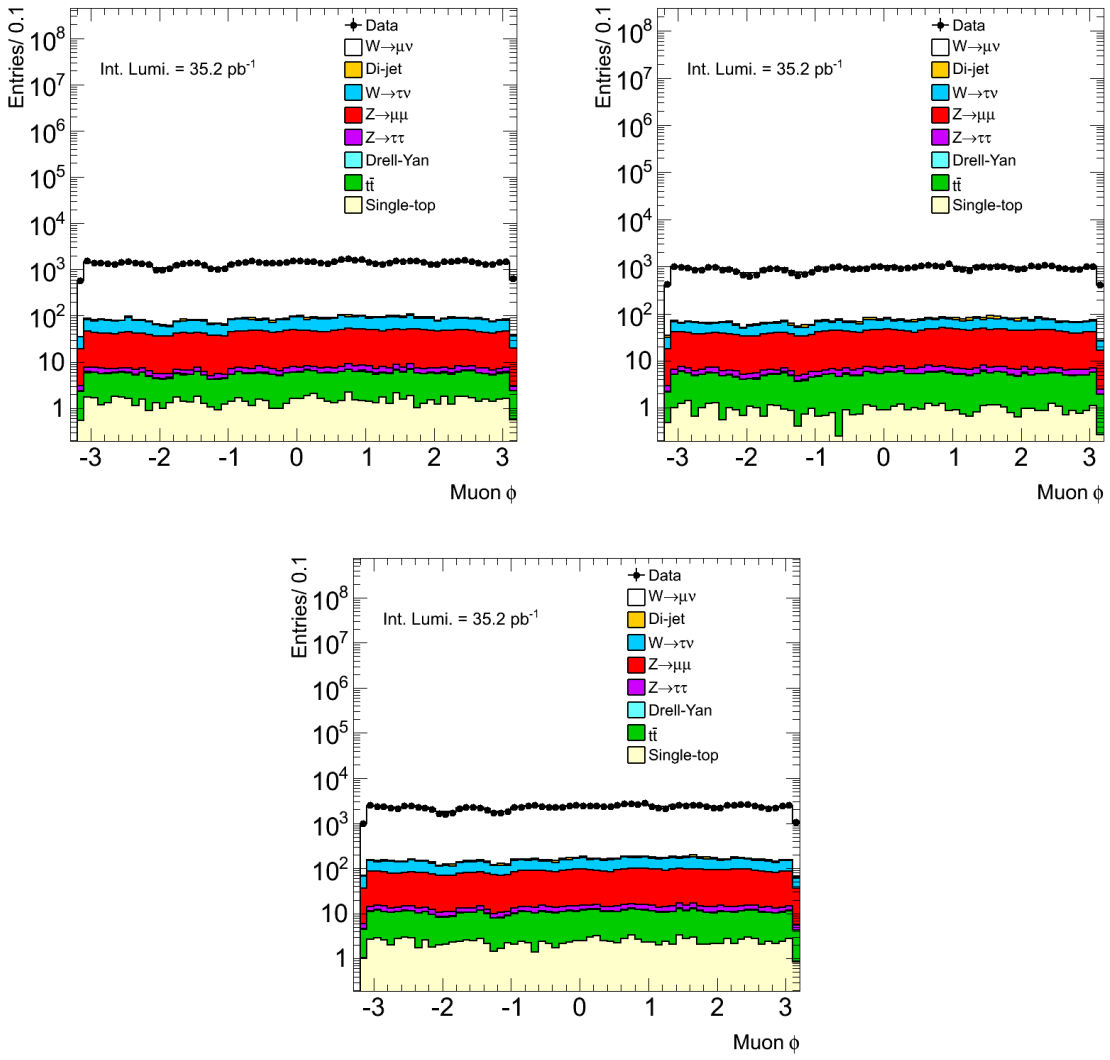

Figure 6.7: Distribution after final selection of azimuthal angle for W^+ candidates (top left), W^- (top right) and all W candidates (bottom). Black dots are for data, the color blocks are for various MC processes.

It is important to note that the acceptance obtained from the cut flow above has been corrected by several scale factors which account for the differences in reconstruction efficiencies between data and Monte Carlo. Measurement of these scale factors are performed using data-driven methods and has been described in Section 5.6.2 and Section 5.2. The scale factor applied to the final acceptance is the combination of data/MC scale factors from muon identification (98.2% from muon MS and 99.9%

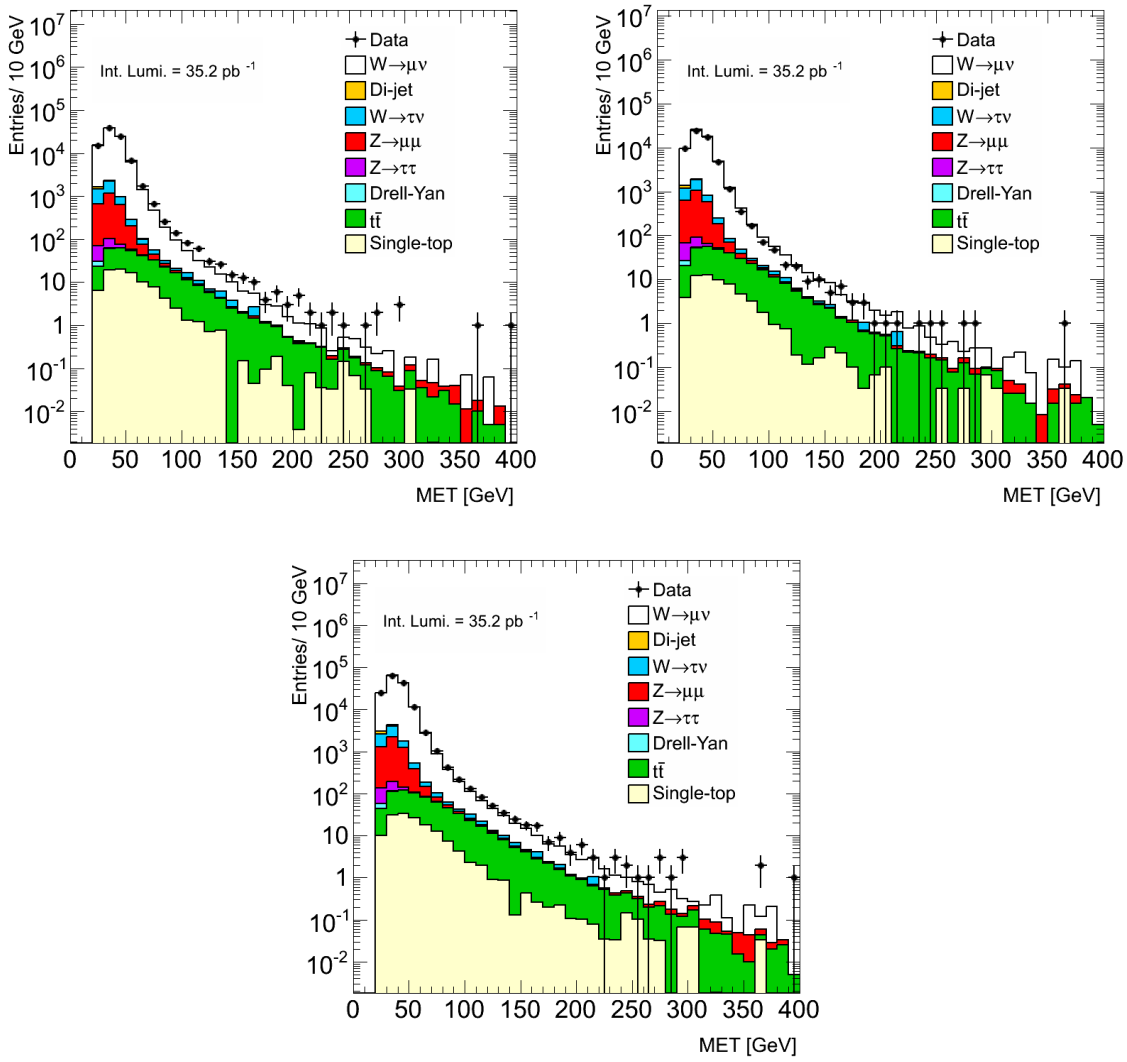

Figure 6.8: Missing transverse energy after final selection for W^+ candidates (top left), W^- candidates (top right) and all W candidates (bottom). Black dots are for data, the color blocks are for various MC processes.

from muon ID), muon isolation of 99.8% and an average of 98.0% from muon triggers.

The overall systematic uncertainty of the detection acceptance is found to be 5.4%, which includes 1.0% from trigger, 1.02% from muon identification and reconstruction, 0.5% from muon isolation requirement, 1.53% from E_T^{miss} measurement. In addition, the acceptance uncertainty includes 5% from theoretical modeling. The luminosity does not contribute to the systematics of the acceptance because the luminosity term

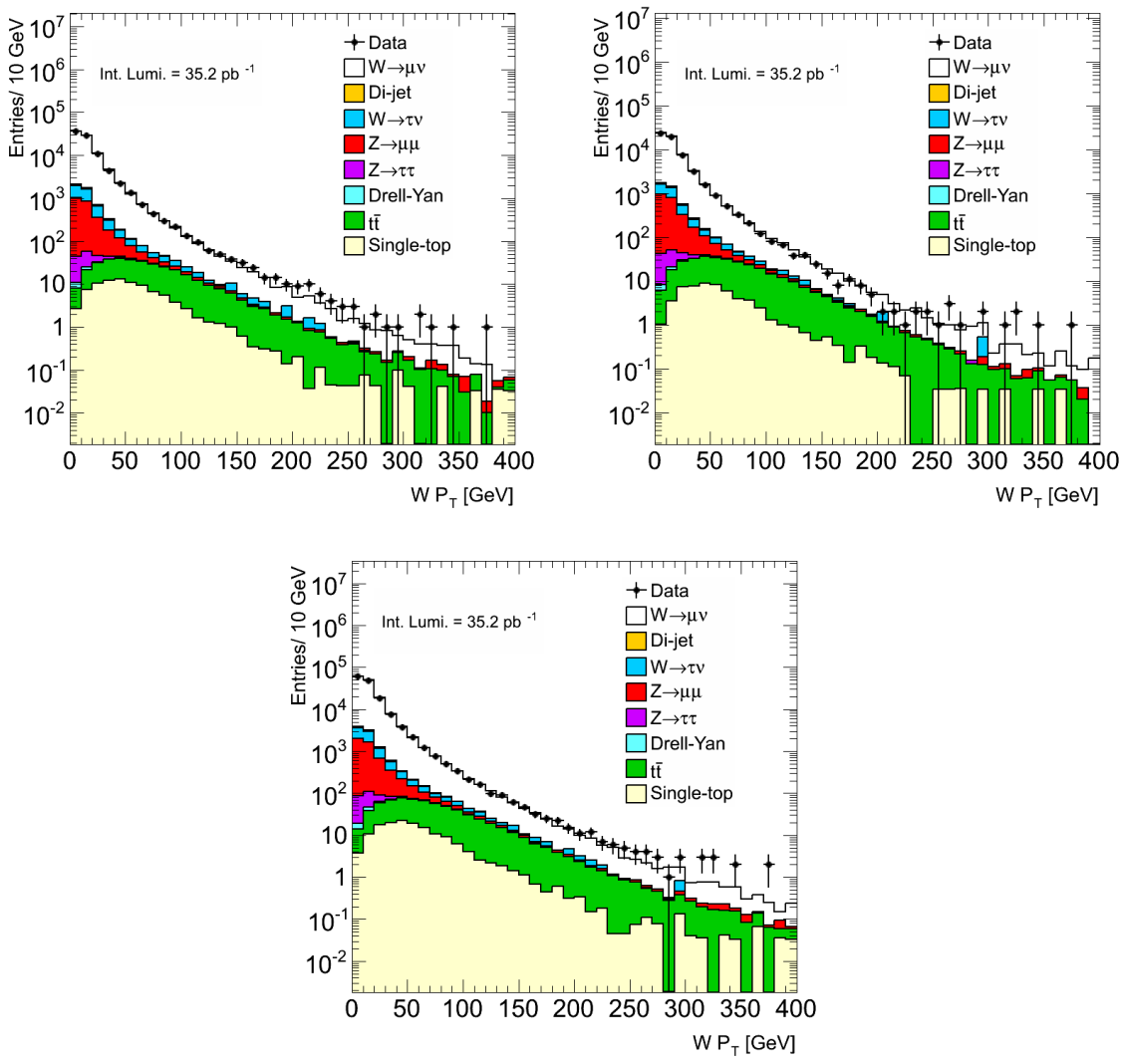

Figure 6.9: Transverse momentum of W candidates after final selection for W^+ candidates (top left), W^- candidates (top right) and all W candidates (bottom). Black dots are for data, the color blocks are for various MC processes.

cancels when taking the ratio during calculation of the acceptance. Finally, the measured detection acceptance is $38.48\% \pm 0.03\ (stat)\% \pm 2.09\ (sys)\%$.

6.4 Backgrounds and Uncertainties

The expected contribution to $W \to \mu\nu$ selection from all background processes except QCD di-jet process are determined from Monte-Carlo simulations using the

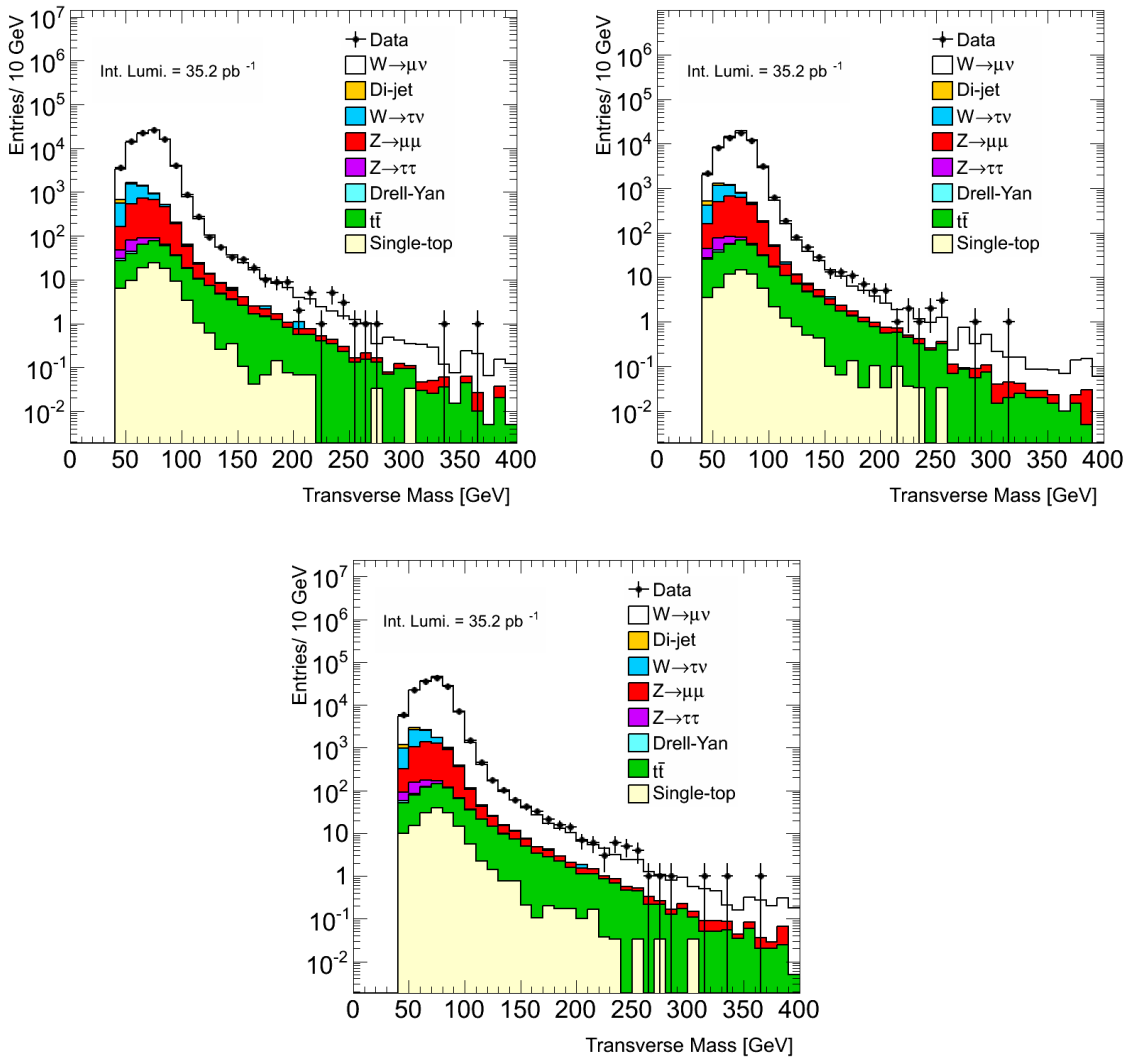

Figure 6.10: Transverse mass of W candidates after final selection for W^+ candidates (top left), W^- candidates (top right) and all W candidates (bottom). Black dots are for data, the color blocks are for various MC processes.

same event selection as used for data. The details are described in Section 6.4.1. The QCD background is primarily composed of heavy-quark decays, with smaller contributions from pion and kaon decays and hadrons faking muons. Given the large uncertainty in the di-jet cross section and the difficulty to properly simulate fake prompt muons, the QCD background has been derived from data using the *Matrix Method* as described in Section 6.4.2. Background expectations from all processes will

Cut	$W \to \mu\nu$ (Rel. Eff.)	$W \to \tau\nu \to \mu\nu$ (Rel. Eff.)	Combined
Total MC events	366293.0	63196.6	429489.6
D3PD PF, PV	282218.9 (77.0%)	22315.9 (35.3%)	304534.8
Muon Cuts	194187.4 (68.8%)	9233.7 (41.4%)	203421.1
Missing E_T	160231.8 (82.5%)	5227.4 (56.6%)	165459.2
Transverse Mass	158707.2 (99.0%)	4645.8 (88.9%)	163353.0
Trigger	136925.8 (86.3%)	3978.3 (85.6%)	140904.1
$\varepsilon \cdot \mathscr{A}$	$(37.38 \pm 0.03)\%$	$(6.30 \pm 0.04)\%$	
Combined $\varepsilon \cdot \mathscr{A}$	$(38.48 \pm 0.03)\%$		

Table 6.5: Event selection cut flow for MC signal process including $W \to \mu\nu$ and $W \to \tau\nu \to \mu\nu$. The last column is the sum of numbers of events from two processes. The detection acceptance is shown in the second to last row. The last row is the combined acceptance defined as $\varepsilon \cdot \mathscr{A} = (\varepsilon \cdot \mathscr{A})_\mu + (\varepsilon \cdot \mathscr{A})_\tau Br(\tau \to \mu\nu)$. Errors are statistical only.

Process	$Z \to \mu\mu$	$Z \to \tau\tau$	Drell-Yan	$t\bar{t}$	Single top
Total MC events	34448.9	34690.0	51606.9	3222.0	1266.0
D3PD PF, PV	31943.7	20428.5	15183.1	3185.9	1185.4
Muon Cuts	25545.1	1799.0	1526.3	856.6	247.5
Missing E_T	5256.7	378.8	24.2	737.0	206.9
Transverse Mass	5135.5	216.7	19.8	612.7	180.0
Trigger	4640.7	189.2	18.5	530.4	151.7

Table 6.6: Cut flow for MC background samples.

be summarized in the end of this section.

6.4.1 Background Estimation with Monte-Carlo

To estimate the backgrounds using MC simulation, the same selection used for data must be applied to these MC background processes. The cut flows are obtained as shown in Table 6.6. The number of events are calculated based on the integrated luminosity of 35.2 pb^{-1}.

The systematic uncertainties related to the MC background determination are given in Table 6.7. All the terms except luminosity are combined quadratically.

Source	$\Delta\sigma/\sigma$
Luminosity	3.4%
Trigger	1%
Muon ID	1.02%
Muon Isolation	0.5%
Missing E_T	1.53%
SM cross section	5% for W and Z
	12% for top

Table 6.7: Sources of systematic uncertainties that contribute to the systematics of MC background determination.

Process	N	ΔN_{stat}	ΔN_{sys}	ΔN_{lumi}
$Z \to \mu\mu$	4640.7	5.5	252.5	157.8
$Z \to \tau\tau$	189.2	1.8	10.3	6.4
Drell-Yan	18.5	1.0	1.0	0.6
$t\bar{t}$	530.4	1.5	64.7	18.0
single top	151.6	2.4	18.5	5.2

Table 6.8: Background contributions from all MC processes except QCD di-jet for all $W \to \mu\nu$.

The luminosity uncertainty is listed separately. Table 6.8-6.10 list the breakdown of background processes. Table 6.8 lists the expected backgrounds to the total $W \to \mu\nu$ process, and Table 6.9 and 6.10 are for $W^+ \to \mu^+\nu$ and $W^- \to \mu^-\nu$, respectively.

Process	N	ΔN_{stat}	ΔN_{sys}	ΔN_{lumi}
$Z \to \mu\mu$	2418.6	4.0	131.6	82.2
$Z \to \tau\tau$	96.1	1.3	5.2	3.3
Drell-Yan	10.1	0.7	0.5	0.3
$t\bar{t}$	265.3	1.0	32.3	9.0
single top	92.7	1.9	11.3	3.2

Table 6.9: Background contribution from all MC processes except QCD di-jet for $W^+ \to \mu^+\nu$.

Process	N	ΔN_{stat}	ΔN_{sys}	ΔN_{lumi}
$Z \to \mu\mu$	2222.1	3.8	120.9	75.6
$Z \to \tau\tau$	93.2	1.3	5.1	3.2
Drell-Yan	8.4	0.6	0.5	0.3
$t\bar{t}$	265.1	1.0	32.3	9.0
single top	58.9	1.5	7.2	2.0

Table 6.10: Background contribution from all MC processes except QCD di-jet for $W^- \to \mu^-\nu$.

6.4.2 Data-Driven QCD Background Estimation

In the matrix method, the QCD background is estimated from a comparison of the number of events seen in data (N_{iso}) after the full W selection, to the number of events observed (N_{loose}) if the muon isolation requirement is not applied. The number of events in these two samples can be expressed as:

$$N_{loose} = N_{nonQCD} + N_{QCD} \tag{6.2}$$

$$N_{iso} = \epsilon^{iso}_{nonQCD} N_{nonQCD} + \epsilon^{iso}_{QCD} N_{QCD} \tag{6.3}$$

Here N_{nonQCD} includes the W signal and the background from the other, non-QCD, physics processes and ϵ^{iso}_{nonQCD} and ϵ^{iso}_{QCD} denote the corresponding efficiencies of the muon isolation requirements for the two event classes. If these efficiencies are known, Equation 6.2 and 6.3 can be solved for N_{QCD}. The muon isolation efficiency for non-QCD events was measured in the data $Z \to \mu\mu$ samples using the tag-and-probe method as described in Section 5.2. The efficiency for QCD events was estimated from a QCD rich sample. This sample is selected from the low missing transverse energy events, $E_T^{miss} < 10\ GeV$, in data by requiring one and only one muon with $P_T > 10\ GeV$, transverse momentum measured in the standalone muon spectrometer with calorimeter energy loss correction $p_T(MS) > 10\ GeV$ and the difference in transverse momentum measured by muon spectrometer and by inner detector $|p_T(MS) - p_T(ID)| < 15\ GeV$. Figure 6.11 shows the isolation efficiency versus

muon P_T for QCD events. The distribution of the QCD rich sample from data is in solid black markers. Standard Model electro-weak processes ($W \to l\nu$, $Z \to \mu\mu$, etc) subtracted using Monte-Carlo simulation have blue diamond markers and QCD di-jet MC events have red square markers. The divergence of the black curve from the red and blue curves at high muon P_T suggests electro-weak contamination in the QCD rich sample. However, the agreement in the low P_T range is good. ϵ^{iso}_{QCD} is determined to be 0.18 ± 0.02 from this plot.

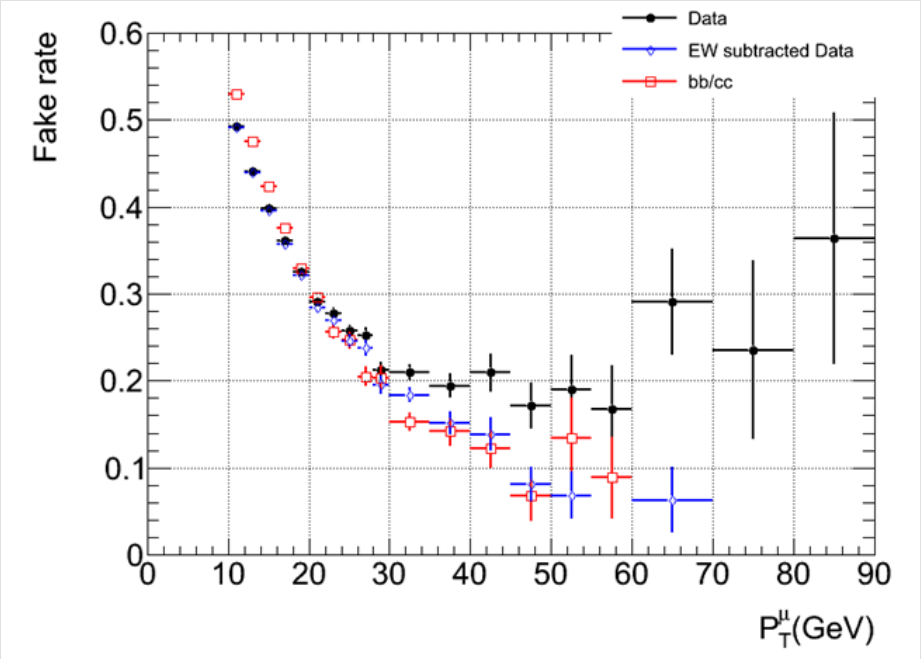

Figure 6.11: Isolation efficiency vs. muon P_T for QCD events in data (solid black), Electro-Weak processes subtracted data (blue diamond), MC di-jet events (red square).

The QCD background in the W signal selection is estimated to be $2931.18 \pm 2.21\ (stat) \pm 1468.93\ (syst)$. The systematic uncertainty is dominated by the uncertainty on the isolation efficiency for QCD events. There is no term for luminosity uncertainty in the estimated QCD background because the derivation in this data-driven method does not involve luminosity. This result is cross-checked with the MC estimation using the QCD scale factor. The results of these two methods agree with

each other.

The expected background for the W selection from all background processes are summarized in Table 6.11 (all W's), Table 6.12 (W^+) and Table 6.13 (W^-). The bottom row in the three tables are the sum of all backgrounds: the statistical uncertainties are combined quadratically, the systematical uncertainties from all processes except QCD are added linearly and then combined quadratically to that from the QCD process, and the luminosity uncertainty is the sum of all contributing processes.

Process	N	ΔN_{stat}	ΔN_{sys}	ΔN_{lumi}
$Z \to \mu\mu$	4640.7	5.5	252.5	157.8
$Z \to \tau\tau$	189.2	1.8	10.3	6.4
Drell-Yan	18.5	1.0	1.0	0.6
$t\bar{t}$	530.4	1.5	64.7	18.0
single top	151.6	2.4	18.5	5.2
QCD di-jet	2931.2	2.2	1468.9	0.0
Total	8461.6	6.9	1509.3	188.0

Table 6.11: Background contribution from different MC processes for all $W \to \mu\nu$.

Process	N	ΔN_{stat}	ΔN_{sys}	ΔN_{lumi}
$Z \to \mu\mu$	2418.6	4.0	131.6	82.2
$Z \to \tau\tau$	96.1	1.3	5.2	3.3
Drell-Yan	10.1	0.7	0.5	0.3
$t\bar{t}$	265.3	1.0	32.3	9.0
single top	92.7	1.9	11.3	3.2
QCD di-jet	1498.7	1.4	751.0	0.0
Total	4381.4	4.9	772.5	98.0

Table 6.12: Background contribution from different MC processes for $W^+ \to \mu^+\nu$.

6.5 Cross Sections

Table 6.14 is a summary of results from Section 6.2 to 6.4. The table includes observed events, expected MC signal events with the detection efficiency-acceptance

Process	N	ΔN_{stat}	ΔN_{sys}	ΔN_{lumi}
$Z \to \mu\mu$	2222.1	3.8	120.9	75.6
$Z \to \tau\tau$	93.2	1.3	5.1	3.2
Drell-Yan	8.4	0.6	0.5	0.3
$t\bar{t}$	265.1	1.0	32.3	9.0
single top	58.9	1.5	7.2	2.0
QCD di-jet	1432.5	1.9	717.9	0.0
Total	4080.2	4.8	736.8	90.0

Table 6.13: Background contribution from different MC processes for $W^- \to \mu^-\nu$.

factor and estimated background events for $W^{\pm}$ and all W's.

Process	W	W^+	W^-
Data	145226	87642	57584
MC $W \to \mu\nu$	140904.1±87.0±7665.2	82990.4±51.2±4514.7	57913.7±37.8±3150.5
MC Bkg	8461.6±6.9±1509.3	4381.4±4.9±772.5	4080.2±4.8±736.8
MC total	149365.7±87.3±7812.4	87371.8±51.4±4580.3	61993.9±38.1±3235.5
Significance	1531.8	1253.8	906.7

Table 6.14: Summary of observed data events and estimated signal and background events from MC for $W \to \mu\nu$ for total integrated luminosity of $35.2pb^{-1}$. The first error is statistical and the second one is systematic. In addition, there is 3.4% for luminosity uncertainty.

Using the terms summarized in this table and based on Equation 6.1, the total $W \to \mu\nu$ cross section is found to be:

$$\sigma_W \times Br(W \to \mu\nu) = 10.15 \pm 0.025\ (stat) \pm 0.56\ (sys) \pm 0.35\ (lumi)\ nb; \quad (6.4)$$

the $W^+ \to \mu^+\nu$ cross section is:

$$\sigma_W^+ \times Br(W^+ \to \mu^+\nu) = 6.18 \pm 0.020\ (stat) \pm 0.34\ (sys) \pm 0.21\ (lumi)\ nb; \quad (6.5)$$

the $W^- \to \mu^-\nu$ cross section is:

$$\sigma_W^- \times Br(W^- \to \mu^-\nu) = 3.97 \pm 0.016\ (stat) \pm 0.22\ (sys) \pm 0.13\ (lumi)\ nb. \quad (6.6)$$

The systematic uncertainty of the cross section is calculated based on the equation:

$$\frac{\Delta\sigma_{sys}}{\sigma_W} = \sqrt{(\frac{\Delta(\varepsilon \cdot \mathscr{A})}{\varepsilon \cdot \mathscr{A}})^2 + (\frac{\Delta N_{bkg}}{N_{obs} - N_{obs}})^2}. \quad (6.7)$$

The systematic uncertainty of the cross section is dominated by the systematics of the detection efficiency-acceptance.

The official $W \to \mu\nu$ cross sections measured by the ATLAS Standard Model group based on the 2010 data are listed in Table 6.15. The cross sections reported in this thesis are consistent with the ATLAS results.

	$\sigma_W^{tot} \times Br(W \to \mu\nu)$ [nb]			
	sta	sys	lum	acc
W^+	$6.062 \pm 0.023 \pm 0.101 \pm 0.206 \pm 0.099$			
W^-	$4.145 \pm 0.020 \pm 0.072 \pm 0.141 \pm 0.086$			
$W^\pm$	$10.210 \pm 0.030 \pm 0.166 \pm 0.347 \pm 0.153$			

Table 6.15: ATLAS published results of total cross section times branching ratio for W^+, W^- and $W^\pm$ in the muon decay channel with 2010 data [14]

The theoretical predictions of 10.46 ± 0.52 nb for total cross section, 6.16 ± 0.31 nb for W^+, and 4.30 ± 0.21 nb for W^- (Section 2.2) are in good agreement with the measured cross sections.

6.6 W^+/W^- Charge Ratio

The measurement of W^+/W^- charge ratio $R = (\sigma^+)/(\sigma^-)$ is attractive, as various systematic uncertainties cancel in this process. Theoretical predictions for cross section ratio also tend to be more precise than for the cross section alone. From the event

selection in Section 6.2, the number of W^+ and W^- candidates in each run period are extracted as shown in Table 6.16. The second to last row is the sum of number of events for all run periods, while the last row is the expected background contribution for W^+ and W^-. Based on these results, the W^+/W^- charge ratio is calculated using equation $R = (N^+_{obs} - N^+_{bkg})/(N^-_{obs} - N^-_{bkg})$. The systematic uncertainty of the W^+/W^- charge ratio is from only the background systematics and systematic uncertainty of pdf shape in the theoretical modeling, where the latter term is dominant. The luminosity uncertainty, the muon reconstruction uncertainties and missing transverse energy uncertainty do not contribute to the charge ratio. The W^+/W^- charge ratio is measured to be $1.56 \pm 0.01\ (stat) \pm 0.09\ (sys)$. This measurement is consistent with the theoretical prediction of $1.433^{+0.032}_{-0.020}$. The difference between the measured and theoretical charge ratio is due to the measurement constrained to the experimental fiducial phase space, whereas, the theoretical result is for the whole phase space.

Run Period	W^+	W^-
A - E3	1739	1153
E4 - G1	2942	1856
G2 - I1 (167576)	39374	25602
I1 (167607) -I2	43587	28973
Total Observed	87642	57584
Total Background	4381.4±4.9±772.5	4080.2±4.8±736.8

Table 6.16: Number of W^+ and W^- candidates in different Run Periods and the sum of all periods. The last row is the expected background for W^+ and W^-.

CHAPTER VII

Search for New Gauge Boson W'

This chapter is dedicated to a search for a new charged weak gauge boson W' with spin 1. Many new physics models with a new gauge symmetry extension of the Standard Model predict such gauge bosons. The search of the new gauge bosons have been extensively carried out in the Tevatron experiment D0 [19] and CDF [17]. These experiments have recently set the W' mass limit at around 1 TeV.

This chapter describes a search for W' in the muon decay channel using the first year LHC data collected by the ATLAS experiment. The experimental signature is a high-p_T isolated muon plus large missing transverse momentum due to a neutrino from W' decay escaping detection. Assuming the W' has the same gauge coupling as the Standard Model, the expectations of the W' production cross sections are calculated and given in Section 7.1. The event selection will be described in Section 7.2. An interesting candidate with transverse mass at 1.01 TeV is observed. The event display and discussion of this candidate are given in Section 7.3. Finally, the 95% confidence level of the mass limit is set based on the observed events, the W' selection efficiencies, and the estimated background contribution in Section 7.4.

7.1 Monte Carlo Samples for W'

The cross sections ($\sigma \times Br$) of W' at mass=500, 750, 1000, 1250, 1500, and 1750 GeV are listed in Table 7.1. These cross sections are calculated at next-to-next-to-leading(NNLO) order QCD using FEWZ with MSTW2008 PDFs. The $W' \to \ell\nu$, ($\ell = e, \mu, \tau$) signal events are modeled by the PYTHIA 6.421 [46] Monte Carlo program using MRST LO parton distribution functions. The numbers of generated events at each mass point are also given in Table 7.1. These events are fully simulated with the ATLAS detector response including trigger and reconstructed with final state particles, i.e. leptons, jets, and missing transverse energy. W' detection efficiencies at different mass point are determined using these fully simulated events.

Process	Mass [GeV]	σB [pb]	N_{MC}	Generator
$W' \to l\nu$	500	17.25	60000	Pythia
	750	3.2	60000	Pythia
	1000	0.8366	60000	Pythia
	1250	0.2606	40000	Pythia
	1500	0.0887	30000	Pythia
	1750	0.03246	30000	Pythia

Table 7.1: The cross section times branching ratio, total number of Monte Carlo events and generator name of $W' \to l\nu$ at different masses. l =electron, muon or tau.

7.2 W' Selection

The selection of $W' \to \mu\nu$ events follows the same flow as the $W \to \mu\nu$ in Section 6.2, with the exception of three different cuts in the muon selection criteria. First, the cut, $|p_T(MS) - p_T(ID)| < 15\ GeV$, is eliminated, because it has been found to lower the detection efficiency of high p_T muons from W' decay. Secondly, the muon spectrometer p_T cut is raised to 25 GeV from 10 GeV to accommodate the increased muon p_T from W' decay.

Thirdly, in order to identify W' candidates, the kinematic variable–transverse mass

Cut	W' (500 GeV)	W' (1000 GeV)	W' (1250 GeV)	W' (1500 GeV)
Total MC	1821.0	88.34	27.52	9.37
D3PD PF, PV	1722.46±7.08	83.56±0.34	26.02±0.13	8.86±0.05
Muon Cuts	558.02±4.03	28.05±0.20	8.76±0.08	2.93±0.03
Missing E_T	554.47±4.02	27.96±0.20	8.74±0.08	2.92±0.03
m_T	419.29±3.49	19.50±0.17	5.92±0.06	1.90±0.02
Trigger	354.68±3.21	16.30±0.15	4.93±0.06	1.58±0.02
Acceptance [%]	19.48 ± 0.18	18.45 ± 0.17	17.91 ± 0.22	16.86 ± 0.21

Table 7.2: Cut flow for MC W' signal process. Total acceptance is listed in the last row. The mass cut for W' mass at 500/1000/1250/1500 GeV is 250/500/625/750 GeV, respectively. Numbers of events are normalized to 35.2 pb^{-1}. Errors are statistical only.

m_T, as defined as in Equation 7.1, has to be larger than half of the mass value of the corresponding W' model. For example, m_T is required to be larger than 500 GeV for W' model with mass at 1 TeV.

$$m_T = \sqrt{2p_T^{\mu} E_T^{miss}(1 - \cos\Delta\phi_{\mu\nu})} \tag{7.1}$$

The event selection cut flow tables with W' model assumption at mass=500, 1000, 1250, and 1500 GeV are listed in Table 7.2. The signal acceptance is calculated and also shown in the last row of this table. The errors shown in this table are statistical only.

The overall systematic uncertainty of W' detection acceptance is found to be 2.7%, which includes 1.0% from trigger, 1.02% from muon identification and reconstruction, 0.5% from muon isolation requirement, 1.53% from E_T^{miss} measurement. In addition, the acceptance uncertainty includes 1.75% from theoretical modeling.

The background is estimated in a similar way as to the W cross section measurement. Different background sources and contributions to the W' search with different mass values are given in Table 7.3. Contributions to the systematic uncertainties of

Process	500 GeV	1000 GeV	1250 GeV	1500 GeV
$W \to \mu\nu$	21.1±1.04±1.15	1.34±0.26±0.07	0.56±0.17±0.03	0.21±0.10±0.01
$W \to \tau\nu$	0.00±0.00±0.00	0.00±0.00±0.00	0.00±0.00±0.00	0.00±0.00±0.00
$Z \to \mu\mu$	2.09±0.12±0.11	0.14±0.03±0.01	0.05±0.02±0.00	0.01±0.01±0.00
$Z \to \tau\tau$	0.05±0.03±0.00	0.00±0.00±0.00	0.00±0.00±0.00	0.00±0.00±0.00
Drell-Yan	0.10±0.07±0.01	0.05±0.05±0.00	0.05±0.05±0.00	0.05±0.05±0.00
$t\bar{t}$	3.51±0.12±0.43	0.10±0.02±0.01	0.04±0.01±0.00	0.00±0.00±0.00
single top	0.37±0.12±0.00	0.04±0.04±0.00	0.00±0.00±0.00	0.00±0.00±0.00
QCD di-jet	0.00±0.00±0.00	0.00±0.00±0.00	0.00±0.00±0.00	0.00±0.00±0.00

Table 7.3: Number of events in MC Standard Model background processes that passed W' selection. The mass cut for W' mass at 500/1000/1250/1500 GeV is 250/500/625/750 GeV, respectively. Numbers of events are normalized to 35.2 pb^{-1}. The first error is statistical uncertainty and the second one is systematic uncertainty.

Mass [GeV]	N_{obs}	$N_{W'}$	N_{bkg}
500	30	354.68±3.21±9.58	27.2±2.11±1.23
1000	2	16.30±0.15±0.44	1.66±1.33±0.07
1250	1	4.93±0.06±0.13	0.71±0.57±0.03
1500	1	1.58±0.02±0.04	0.27±0.21±0.01

Table 7.4: Summary of results including expected number of W' signal process, SM background and number of observed events. Numbers of events for MC processes are normalized to 35.2 pb^{-1}. The first error is statistical uncertainty and the second one is systematic uncertainty.

the backgrounds are 1.0% from trigger, 1.02% from muon identification and reconstruction, 0.5% from muon isolation requirement, 1.53% from E_T^{miss} measurement, 5%/12% from theoretical modeling for W and Z/top processes.

Finally, the numbers of observed events passing the W' selection cuts, the expected W' signal events, and the estimated number of SM background are summarized in Table 7.4. The observed events are statistically consistent with the SM background estimation. No evidence of W' signal is observed. However, one observed candidate event with mass around 1 TeV has attracted attention. This event is investigated in the next section.

7.3 An Interesting W' Candidate Event

As indicated in Table 7.4, there is one W' candidate event observed from the data with transverse mass at 1.06 TeV.This event is indexed by event number = 70584935, Luminosity Block Number (LBN) = 276, and Bunch Crossing Identity (BCID) = 2002 from run 167607 in run period I1. The kinematic variables of this event are listed in Table 7.5.

Physics Object	p_T [GeV]	η	ϕ
Muon	531.36	-1.52	-0.38
E_T^{miss} (ν)	536.52	-	2.79
$Muon + E_T^{miss}$	17.03	-4.91	-2.24

Table 7.5: Kinematic variables of an event observed with transverse mass at 1.06 TeV. This event is indexed by event number = 70584935, Luminosity Block Number (LBN) = 276, and Bunch Crossing Identity (BCID) = 2002 from run 167607 in run period I1.

This event was examined in detail using the ATLAS software Atlantis event display shown in Figure 7.1. This event display uses a reprocessed data-set and indicates a muon p_T much smaller than the muon p_T determined using the initial processed data-set as shown in Table 7.5. Further checks was made using at the muon momentum reconstructions by the inner tracker and muon spectrometer stand-alone packages. The two reconstructed p_T's were 34.59 GeV and 26.46 GeV, respectively, but the combined reconstructed muon p_T was a much higher value (531 GeV). It is clear that the high combined muon p_T was an artifact from the Staco fitting algorithm. The mis-measured muon leads to a mis-measured transverse missing energy, which resulted in this candidate with a 1.06 TeV transverse mass. The bug in the staco algorithm is corrected in the new data-set (with data-set tag f341 and later) after the data reprocessing in November 2010.

Another cross-check of this candidate was performed with different muon reconstruction package, MuID. From the MuID reconstruction program, this muon mo-

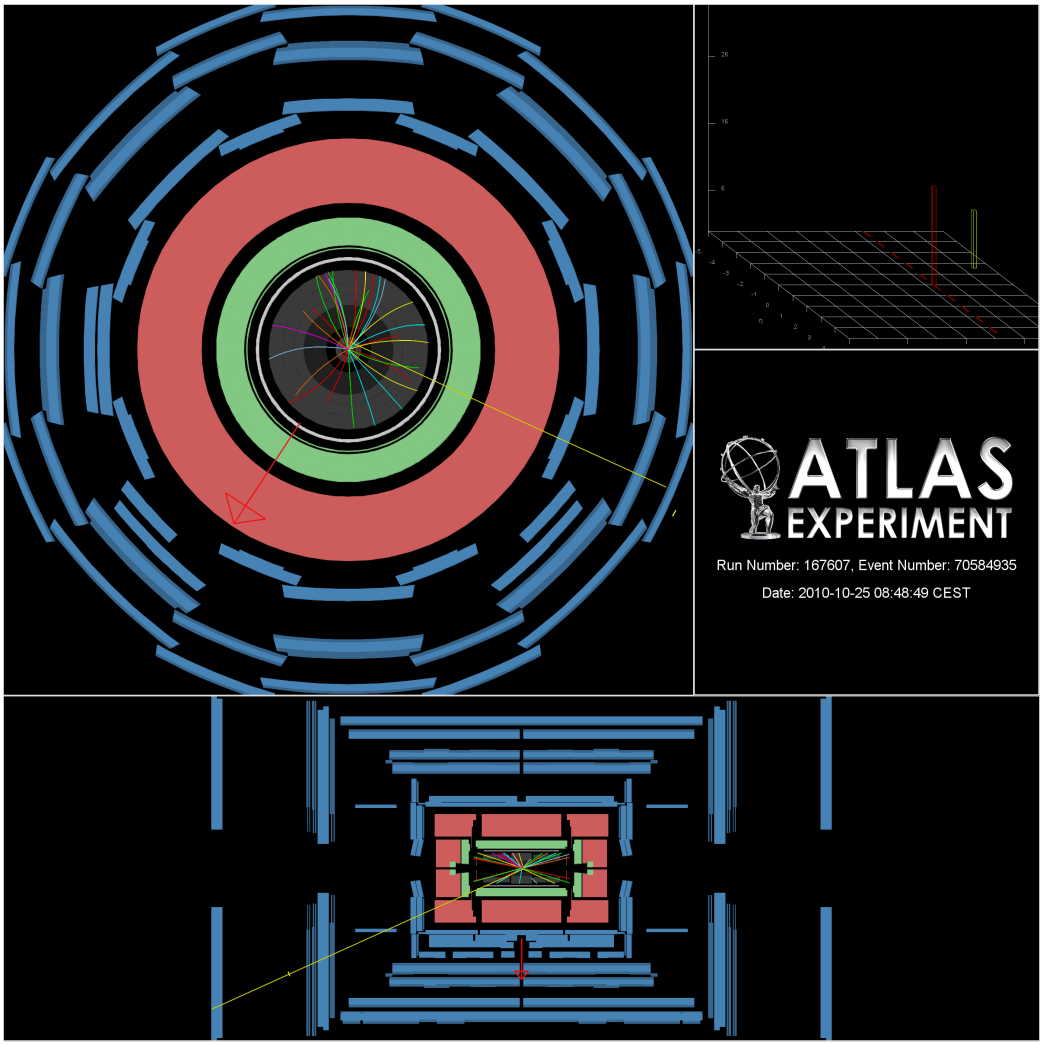

Figure 7.1: Event display of an event observed with transverse mass at 1.06 TeV. This event is indexed by event number = 70584935, Luminosity Block Number (LBN) = 276, and Bunch Crossing Identity (BCID) = 2002 from run 167607 in run period I1.

mentum is determined to be consistent with the inner tracker and muon spectrometer standalone measurement at around 35 GeV. This confirms that this event is not a W' candidate. Based on these findings, this event is removed from the observed events in the W' search program.

7.4 95% Confidence Level Limit on W' Mass

Limits for a 95% Confidence Level (CL) exclusion on the cross section (σBr) for W' are set using a single-bin likelihood analysis. The likelihood to observe N_{obs} events based on Poisson statistics is:

$$L = \frac{N_{exp}^{N_{obs}} e^{-N_{exp}}}{N_{obs}!}, \tag{7.2}$$

The likelihood ratio test-statistic is:

$$Q = \frac{L(s+b)}{L(b)}. \tag{7.3}$$

In background only hypothesis $N_{exp} = N_{bkg}$. In signal plus background hypothesis, $L(s+b)$, $N_{exp} = N_{bkg} + N_{W'}$, where $N_{W'}$ is determined from the predicted cross section times branching ratio, W' detection efficiency determined in Section 7.2, and the total integrated luminosity, i.e. $N_{W'} = \sigma Br \cdot \varepsilon \cdot \mathscr{A} \cdot \mathscr{L}$. The likelihood ratio test statistic is then used to find the confidence level, which is defined as:

$$CL_s = \frac{CL_{s+b}}{CL_b}, \tag{7.4}$$

as illustrated in Figure 7.2. Monte Carlo experiments are performed to determine the central value of signal process so that $1 - CL_s = 95\%$.

Uncertainties are handled by introducing Gaussian probability density functions characterizing signal and background uncertainties neglecting correlations between signal and background uncertainties. This Gaussian probability density function is multiplied to the likelihood in Equation 7.2.

Based on the observed and estimated backgrounds events, and W' detection efficiency, the 95% confidence level limits on W' cross sections are calculated and shown in Table 7.6 for four different masses. Both limits with and without the uncertainties

Mass [GeV]	without uncertainty		with uncertainty	
	Observed	Expected	Observed	Expected
500	0.713	0.661	0.732	0.680
1000	0.240	0.241	0.241	0.241
1250	0.195	0.195	0.196	0.196
1500	0.183	0.183	0.183	0.183

Table 7.6: 95% CL limit for W' cross section in pb.

taken into account are listed in this table.

To set the W' mass limit, the 95% CL limits on cross section with uncertainty are plotted against W' mass as shown in Figure 7.3. The theoretical cross section curve calculated with sequential Standard Model couplings as a function of W' mass is also shown in Figure 7.3. Comparison of the measured cross section limit and theoretical predictions gives the 95% confidence level limit of W' mass to be higher than 1.32 TeV. This limit is improved from the recent ATLAS results [16] at 1.29 TeV in the muon channel, which analyzed only muons from the barrel region of the detector. This limit also exceeds the limit set by Tevatron experiments, 1.12 TeV, based on much higher integrated luminosity ($\sim 5.3\ fb^{-1}$) from $p\bar{p}$ collisions at $\sqrt{s} = 1.96\ TeV$.

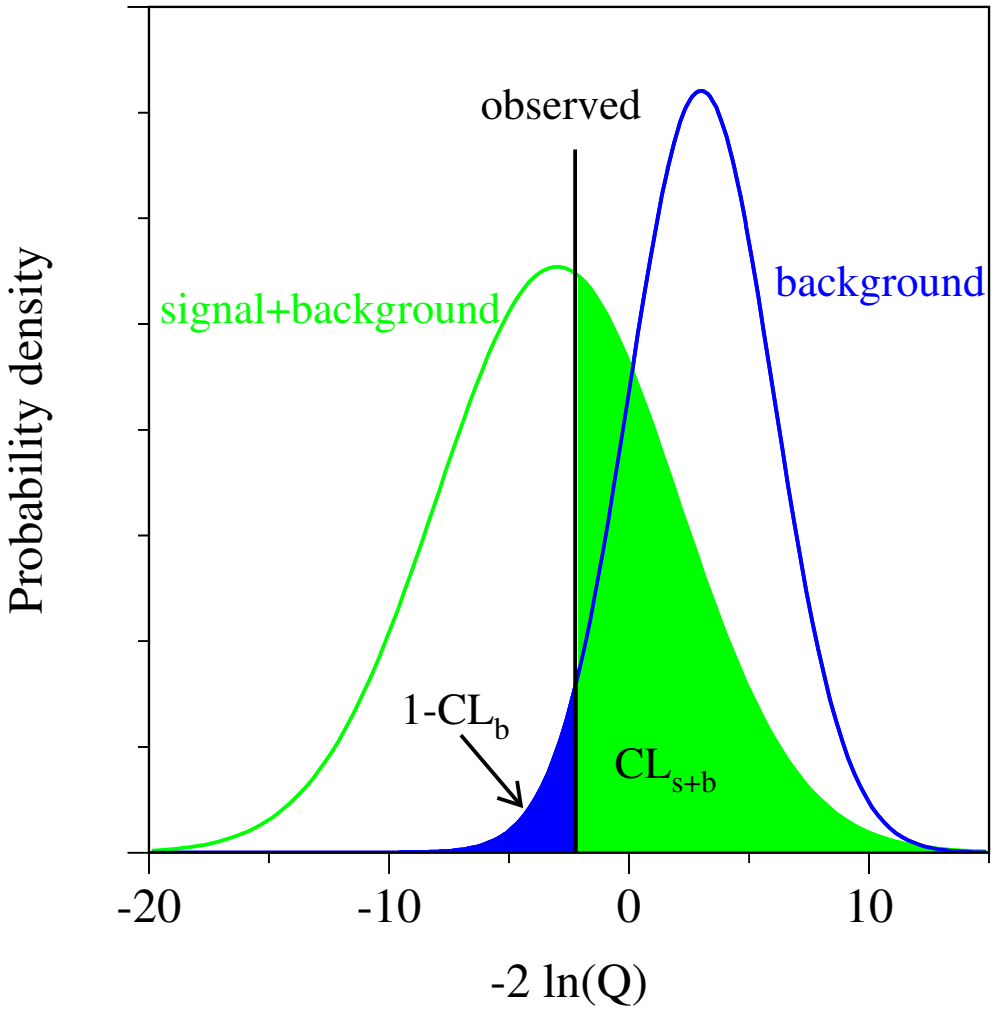

Figure 7.2: Illustration of likelihood ratio test statistics based on Poisson distribution. Blue curve is background only hypothesis. Green curve is background plus signal hypothesis. The value of observed events is in black.

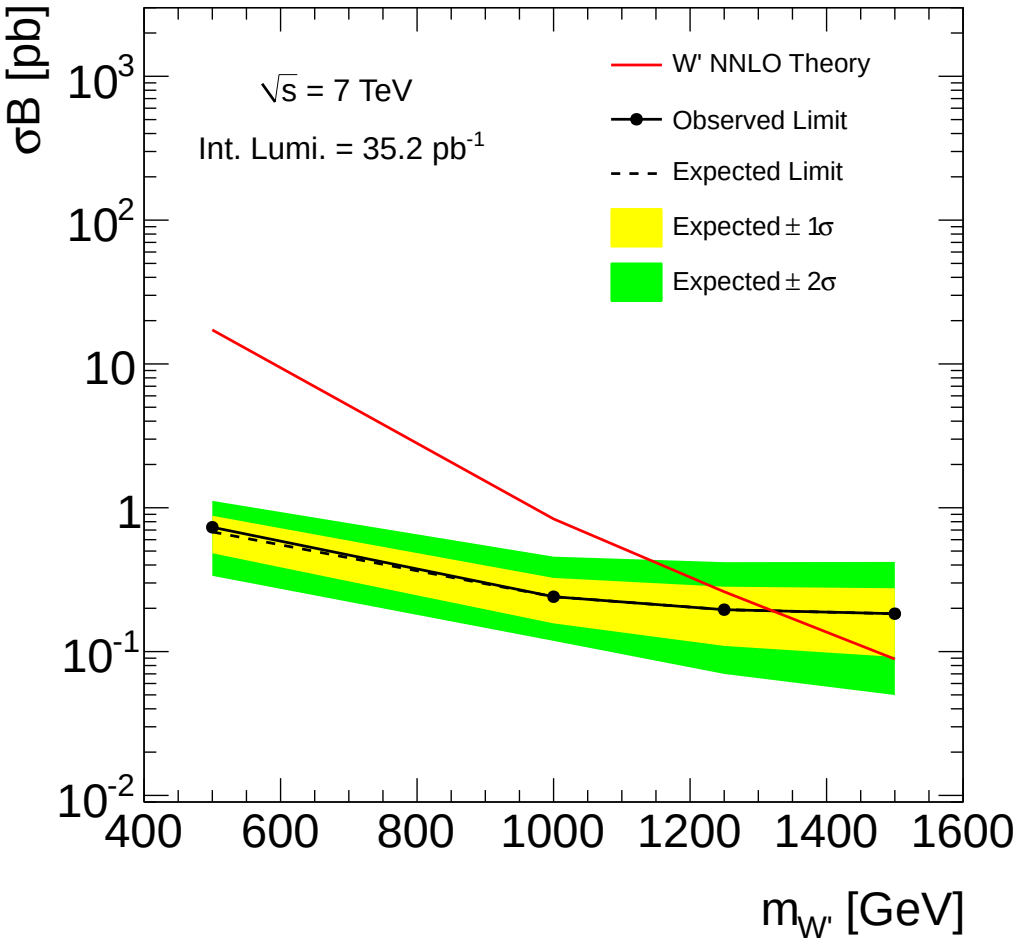

Figure 7.3: Limit at 95% CL for $W' \to \mu\nu$. The solid black line is the observed limit. The expected limit is indicated with black dashed lines surrounded by 1σ (yellow) and 2σ (green) shaded bands. The W' cross section given by NNLO theory is shown in red line.

CHAPTER VIII

Results and Conclusions

The first year of the Large Hadron Collider and the ATLAS experiment were remarkably successful. Using data collected by the ATLAS detector from March 30 to October 31, 2010 with an integrated luminosity of 35.2 pb^{-1}, the measurement of the weak gauge boson W production and search for new gauge boson W' in the $\mu\nu$ decay channel were performed.

Table 8.1 summarizes the number of W candidate events selected with this data and estimated background for the W cross section measurement. The measured cross sections are shown in Table 8.2 along with the corresponding Next-to-Leading order Standard Model prediction. Based on this comparison, the cross sections measured in this thesis are consistent with the theoretical predictions.

Process	Observed Events	Estimated Background
All W	145226	$8461.6 \pm 6.9\ (stat) \pm 1509.3\ (sys) \pm 188.0\ (lumi)$
W^+	87642	$4381.4 \pm 4.9\ (stat) \pm 772.5\ (sys) \pm 149.0\ (lumi)$
W^-	57584	$4080.2 \pm 4.8\ (stat) \pm 736.8\ (sys) \pm 138.7\ (lumi)$

Table 8.1: Summary of observed data events and estimated background events for $W \to \mu\nu$ analysis with total integrated luminosity of $35.2 pb^{-1}$.

The W^+/W^- charge ratio is measured to be $1.56 \pm 0.01\ (stat) \pm 0.09\ (sys)$, compared to the theoretical prediction at $1.433^{+0.032}_{-0.020}$. The measured charge ratio is consistent with the theoretical prediction.

Process	Measured Cross Section [nb]	Theory [nb]
All W	$10.15 \pm 0.025\ (stat) \pm 0.56\ (sys) \pm 0.35\ (lumi)$	10.46 ± 0.52
W^+	$6.18 \pm 0.020\ (stat) \pm 0.34\ (sys) \pm 0.21\ (lumi)$	6.16 ± 0.31
W^-	$3.97 \pm 0.016\ (stat) \pm 0.22\ (sys) \pm 0.13\ (lumi)$	4.30 ± 0.21

Table 8.2: Measured $W \to \mu\nu$ cross sections with a total integrated luminosity of $35.2 pb^{-1}$ and the Next-to-Leading order Standard Model predictions.

The dominant systematic error is from the total integrated luminosity. The combined systematic error from trigger, muon identification and missing energy measurement gives similar uncertainty. Further reduction of the systematic uncertainties will be very challenging.

The W' was searched for in the high mass region in the transverse mass spectrum calculated with muon p_T and E_T^{miss}. The observed number of events are consistent with the Standard Model prediction. No experimental evidence of the W' in $\mu\nu$ decay channel was observed. A 95% confidence level of lower mass limit for W' is set at 1.32 TeV, exceeding the limit recently set by Tevatron experiments with much higher integrated luminosity ($\sim 5.3\ fb^{-1}$) for $p\bar{p}$ collisions at $\sqrt{s} = 1.96\ TeV$.

BIBLIOGRAPHY

BIBLIOGRAPHY

[1] http://dorigo.wordpress.com/2007/11/10/
the-goldstone-theorem-for-real-dummies/.

[2] https://twiki.cern.ch/twiki/bin/view/AtlasPublic/LuminosityPublicResults.

[3] https://twiki.cern.ch/twiki/bin/view/AtlasPublic/
MuonPerformancePublicPlots.

[4] https://twiki.cern.ch/twiki/bin/viewauth/Atlas/GoodRunsListsTutorial,
https://atlasdqm.cern.ch/grl/, http://atlasdqm.web.cern.ch/atlasdqm/grlgen/.

[5] http://root.cern.ch/root/html/TMinuit.html.

[6] https://twiki.cern.ch/twiki/bin/viewauth/AtlasProtected/
JetEtmissDataAnalysisRecommendationSummer2010.

[7] Performance of the Missing Transverse Energy Reconstruction in Minimum Bias Collisions at Center-of-mass Energy of $\sqrt{s} = 7\ TeV$ with the ATLAS Detector. ATLAS internal note: ATLAS-CONF-2010-039.

[8] Properties of Jes and Inputs to Jet Reconstruction and Calibration with the ATLAS Detector Using Proton-proton Collisions at $\sqrt{s} = 7\ TeV$. ATLAS internal note: ATLAS-CONF-2010-053.

[9] Single Boson and Diboson Production Cross Section in *pp* Collisions at $\sqrt{s} = 7\ TeV$. ATLAS physics note: ATLAS-COM-PHYS-2010-695.

[10] Updated Luminosity Determination in pp Collisions at $\sqrt{s} = 7\ TeV$ Using the ATLAS Detector. ATLAS conference note: ATLAS-CONF-2011-011.

[11] G. Aad et al. *Expected Performance of the ATLAS Experiment - Detector, Trigger and Physics*. CERN/LHCC, 2008.

[12] G. Aad et al. The ATLAS Experiment at the CERN Large Hadron Collider. *JINST*, 3:S08003, 2008.

[13] G. Aad et al. Measurement of Inclusive Jet and Dijet Cross Sections in Proton-proton Collisions at 7 TeV Centre-of-mass Energy with the ATLAS Detector. *Submitted to The European Physical Journal C - Particles and Fields*, 2010.

[14] G. Aad et al. Measurement of the inclusive $W^{\pm}$ and Z/γ^{*} cross sections in the electron and muon decay channels in pp collisions at $\sqrt{s} = 7\ TeV$ with the ATLAS detector. *Submitted to High Energy Physics - Experiment, arXiv:1109.5141v3*, 2011.

[15] G. Aad et al. Performance of the ATLAS Trigger System in 2010. *Submitted to The European Physical Journal C - Particles and Fields*, 2011.

[16] G. Aad et al. Search for high-mass states with one lepton plus missing transverse momentum in protonCproton collisions ats=7TeVwith the ATLAS detector. *Physics Letters B*, 701:50–69, 2011.

[17] T. Aaltonen et al. Search for New Heavy Gauge Boson W' with Event Signature Electron+Missing Transverse Energy in $p\bar{p}$ Collisions at $\sqrt{s}$=1.96 TeV . *Phys. Rev. D*, 83, 2011.

[18] Abachi, S. and others. W and Z Boson Production in $p\bar{p}$ Collisions at $\sqrt{s} = 1.8\ TeV$. *Physical Review Letters*, 75:1456–1461, 1995.

[19] V. M. Abazov et al. Search for W' Bosons Decaying to an Electron and a Neutrino with the D0 Detector. *Phys. Rev. Lett.*, 100, 2008.

[20] Abe, F. and others. Measurement of the Production and Muonic Decay Rate of W and Z Boson in $p\bar{p}$ Collisions at $\sqrt{s} = 1.8\ TeV$. *Physical Review Letters*, 69:28–32, 1992.

[21] Abreu, P. and others. Measurement and Interpretation of the W-pair cross-section in $e^{+}e^{-}$ Interactions at $\sqrt{s} = 161\ GeV$. *Physics Letters B*, 397:158–170, 1997.

[22] Abulencia, A. and others. Measurement of Inclusive W and Z Cross Sections in $p\bar{p}$ Collisions at $\sqrt{s} = 1.96\ TeV$. *Journal of Physics G: Nuclear and Particle Physics*, 34:2457–2544, 2007.

[23] Acciarri, M. and others. Pair-production of W Bosons in $e^{+}e^{-}$ Interactions at $\sqrt{s} = 161\ GeV$. *Physics Letters B*, 398:223–238, 1997.

[24] Ahmet, K. and others. The OPAL detector at LEP. *Nuclear Instruments and Methods in Physics Research Section A: Accelerators, Spectrometers, Detectors and Associated Equipment*, 305:275–319, 1991.

[25] S. Alioli. Cross Section Benchmarks for 7 TeV LHC. Presented at the PDF4LHC Meeting at CERN, 2010.

[26] M. B. Altarelli, G. and M. Ruiz-Altaba. Searching for new heavy vector bosons in p$\bar{p}$ colliders. *Z. Phys. C*, 45:109–121, 1989.

[27] D. L. M. K. Anastasiou, Charalampos and F. Petriello. High precision QCD at hadron colliders: Electroweak gauge boson rapidity distribution at NNLO. *Phys. Rev. D.*, 69:094008, 2004.

[28] D. S. D. G. Arkani-Hamed, N. and J. March-Russell. Neutrino masses from large extra dimensions. *Phys. Rev. D*, 65:024032, 2001.

[29] Arnison, G. and others. Experimental Observation of Isolated Large Transverse Energy Electron With Associated Missing Energy at $\sqrt{s} = 540\ GeV$. *Physics Letters B*, 122:103–116, 1983.

[30] Banner, M. and others. Observation of Single Isolated Electrons of High Transverse Momentum in Events with Missing Transverse Energy at the CERN $\bar{p}$p Collider. *Physics Letters B*, 122:476–485, 1983.

[31] Barger, Vernon D. and Phillips, Roger. *COLLIDER PHYSICS*. 2 edition.

[32] P. Chiappetta. Introduction to Strong Higgs Sector. *High Energy Physics - Phenomenology*, 1994.

[33] A. Collaboration. Measurement of the $W \to l\nu$ and $Z/\gamma^* \to ll$ production cross sections in proton-proton collisions at $\sqrt{s} = 7TeV$ with the ATLAS detector. CERN-PH-EP-2010-037, Oct 2010, 38 pp.

[34] Decamp, D. and others. ALEPH: A detector for electron-positron annihilations at LEP. *Nuclear Instruments and Methods in Physics Research Section A: Accelerators, Spectrometers, Detectors and Associated Equipment*, 294:121–178, 1990.

[35] Evans, Lyndon and Bryant, Philip (editors). LHC Machine. *JINST*, 3:S08001, 2008.

[36] S. Frixione and B. Webber. http://www.hep.phy.cam.ac.uk/theory/webber/MCatNLO/.

[37] Gilman, F. J., Kleinknecht, K and Renk, B. The Cabibbo-Kobayashi-Maskawa Quark-Mixing Matrix. *The European Physical Journal C - Particles and Fields*, 15:110–114, 2000.

[38] Glashow, Sheldon L. Partial-symmetries of weak interactions. *Nuclear Physics*, 2:579–588, 1961.

[39] H. J. A. M. E. Gross, D. J. and R. Rohm. Heterotic String. *Phys. Rev. Lett.*, 54:502–505, 1985.

[40] Kane, Gordon. *MORDERN ELEMENTARY PARTICLE PHYSICS*. Updated edition.

[41] R. R. W. Langacker, P. and J. L. Rosner. New heavy gauge bosons in pp and p$\bar{p}$ collisions. *Phys. Rev. D*, 30:1470–1487, 1984.

[42] S. W. J. T. R. S. Martin, A. D. and G. Watt. Parton distributions for the LHC. *The European Physical Journal C - Particles and Fields*, 63:189–285, 2009.

[43] K. Nakamura et al. Review of Particle Physics. *Journal of Physics G*, 37:075021, 2010.

[44] J. C. Pati and A. Salam. Lepton number as the fourth "color". *Phys. Rev. D*, 10:275–289, 1974.

[45] Salam, Abdus and Ward, J. C. Weak and electromagnetic interactions. *IL NUOVO CIMENTO*, 11:568–577, 1955-1965.

[46] T. Sjostrand et al. High-energy physics event generation with PYTHIA 6.1. *Comput. Phys. Commun.*, 135:238–259, 2001.

[47] Weinberg, Steven. A Model of Leptons. *Phys. Rev. Lett.*, 19:1264–1266, 1967.